LUND UNIVERSITY

Computational Tools for Antenna Analysis and Design

Tayli, Doruk

2018

Document Version:
Publisher's PDF, also known as Version of record

Link to publication

Citation for published version (APA):
Tayli, D. (2018). *Computational Tools for Antenna Analysis and Design*. [Doctoral Thesis (compilation), Department of Electrical and Information Technology]. Electromagnetic Theory Department of Electrical and Information Technology Lund University Sweden.

Total number of authors:
1

Computational Tools for Antenna Analysis and Design

Doruk Tayli

Doctoral Dissertation

Lund University
Lund, Sweden
2018

Doctoral dissertation which, by due permission of the Faculty of Engineering, Lund University, will be publicly defended on March 2, 2018, at 10.15 a.m. in lecture hall E:1406, John Erikssons väg 4, Lund, for the degree of Doctor of Philosophy in Electrical Engineering.

Department of Electrical and Information Technology
Electromagnetic Theory Group
Lund University
P.O. Box 118, S-221 00 Lund, Sweden

Series of licentiate and doctoral theses
ISSN 1654-790X; No. 109
ISBN 978-91-7753-461-7 (print)
ISBN 978-91-7753-462-4 (digital)

Till in that twilight of the gods
When earth and sun are frozen clods,
When, all its energy degraded,
Matter in æther shall have faded,
We, that is, all the work we've done,
As waves in æther, shall for ever run
In swift-expanding spheres, through heavens
beyond the sun.

— James Clerk Maxwell, *A Paradoxical Ode*

Abstract

Many engineers and scientists prevalently use computational tools in electromagnetics, which is also the predominant case for antennas. The ever-increasing number of applications and technologies that employ antennas create a constant demand to improve and extend existing tools and develop new ones. This dissertation investigates computational tools for antenna analysis and design. Antenna current optimization is used to determine the theoretical performance bounds on antennas above a ground plane. The results add insight to the performance of patch antennas and can thereby benefit antenna designers. Moreover, the limits are used to design antennas in method of moments (MoM) and genetic algorithm (GA) solvers. The matrices used to compute characteristic modes, that is a generalized eigenvalue problem, are analyzed. Numerical issues of the calculation are circumvented, and the computational complexity is decreased with the use of spherical vector waves. A macro basis function (MBF) and adaptive cross approximation (ACA) algorithm framework is employed to simulate vast endfire arrays. Convex optimization is used to synthesize endfire patterns with improved matching performance. Furthermore, the performance of two techniques that are used in the MBF method to model interconnected arrays is investigated in the endfire mode.

Popular Science

Electromagnetic waves and, scores of electronic devices that use them are an inherent part of our daily life. Electromagnetic waves not only allow us to communicate over long distances but also to predict the weather, to perform geographical and geological surveys through satellite imaging, to visualize human anatomy, investigate subatomic structures; and detect objects beyond our field of perception. Most pleasant and unnoticed uses are embedded within our multimedia devices. Theoretical developments and experiments of the 19^{th} century by great scientists and engineers gave us this new power that is in the realm of "magic" in the eyes of earlier generations. The impact of mobile phones in our daily lives is a significant example of this change.

The ever-increasing number of wireless devices and mobile applications are expected to grow at exponential rates in the future. According to experts, the Internet of Things (IoT), which is a combination of objects connected to the internet, will be 30 billion devices by 2020. These objects will require multiple wireless communication technologies Wi-Fi, Bluetooth, 4G and the upcoming 5G. Naturally, all of these communication technologies need radiating elements, antennas, to convert electrical signals into electromagnetic waves and vice versa.

Designing antennas for portable systems is a challenge for engineers as antennas, unlike electronic circuits, cannot be scaled down in size due to the laws of physics. Usually, antennas are required to perform at their bounds with an ever increasing restriction of space and demand for maximum performance from mobile wireless systems. Pushing the limits of current paradigms bring with it the need for new analysis and design tools.

Antenna engineers rely on simulations to analyze their designs before prototyping, to reduce the costs and speed up the product development cycle. While there are excellent commercial electromagnetic tools that aid designers, there is a constant need to improve the efficiency of simulation and modeling software as simulation times increase with the complexity and size of the device under investigation. For instance, computation time can last even on powerful computing platforms from weeks to months depending on the complexity and scale of the problem. Therefore any reduction in simulation time is vital.

In this thesis, computational tools are investigated to augment the area of antenna analysis and design procedures. One of the primary techniques is the computation of physical limitations for antennas, which answers the question "how close is the performance of the antenna under design to the theoretical optimum." Another technique the characteristic mode (CM) analysis that is used to investigate the natural modes of antennas, is extended to improve both its accuracy and efficiency. Lastly, macro basis functions (MBF) and the adaptive cross approximation (ACA) algorithm is used in the design and analysis of large antenna arrays. Commonly simulations of these massive structures are done on powerful workstations. With this framework, it is possible to simulate the same structure in less time and with the same accuracy on a personal computer.

Preface

This doctoral dissertation summarizes the research which I have carried out at the Department of Electrical and Information Technology, Lund University, Sweden. The first part introduces the research objectives and scope; presents the theoretical background and antenna definitions; then focuses on the computational tools. The second part presents the research contribution published in the scientific papers listed below.

List of Included Papers

I. D. Tayli and M. Gustafsson,
"Physical Bounds for Antennas Above a Ground Plane"
IEEE Antennas Wireless Propagation Letters, Vol. 15, pp. 1281–1284, 2015
Contributions of the author: The author of this thesis is the main contributor to this paper. He has derived the expressions and implemented them in simulation software, performed the simulations, and wrote the paper.

II. D. Tayli, M. Cismasu, and M. Gustafsson,
"Fundamental Bounds and optimization of small antennas"
Developments in Antenna Analysis and Synthesis, edited by R. Mittra, IET, *in press*, 2018
Contributions of the author: The author of this thesis has co-written this book chapter with Marius Cismasu. Marius Cismasu has implemented the numerical simulation software and simulated the examples.

III. D. Tayli, M. Capek, L. Akrou, V. Losenicky, L. Jelinek, and M. Gustafsson,
"Accurate and Efficient Evaluation of Characteristic Modes"
IEEE Transactions on Antennas and Propagation, *submitted*, 2017
Contributions of the author: The author of this thesis is the main contributor to this paper. He has derived the expressions, implemented the simulation software, performed the simulations and co-written the paper with Miloslav Capek. The characteristic mode algorithms were implemented and simulated by Lamyae Akrou and Vitek Losenicky.

IV. J. Helander, D. Tayli, and D. Sjöberg,
"Synthesis of Large Endfire Antenna Arrays using Convex Optimization"
IEEE Transactions on Antennas and Propagation, 2017
Contributions of the author: The author of this thesis has written the main simulation software and co-implemented the compression and

acceleration algorithms with Jakob Helander. The examples and writing of the paper were done by Jakob Helander.

V. J. Helander, D. Tayli, and D. Sjöberg,
"A Comparison of Macro Basis Function Methods for Interconnected Endfire Antenna Arrays"
IEEE Antennas Wireless Propagation Letters, Vol. 16, pp. 2159–2162, 2017.
Contributions of the author: The author of this thesis has co-designed the simulation software and co-implemented the compression and acceleration algorithms with Jakob Helander. The examples and writing of the paper were done by Jakob Helander.

Other Publications by the Author

The author of this dissertation is also the author or co-author of the following publications which are related to the research topic but not considered part of the dissertation:

VI. M. Gustafsson, D. Tayli, and M. Cismasu,
"Physical Bounds of Antennas". In: *Handbook of Antenna Technologies*, edited by Z. N. Chen, Springer-Verlag, pp 1–32, 2015.

VII. M. Gustafsson, D. Tayli, C. Ehrenborg, M. Cismasu, and S. Nordebo,
"Antenna current optimization using MATLAB and CVX"
FERMAT, Vol. 15, No. 5, pp. 1–29, 2016.

VIII. K. Schab, L. Jelinek, M. Capek, C. Ehrenborg, D. Tayli, G. A. E. Vandenbosch, and M. Gustafsson,
"Energy Stored by Radiating Systems"
IEEE Access, 2018.

Acknowledgments

First and foremost, I would like to thank my supervisor Prof. Mats Gustafsson for introducing me to this exciting research path as well as for encouraging and supporting me throughout my Ph.D. education. His excellence and perfectionism in research have been an inspiration to endeavor, while his unlimited patience to my crimes of mathematical notation has been exemplary.

Second, my co-supervisor Prof. Daniel Sjöberg whom I would like to thank for being a great mentor. His industriousness and limitless energy set an example to all. I am grateful for both supervisors fostering their student's projects, the computational tool created in this work is one example.

I am lucky to have taken courses from Prof. Gerhard Kristensson whom I admire his excellence not only in research but also in teaching. Thank you for the engaging discussions and your valuable feedback throughout these years.

Working with colleagues at the Electromagnetic Theory group, Marius Cismasu, Andreas Ericsson, Casimir Ehrenborg, Jakob Helander, and Johan Lundgren, has made my doctoral studies an enjoyable journey. Also, I would like to thank my colleagues in the department Christian Nelson, Babak Mohammadi, Bo Xu, Zachary Miers, and all others whom I didn't mention by name.

I am grateful to Anders Höök, Glenn Sjöberg and Kent Falk at Saab Electronic Defense Systems, and Erik Abenius and Bo Strand at ESI for sharing their knowledge and expertise. Special thanks to Miloslav Čapek and Lukas Jelinek from Czech Technical University in Prague for the fruitful discussions and collaboration.

I am particularly grateful to the Swedish Research Council (VR) and Swedish Governmental Agency for Innovation Systems (VINNOVA) for funding this work. The research and travel grant from the Royal Physiographic Society of Lund are gratefully acknowledged. I would also like to thank Altair for the personal license of FEKO.

I would like to thank my parents who have always been there for me, backing my studies. It goes without saying that I stand where I am now with their love and support.

Last but not least, I thank my fiancée Melahat for bearing with me through both our Ph.D. journeys. Even though we were separated by a considerable distance, we managed to make the best of it and traveled around Europe having great memories together.

Lund, January 2018

Doruk Tayli

Acronyms and Abbreviations

2D	two-dimensional
ACA	adaptive cross approximation
AIM	adaptive integral method
CBF	characteristic basis function
CEM	computational electromagnetics
CM	characteristic mode
DOF	degrees-of-freedom
EEP	embedded element pattern
EFIE	electric field integral equation
FMM	fast multipole method
FOM	figure-of-merit
GA	genetic algorithm
GEP	generalized eigenvalue problem
MBF	macro basis function
MIMO	multiple-input multiple-output
MOR	model order reduction
MoM	method of moments
PEC	perfect electric conductor
RF	radio frequency
RWG	Rao-Wilton-Glisson

SF	synthetic function
SVD	singular value decomposition
TARC	total active reflection coefficient
TE	transverse electric
TM	transverse magnetic

Contents

Research Overview

Doruk Tayli

1 Introduction

Computational electromagnetics (CEM) has become a dominant tool in antenna simulations as the result of rapid increase of computational power [21,147]. Numerous computational methods are applied to antenna analysis and design, depending on the nature and complexity of the problem at hand. In some cases, high-frequency asymptotic methods and approximations are applicable while in others full-wave simulations are required [21,49]. Method of moments (MoM) is one of the techniques established as standard for full-wave simulations [21,49,147]. One of the main aims of this research is to investigate the use of CEM in antenna analysis and design. As part of this work, an in-house computational tool that implements MoM and the advanced methods presented in thesis has been developed.

1.1 Objectives and Scope

Antenna design for small platforms, such as mobile phones, is a complex process [130, 146, 153]. Usually, antennas are designed from known templates that are well tested and that can be modified or extended to meet the specifications of new designs. Antennas that are developed by editing a template usually perform satisfactorily. If these templates cannot be used to meet the specifications, a new type of antenna has to be designed. Then the antenna design cycle turns into a trial and error based process, increasing the development time and the cost of the final product. During this iterative process, knowledge of the fundamental bounds can benefit the antenna designer as it provides vital information on how far the performance of the current design is from the optimal one [63, 66, 70].

Today it is possible to compute fundamental bounds for a wide variety of antennas with the aid of new theory and computational tools [18, 58, 63, 65, 66, 70, 86, 92, 140]. But, there are still specific structures that have not yet been investigated in detail with respect to the bounds. One antenna type, essential in terminal devices, is antennas above a ground plane. This topic was previously investigated [19, 65, 133], but the canonical case of an infinite ground plane has not been studied in detail. The first article, Paper I, of the dissertation examines the fundamental bounds of this canonical geometry using stored energies [140] and convex optimization [14].

Another problem is the design and optimization of embedded antennas [130, 146]. In mobile terminal devices, the antenna is not an isolated element but a part of the whole structure; the chassis, screen, battery, *etc.* are major factors that complicates the entire design process. Consequently, the antenna element has to be investigated as part of the whole structure and not as an ideal isolated entity. The second article, Paper II, of the thesis examines the design and optimization of such embedded antenna elements using a simulation framework combining the method of moments (MoM) [21, 49, 147], genetic algorithm (GA) [82, 89] and convex optimization. Additionally, the effect of antenna placement on the wireless terminals chassis is also investigated.

Recent advances in characteristic mode (CM) decomposition for antenna analysis and synthesis has promoted CM as an important computational tool [12,15, 16,20,79,80,101,111]. CMs can be used to find the natural modes of structures, that provide valuable information about the electromagnetic behavior. Moreover, CMs can be modified to obtain different resonances or they can be combined to obtain other characteristics [15]. Although, much is known about the theory of CMs there are numerical challenges [17,79] in computing high order modes that are useful to investigate larger structures and antenna arrays. Paper III presents a new technique that calculates the CMs with higher accuracy and efficiency than the conventional method, this extends the CM computation to high order modes.

Phased arrays are arrangements of antennas used in radar applications [7]. A phased array consists of many individual antenna elements. The design of endfire phased arrays [76,96] are similarly complicated as mobile terminal antennas, but they introduce unique challenges. With respect to their electrical size while mobile terminals are small, phased arrays are large structures. Moreover, individual antenna elements in the phased array have near-field coupling effects. In endfire operation, the problems of phased arrays are exacerbated due to the strong coupling between elements and the mismatch of antenna ports. These issues restrict the applicability of numerical methods. Computational clusters are used in simulations when the number of elements in the phased array increase and the array structure expands in size. Paper IV investigates the use of macro basis function (MBF) [34,104–106,108,123] and adaptive cross approximation (ACA) [9,83,106,158] numerical methods to simulate and synthesize endfire phased arrays efficiently.

Although the investigation of phased arrays with disconnected domains using the MBF and ACA framework is a straightforward process, its application to a phased array with interconnected sub-domains is more involved [34]. The complication arises with the modeling of the current continuity across interconnected sub-domains [106,108]. Two techniques that have been used to model the current continuity with the MBF method in [106,108] are investigated in the extreme case of endfire operation in Paper V. As the endfire operation mode results in strong near-field coupling between the sub-domains, it can have a significant impact on the accuracy of the method.

1.2 Dissertation Structure

Section 2, of the *Research Overview* introduces the use of integral equation techniques in computational electromagnetics. Different tools such as image theory, spherical vector waves, and electric field integral equation (EFIE) are surveyed. The MoM and its use in solving the EFIE conclude the section. Section 3, focuses on antennas, introducing the Q-factor, stored energies, and fundamental bounds. Different computational tools utilized in the included papers antenna current optimization, characteristic modes, and the macro basis functions are briefly described in Section 4. Section 5 presents the summary of the results for each paper included in this thesis. Section 6 summarizes how the research outcome and findings match with the thesis goals. The dissertation concludes with future work in Section 7.

2 Integral Equations in Electromagnetics

Integral equations have been used in computational electromagnetics from quite early on. Maxwell himself was the first to use it to compute the capacitance of a square [109,152]. Harrington introduced the method of moments (MoM) to solve integrals equations numerically in his work [78]. Since the 80's the works [50,124] and the release of commercial software tools gave a significant boost to integral solvers used in antenna analysis and design. Currently, there is an abundance of integral equation solvers both commercial and in-house software developed by research establishments [141]. This section presents the mathematical background and tools for integral equations in the CEM field.

2.1 Definitions

This thesis, focuses on time-harmonic electromagnetic fields that are oscillating with an angular frequency, ω [21,99]. The $\mathrm{e}^{\mathrm{j}\omega t}$ time convention is used for time-harmonic quantities. Therefore the real-valued time-domain electric field $\boldsymbol{E}(\boldsymbol{r},t)$ is generated by

$$\boldsymbol{E}(\boldsymbol{r},t) = \mathrm{Re}\left\{\boldsymbol{E}(\boldsymbol{r},\omega)\mathrm{e}^{\mathrm{j}\omega t}\right\}, \tag{2.1}$$

where $\boldsymbol{E}(\boldsymbol{r},\omega)$ is the time-harmonic electric field. The ω term of time-harmonic fields is omitted to simplify the notation throughout the text. The wavenumber k is defined in terms of the angular frequency ω, permittivity ϵ, and permeability μ, as $k = \omega\sqrt{\epsilon\mu}$.

2.2 Green Function and Dyadic

George Green was a self-taught mathematician and a miller who wrote a seminal work on electromagnetism in 1828 titled, *"An essay on the application of mathematical analysis to the theories of electricity and magnetism"* [56] in which he describes the mathematical tool we call the Green function today. There is a close analogy between the impulse response in systems theory and the Green function. The impulse response models a temporal system reacting to a short impulse in time, while the Green function models a spatial system responding to a spatially focused source [35].

In electromagnetism, considering isotropic media, the free-space scalar Green function is the fundamental solution of the Helmholtz equation with radiation conditions [99]

$$\nabla^2 g(\boldsymbol{r}_1,\boldsymbol{r}_2) + k^2 g(\boldsymbol{r}_1,\boldsymbol{r}_2) = -\delta\left(\boldsymbol{r}_1 - \boldsymbol{r}_2\right) \tag{2.2}$$

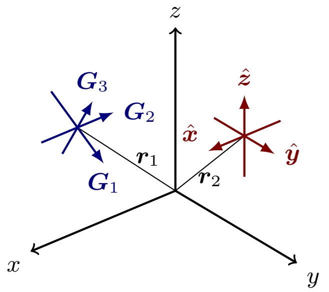

Figure 1: Infinitesimal electric dipoles directed in $\hat{\boldsymbol{x}}$, $\hat{\boldsymbol{y}}$, and $\hat{\boldsymbol{z}}$ producing the electric fields $\boldsymbol{G}_1 = \mathbf{G} \cdot \hat{\boldsymbol{x}}$, $\boldsymbol{G}_2 = \mathbf{G} \cdot \hat{\boldsymbol{y}}$, and $\boldsymbol{G}_3 = \mathbf{G} \cdot \hat{\boldsymbol{z}}$ [135].

here k is the wavenumber, $\boldsymbol{r}_1$ is the observation point, $\boldsymbol{r}_2$ is the source point, and $\delta(\boldsymbol{r})$ is the Dirac delta distribution. The scalar Green function $g(\boldsymbol{r}_1, \boldsymbol{r}_2)$ represents the outgoing wave from a unit source at $\boldsymbol{r}_2$

$$g(\boldsymbol{r}_1, \boldsymbol{r}_2) = \frac{\mathrm{e}^{-\mathrm{j}k|\boldsymbol{r}_1 - \boldsymbol{r}_2|}}{4\pi\,|\boldsymbol{r}_1 - \boldsymbol{r}_2|}. \tag{2.3}$$

The Green dyadic function, $\mathbf{G}(\boldsymbol{r}_1, \boldsymbol{r}_2)$, represents the electric field generated by an infinitesimal electric dipole [21, 99, 135] depicted in Fig. 1, and it is the outgoing solution to the vector wave Helmholtz equation [21, 99]

$$\nabla \times (\nabla \times \mathbf{G}(\boldsymbol{r}_1, \boldsymbol{r}_2)) - k^2 \mathbf{G}(\boldsymbol{r}_1, \boldsymbol{r}_2) = \mathbf{I}_3 \delta\left(\boldsymbol{r}_1 - \boldsymbol{r}_2\right) \tag{2.4}$$

and it can be expressed using the scalar Green function as

$$\mathbf{G}(\boldsymbol{r}_1, \boldsymbol{r}_2) = \left(\mathbf{I}_3 + \frac{\nabla\nabla}{k^2}\right) g(\boldsymbol{r}_1, \boldsymbol{r}_2) = \left(\mathbf{I}_3 + \frac{\nabla\nabla}{k^2}\right) \frac{\mathrm{e}^{-\mathrm{j}k|\boldsymbol{r}_1 - \boldsymbol{r}_2|}}{4\pi\,|\boldsymbol{r}_1 - \boldsymbol{r}_2|}, \tag{2.5}$$

where $\mathbf{I}_3$ is the identity dyadic. It is a mathematical tool that can be used to determine the total electric field radiated by an arbitrary distribution of currents. In case of antennas and scatterers, once the current distribution on structure is known, scattered fields can be elegantly computed using the dyadic Green function. One drawback of the form of (2.5) is the derivatives on the Green function, this hyper-singularity [21, 87, 147] poses a challenge in the evaluation of the Green dyadic when the source and observation points are near.

2.3 Image Theory

In everyday use, antennas are usually located near obstacles [7, 8, 98, 146]. For a mobile phone antenna, typical examples are a hand, a table, or the floors and walls. In case of a patch antenna, a base station, or a phased array, it is the presence of a large ground plane [7, 8, 98]. All of these obstacles influence antenna

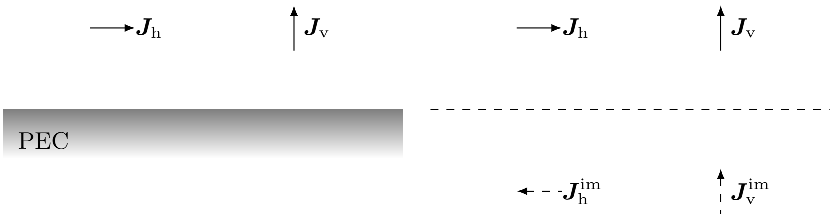

(a) with PEC plane **(b)** PEC plane removed

Figure 2: Image theory, currents above a PEC ground plane.

properties; radiation pattern, input impedance, *etc.* To solve such electromagnetic problems in the presence of obstacles the appropriate boundary conditions are added to the definition of the problem. The addition of boundary conditions usually results in a complex boundary value problem unless the geometries involved are simple canonical structures [6, 13, 78, 85, 112, 113].

Certain cases allow the use of the classical method of image theory to solve the arising complex boundary value problem. One example is the antenna above a perfectly conducting infinite ground plane, which is a canonical case [85, 87]. In image theory, the effect of the ground plane is modeled by placing imaginary sources below the ground. The addition of virtual sources permits the removal of the conducting plane, turning the whole region into free-space; although in reality, the ground is neither perfectly conducting, nor infinite in extent. These assumptions approximate the real situation accurately [7, 8].

Assuming an infinite perfect electric conductor (PEC) plane at $z = 0$ (the xy-plane) we can construct the image sources for an arbitrary current density located above the ground plane [87]. A simple way to express the current density is to decompose it into a vertical and horizontal component, $\boldsymbol{J}(\boldsymbol{r}) = \boldsymbol{J}_{\mathrm{v}}(\boldsymbol{r}) + \boldsymbol{J}_{\mathrm{h}}(\boldsymbol{r})$, therefore the image current can be expressed as

$$\boldsymbol{J}^{\mathrm{im}}(\boldsymbol{r}) = \boldsymbol{J}_{\mathrm{v}}(\boldsymbol{r}_{\mathrm{i}}) - \boldsymbol{J}_{\mathrm{h}}(\boldsymbol{r}_{\mathrm{i}}) = \hat{\boldsymbol{z}}\hat{\boldsymbol{z}} \cdot \boldsymbol{J}(\boldsymbol{r}_{\mathrm{i}}) - \left[\boldsymbol{J}(\boldsymbol{r}_{\mathrm{i}}) - \hat{\boldsymbol{z}}\hat{\boldsymbol{z}} \cdot \boldsymbol{J}(\boldsymbol{r}_{\mathrm{i}})\right], \tag{2.6}$$

where $\boldsymbol{r} = x\hat{\boldsymbol{x}} + y\hat{\boldsymbol{y}} + z\hat{\boldsymbol{z}}$ and $\boldsymbol{r}_{\mathrm{i}} = x\hat{\boldsymbol{x}} + y\hat{\boldsymbol{y}} - z\hat{\boldsymbol{z}}$ are the positions of the current density and it's image, respectively. While the $\hat{\boldsymbol{z}}$ oriented currents remain in the same direction the currents oriented in $\hat{\boldsymbol{x}}$, and $\hat{\boldsymbol{y}}$ are reversed in direction, see Fig. 2 [7, 85, 87]. The half-space dyadic Green function for this problem can then be written as [87]

$$\mathbf{G}^{\mathrm{im}}(\boldsymbol{r}_1, \boldsymbol{r}_2) = \mathbf{G}(\boldsymbol{r}_1, \boldsymbol{r}_2) - \mathbf{G}(\boldsymbol{r}_1, \boldsymbol{r}_{2\mathrm{i}}) + 2\mathbf{G}(\boldsymbol{r}_1, \boldsymbol{r}_{2\mathrm{i}}) \cdot \hat{\boldsymbol{z}}\hat{\boldsymbol{z}}. \tag{2.7}$$

Replacing the Green dyadic in an integral equation with (2.7) will convert the half-space with an infinite PEC ground plane to a free-space problem.

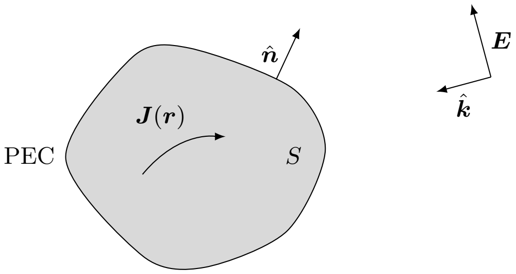

Figure 3: Scattering from a perfect electric conductor (PEC) with surface S, and outward normal vector $\hat{\boldsymbol{n}}$. The incident electric field $\boldsymbol{E}$ is propagating in the $\hat{\boldsymbol{k}}$ direction and the induced currents on the surface are denoted $\boldsymbol{J}(\boldsymbol{r})$.

2.4 Electric Field Integral Equation

Integral equations are equations containing an unknown function within an integral [6, 112]. The Fredholm equation of the first kind, is written as [6]

$$g(x) = \int_a^b K(x, y)\, f(y) \mathrm{d}y, \tag{2.8}$$

where $K(x, y)$ is the kernel, $g(x)$ is a known function, and $f(y)$ is the unknown function. The Fredholm equation of the first kind, is known to be ill-posed if $K(x, y)$ is smooth [6, 35, 112].

Integral equations have advantages over differential equations for certain scattering and antenna problems. Differential equations describe an unknown function by its local behavior, in this case, its derivatives [42]. Using this as a starting point many solutions are constructed. But, the final result is found once the boundary conditions are applied to the equation. For integral equations, the unknown function is not only related to its local values but also to all of its values in the region including the boundary conditions [6, 112]. As the boundary conditions are embedded into the equation, it is well suited for scattering and antenna problems.

In scattering or antenna problems, a current density is induced on the surface of the structure by an excitation or an incident field. The induced current density then radiates an electromagnetic field itself [21]. This phenomenon can be described using an integral equation that couples the incident electric field to the induced surface current densities, and is called the electric field integral equation (EFIE) [21, 49, 87, 147]. The total field is the sum of the scattered and incident fields. The EFIE for a PEC structure situated in free-space is [21]

$$\hat{\boldsymbol{n}} \times \boldsymbol{E}(\boldsymbol{r}_1) = \mathrm{j}k\eta_0 \hat{\boldsymbol{n}} \times \int_S \mathbf{G}(\boldsymbol{r}_1, \boldsymbol{r}_2) \cdot \boldsymbol{J}(\boldsymbol{r}_2)\, \mathrm{dS}_2 \tag{2.9}$$

where $\mathbf{G}(\boldsymbol{r}_1, \boldsymbol{r}_2)$ is the Green dyadic (2.5) (kernel), $\boldsymbol{E}(\boldsymbol{r}_1)$ is the incident electric field (known), $\boldsymbol{J}(\boldsymbol{r}_2)$ is the induced current density (unknown), η_0 is the free-space

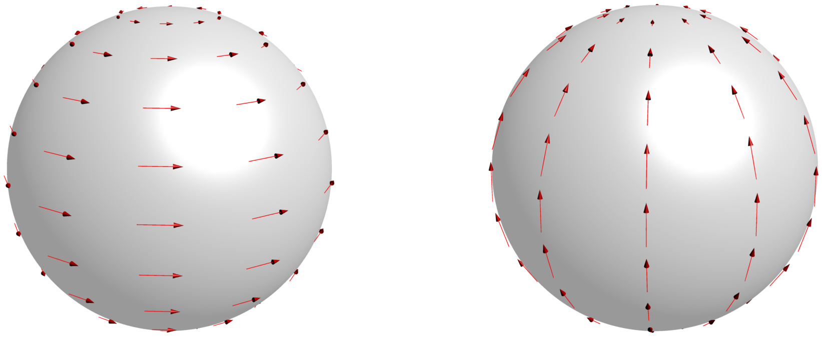

(a) $\boldsymbol{A}_{1\mathrm{e}01}\left(\hat{\boldsymbol{r}}\right)$ **(b)** $\boldsymbol{A}_{2\mathrm{e}01}\left(\hat{\boldsymbol{r}}\right)$

Figure 4: Spherical vector harmonics $\boldsymbol{A}_{\tau\mathrm{e}01}\left(\hat{\boldsymbol{r}}\right)$, $\tau = 1, 2$.

impedance, S is the surface of integration, and $\hat{\boldsymbol{n}}$ is the unit normal vector to the surface, see Fig. 3. EFIE similar to the Fredholm equation of the first kind, is ill-conditioned [21,31]. Preconditioning the EFIE to prevent dense-discretization and low-frequency breakdown is an active research area [2,4,5,24,32,71]

The fields radiated by the antenna has a special characteristic far away from the structure, also called the far-field [7,98,99]. The far-field is defined as $\boldsymbol{F}(\hat{\boldsymbol{r}}) = r\mathrm{e}^{\mathrm{j}kr}\boldsymbol{E}_{\mathrm{s}}(\boldsymbol{r})$ for $r = |\boldsymbol{r}| \to \infty$, where $\boldsymbol{E}_{\mathrm{s}}$ is the scattered electric field. The scattered field only consists of the tangential vector components $\hat{\boldsymbol{\theta}}$ and $\hat{\boldsymbol{\phi}}$, and is determined by

$$\boldsymbol{F}(\hat{\boldsymbol{r}}) = \frac{\mathrm{j}k\eta_0}{4\pi}\hat{\boldsymbol{r}} \times \int_S \hat{\boldsymbol{r}} \times \boldsymbol{J}\left(\boldsymbol{r}_2\right)\mathrm{e}^{\mathrm{j}k\hat{\boldsymbol{r}}\cdot\boldsymbol{r}_2}\mathrm{dS}_2 \tag{2.10}$$

where the direction of radiation is described by the radial unit vector $\hat{\boldsymbol{r}} = \hat{\boldsymbol{x}}\sin\theta\cos\phi + \hat{\boldsymbol{y}}\sin\theta\sin\phi + \hat{\boldsymbol{z}}\cos\theta$.

2.5 Spherical Vector Waves

An important mathematical tool in electromagnetics is the spherical vector waves [29,72,99,113,135]. These are the solution of Maxwell's equations in a spherical coordinate system (r, θ, ϕ). As spherical vector waves are used throughout the disseration we give a short introduction here, for details see [72,75,99,113,135,148].

Total electromagnetic field outside of a circumscribing sphere can be represented as an expansion of spherical vector waves [99],

$$\boldsymbol{E}(\boldsymbol{r}) = \sum_{\alpha}\left(a_\alpha\boldsymbol{v}_\alpha\left(k\boldsymbol{r}\right) + f_\alpha\boldsymbol{u}_\alpha\left(k\boldsymbol{r}\right)\right), \tag{2.11}$$

where a_α and f_α are respectively the expansion coefficients of the incident and scattered field; $\boldsymbol{v}_\alpha\left(k\boldsymbol{r}\right)$ and $\boldsymbol{u}_\alpha\left(k\boldsymbol{r}\right)$ are the regular and outgoing spherical vector waves [72, 99, 113, 148], respectively. The multi-index α for real-valued spherical vector waves are ordered as [68, 72],

$$\alpha\left(\tau,\sigma,m,l\right)=2\left(l^2+l-1+\left(-1\right)^s m\right)+\tau, \tag{2.12}$$

where the sub-indices are; $\tau\in\{1,2\}$, $m\in\{0,\dots,l\}$, $l\in\{1,\dots,L\}$, $s=0$ for even azimuth functions ($\sigma=\mathrm{e}$), and $s=1$ for odd azimuth functions ($\sigma=\mathrm{o}$). Sub-indices of α; σ, l, m define a multipole expansion of order l while the τ index represents either a transverse electric (TE) wave $\tau=1$, or a transverse magnetic (TM) wave $\tau=2$. Total number of spherical modes is $N_\alpha=2L(L+2)$. The TE and TM modes of the vector spherical harmonics are depicted for $m=0$ and $l=1$ in Fig. 4. The magnetic field is expressed with the use of $\nabla\times\boldsymbol{v}_\alpha\left(k\boldsymbol{r}\right)=k\boldsymbol{v}_{\bar\alpha}\left(k\boldsymbol{r}\right)$, and $\nabla\times\boldsymbol{u}_\alpha\left(k\boldsymbol{r}\right)=k\boldsymbol{u}_{\bar\alpha}\left(k\boldsymbol{r}\right)$ where $\bar\alpha=\{\bar\tau\sigma ml\}$ is the dual index to τ, defined as $\bar 1=2$ and $\bar 2=1$ [99]. The expansion of the magnetic field is then,

$$\boldsymbol{H}(\boldsymbol{r})=-\frac{1}{\mathrm{j}\eta}\sum_\alpha\left(a_\alpha\boldsymbol{v}_{\bar\alpha}\left(k\boldsymbol{r}\right)+f_\alpha\boldsymbol{u}_{\bar\alpha}\left(k\boldsymbol{r}\right)\right). \tag{2.13}$$

Representing the scattered fields as an expansion of spherical vector waves, is advantageous as it can be used to compute the radiated far-field in an efficient manner. The radiated far-field is written using the vector spherical harmonics $\boldsymbol{A}_{\tau\sigma ml}\left(\hat{\boldsymbol{r}}\right)$, components of the vector spherical waves, as [99]

$$\boldsymbol{F}\left(\hat{\boldsymbol{r}}\right)=-\frac{1}{\mathrm{j}k}\sum_\alpha\left(-\mathrm{j}\right)^{-l+\tau-1}f_\alpha\boldsymbol{A}_{\tau\sigma ml}\left(\hat{\boldsymbol{r}}\right), \tag{2.14}$$

and the expansion coefficients can be determined from

$$f_\alpha=\left(-\mathrm{j}\right)^{l+2-\tau}k\int_\Omega\boldsymbol{A}_{\tau\sigma ml}\left(\hat{\boldsymbol{r}}\right)\cdot\boldsymbol{F}\left(\hat{\boldsymbol{r}}\right)\mathrm{d}\Omega, \tag{2.15}$$

where $\mathrm{d}\Omega$ is the element of solid angle and the integral is over the unit sphere Ω. Total radiated power is expressed as

$$P_\mathrm{r}=\frac{\eta}{32\pi^2}\sum_\alpha\left|f_\alpha\right|^2. \tag{2.16}$$

Spherical vector waves can also be used to expand the Green dyadic (2.5) for all $\boldsymbol{r}_1\neq\boldsymbol{r}_2$ as [99]

$$\mathbf{G}(\boldsymbol{r}_1,\boldsymbol{r}_2)=-\mathrm{j}k\sum_\alpha\boldsymbol{v}_\alpha\left(k\boldsymbol{r}_<\right)\boldsymbol{u}_\alpha\left(k\boldsymbol{r}_>\right)=-\mathrm{j}k\sum_\alpha\boldsymbol{u}_\alpha\left(k\boldsymbol{r}_>\right)\boldsymbol{v}_\alpha\left(k\boldsymbol{r}_<\right), \tag{2.17}$$

where $\boldsymbol{r}_<$ is the smaller of $\boldsymbol{r}_1$ and $\boldsymbol{r}_2$ and $\boldsymbol{r}_>$ is the larger of $\boldsymbol{r}_1$ and $\boldsymbol{r}_2$. This expansion can be utilized for fast multipole methods used in large scale CEM [22, 28, 132].

The Green dyadic of the EFIE (2.9) can be substituted with the spherical vector wave expansion in (2.17)

$$\hat{\boldsymbol{n}} \times \boldsymbol{E}(\boldsymbol{r}_1) = k^2 \eta_0 \hat{\boldsymbol{n}} \times \sum_{\alpha} \int_S \boldsymbol{u}_\alpha (k\boldsymbol{r}_>) \, \boldsymbol{v}_\alpha (k\boldsymbol{r}_<) \cdot \boldsymbol{J}(\boldsymbol{r}_2) \, \mathrm{dS}_2$$

assuming $\boldsymbol{r}_1 \neq \boldsymbol{r}_2$ and selecting $\boldsymbol{r}_< = \boldsymbol{r}_1$ and $\boldsymbol{r}_> = \boldsymbol{r}_2$ the equation becomes

$$\begin{aligned} \hat{\boldsymbol{n}} \times \boldsymbol{E}(\boldsymbol{r}_1) &= k^2 \eta_0 \hat{\boldsymbol{n}} \times \sum_{\alpha} \boldsymbol{u}_\alpha (k\boldsymbol{r}_1) \int_S \boldsymbol{v}_\alpha (k\boldsymbol{r}_2) \cdot \boldsymbol{J}(\boldsymbol{r}_2) \, \mathrm{dS}_2 \\ &= \hat{\boldsymbol{n}} \times \sum_{\alpha} f_\alpha \boldsymbol{u}_\alpha (k\boldsymbol{r}_1), \end{aligned} \tag{2.18}$$

where

$$f_\alpha = k^2 \eta_0 \int_S \boldsymbol{v}_\alpha (k\boldsymbol{r}) \cdot \boldsymbol{J}(\boldsymbol{r}) \, \mathrm{dS} \tag{2.19}$$

is the projection of the current density onto regular spherical vector waves. The resulting equation is similar to (2.11).

2.6 Method of Moments

Analytical solutions to integral equations arising in antenna analysis exist only for a set of simple shapes [13, 97, 113, 125]. In practice, most if not all antennas do not fit into this small set of geometries. Approximate methods are employed to analyze complicated antenna structures [78]. One of the main techniques to solve integral equations is the method of moments (MoM) [21, 78, 87]. In MoM, the integral operator is turned into a linear system of equations which is then solved using matrix theory [21, 49, 78, 147].

An integral equation such as the EFIE can be represented as an operator $\mathcal{L}$ acting on a function f,

$$\mathcal{L}(f) = g \tag{2.20}$$

here g is a known function called the source or excitation, and f is the response function to be determined. To solve this problem we represent the unknown f as

$$f = \sum_n f_n \psi_n, \tag{2.21}$$

where ψ_n are known *basis functions* and f_n are the unknown coefficients. For a compact operator, a finite set of functions can approximate the solution space [21]. Here the behavior of the f function is represented by a finite set of functions. Inserting the expanded (2.21) function into (2.20) and assuming that $n = 1, \cdots, N$ we get

$$\sum_{n=1}^{N} f_n \mathcal{L}(\psi_n) = g \tag{2.22}$$

yielding an equation with N unknowns. Now the equation is tested with *testing functions* w. One common testing function choice is $w_n = \psi_n$ that is referred as Galerkin's method [93]. Once the (2.22) is tested with testing functions it results in a linear system of equations

$$\sum_{n}^{N} f_n \left\langle w_m, \mathcal{L}\left(\psi_n\right)\right\rangle = \left\langle w_m, g\right\rangle, \tag{2.23}$$

where $\langle f, g\rangle$ is defined as a suitable inner product [78]. The linear system of (2.23) can be written in matrix form

$$\mathbf{Lf} = \mathbf{g}, \tag{2.24}$$

where the $\mathbf{L}$ and $\mathbf{g}$ are

$$L_{mn} = \left\langle w_m, \mathcal{L}\left(\psi_n\right)\right\rangle, \tag{2.25}$$

$$g_n = \left\langle w_n, g\right\rangle, \tag{2.26}$$

and $\mathbf{f}$ is the column vector containing the unknown coefficients f_n. The matrix equation (2.24) can be solved using a linear system solver [52, 134].

2.7 Solving the EFIE with MoM

The EFIE presented in Section 2.4 can be solved using the MoM described in-Section 2.6. For a PEC structure the magnetic current densities on the surface are $\boldsymbol{M} = -\hat{\boldsymbol{n}} \times \boldsymbol{E} = 0$, therefore only electric current densities, $\boldsymbol{J}$, reside on the surface. These current densities are expanded using basis functions $\boldsymbol{\psi}\left(\boldsymbol{r}\right)$, as

$$\boldsymbol{J}\left(\boldsymbol{r}\right) = \sum_{n=1}^{N} I_n \boldsymbol{\psi}_n\left(\boldsymbol{r}\right) \tag{2.27}$$

here $\boldsymbol{\psi}_n(\boldsymbol{r})$ and I_n are the n^{th} basis function and expansion coefficient, while N is the total number of basis functions, also called the total degrees-of-freedom (DOF) [21].

Following the solution in Section 2.6, basis functions are used to expand the current densities, by inserting (2.27) into (2.9), in an identical manner to (2.22). The resulting equation is later tested using $\hat{\boldsymbol{n}} \times \boldsymbol{\psi}_m\left(\boldsymbol{r}\right)$ testing functions and using the inner product

$$\langle \boldsymbol{f}, \boldsymbol{g}\rangle = \int_S \boldsymbol{f}^*(\boldsymbol{r}) \cdot \boldsymbol{g}(\boldsymbol{r}) \mathrm{dS}, \tag{2.28}$$

where * denotes the complex conjugate. The final equation becomes [21],

$$\int_S \boldsymbol{\psi}_m\left(\boldsymbol{r}_1\right) \cdot \boldsymbol{E}\left(\boldsymbol{r}_1\right) \mathrm{dS}_1 = \mathrm{j}k\eta_0 \int_S \int_S \boldsymbol{\psi}_m\left(\boldsymbol{r}_1\right) \cdot \mathbf{G}(\boldsymbol{r}_1, \boldsymbol{r}_2) \cdot \boldsymbol{\psi}_n\left(\boldsymbol{r}_2\right) \mathrm{dS}_1 \mathrm{dS}_2. \tag{2.29}$$

As there are N basis and test functions in (2.29), the system of equations can be written in matrix form as

$$\mathbf{ZI} = \mathbf{V}, \tag{2.30}$$

where $\mathbf{I} \in \mathbb{C}^{N\times 1}$ is a column vector of unknown current density coefficients, $\mathbf{V} \in \mathbb{C}^{N\times 1}$ is the excitation column vector, and $\mathbf{Z} \in \mathbb{C}^{N\times N}$ is the impedance matrix. Individual elements of $\mathbf{Z}$ and $\mathbf{V}$ are

$$Z_{mn} = \mathrm{j}k\eta_0 \int_S \int_S \boldsymbol{\psi}_m(\boldsymbol{r}_1) \cdot \mathbf{G}(\boldsymbol{r}_1, \boldsymbol{r}_2) \cdot \boldsymbol{\psi}_n(\boldsymbol{r}_2)\, \mathrm{dS}_1 \mathrm{dS}_2, \tag{2.31}$$

and

$$V_m = \int_S \boldsymbol{\psi}_m(\boldsymbol{r}) \cdot \boldsymbol{E}(\boldsymbol{r})\, \mathrm{dS}. \tag{2.32}$$

Surface currents density coefficient vector $\mathbf{I}$, induced by the excitation $\mathbf{V}$, is found once the system of equations in (2.30) is solved. These coefficients are then used to compute radiated fields and far-field, circuit parameters such as input impedance and s-parameters. The radiated far-field is found by substituting (2.27) into (2.10)

$$\boldsymbol{F}(\hat{\boldsymbol{r}}) = \frac{-\mathrm{j}k\eta_0}{4\pi} \sum_n^N I_n \int_S \boldsymbol{\psi}_n(\boldsymbol{r}_2)\, \mathrm{e}^{\mathrm{j}k\hat{\boldsymbol{r}}\cdot\boldsymbol{r}_2} \mathrm{dS}_2. \tag{2.33}$$

The impedance matrix can be expressed as a sum of its real and imaginary parts

$$\mathbf{Z} = \mathbf{R} + \mathrm{j}\mathbf{X}, \tag{2.34}$$

where $\mathbf{R}$ is the resistance matrix, $\mathbf{X}$ is the reactance matrix. The matrix $\mathbf{R}$ is positive-semidefinite in theory [78], but it is often indefinite when computed with finite precision [17,66,136], see Appendix B. The indefiniteness of $\mathbf{R}$ causes a problem in modal decompositions, limiting the number of correct calculated modes. It is possible to circumvent this with the use of the spherical vector wave expansion of the Green dyadic (2.17), see Section 4.2.

Expansion of the Green dyadic in spherical vector waves (2.17) can be used to factorize the EFIE into a product of two integrals

$$\begin{aligned} Z_{mn} &= k^2\eta_0 \sum_\alpha \int_S \int_S \boldsymbol{\psi}_m(\boldsymbol{r}_1) \cdot \boldsymbol{v}_\alpha(k\boldsymbol{r}_<)\, \boldsymbol{u}_\alpha(k\boldsymbol{r}_>) \cdot \boldsymbol{\psi}_n(\boldsymbol{r}_2)\, \mathrm{dS}_1 \mathrm{dS}_2 \\ &= k^2\eta_0 \sum_\alpha \int_S \boldsymbol{\psi}_m(\boldsymbol{r}_1) \cdot \boldsymbol{v}_\alpha(k\boldsymbol{r}_1)\, \mathrm{dS}_1 \int_S \boldsymbol{u}_\alpha(k\boldsymbol{r}_2) \cdot \boldsymbol{\psi}_n(\boldsymbol{r}_2)\, \mathrm{dS}_2 \end{aligned} \tag{2.35}$$

where it is assumed that $|\boldsymbol{r}_1| < |\boldsymbol{r}_2|$. The factorized integral expressions are

$$S_{\alpha n} = k\sqrt{\eta_0} \int_S \boldsymbol{\psi}_n(\boldsymbol{r}) \cdot \boldsymbol{v}_\alpha(k\boldsymbol{r})\, \mathrm{dS} \tag{2.36}$$

and

$$Q_{\alpha n} = k\sqrt{\eta_0}\int_S \boldsymbol{\psi}_n\left(\boldsymbol{r}\right)\cdot \boldsymbol{u}_\alpha\left(k\boldsymbol{r}\right)\mathrm{dS} \tag{2.37}$$

resembling the integrals in the T-matrix method that use spherical vector waves as basis and testing functions [99, 148]. This factorization presents many opportunities in the computation of the far-field, characteristic modes, and impedance matrix. Using (2.35), the matrix $\mathbf{R}$ can be decomposed as,

$$\mathbf{R} = \mathbf{S}^{\mathrm{H}}\mathbf{S} = \mathbf{S}^{\mathrm{T}}\mathbf{S} \tag{2.38}$$

as the matrix $\mathbf{S}\in\mathbb{R}^{N_\alpha\times N}$ is real-valued, and $\boldsymbol{v}_\alpha\left(k\boldsymbol{r}\right) = \mathrm{Re}\{\boldsymbol{u}_\alpha\left(k\boldsymbol{r}\right)\}$. Transpose and Hermitian transpose matrix operation are indicated as $^{\mathrm{T}}$ and $^{\mathrm{H}}$, respectively. The factorization (2.38) and its use in characteristic mode decomposition is discussed in Paper III. The radiated far-field can be computed using $\mathbf{S}$ with the spherical vector wave expansion coefficients (2.19) as

$$\mathbf{F}_\alpha = \mathbf{S}\mathbf{I}, \tag{2.39}$$

where the column matrix $\mathbf{F}_\alpha\in\mathbb{C}^{N_\alpha\times 1}$ consists of the coefficients f_α that are identical to (2.15) and (2.19). Radiated far-field and total radiated power are found using (2.14) and (2.16), respectively. Computing the radiated far-field using $\mathbf{S}$ has two main advantages, decrease in computation time, and continuous representation of the far-field. When the far-field is computed using (2.33), a unit sphere is sampled with N_θ and N_ϕ points for the θ and ϕ angles and the integral is calculated $N_\theta N_\phi$ times. The use of the matrix $\mathbf{F}_\alpha$ increases the computation speed of both quantities, the far-field and the radiated power, significantly. Integrals are replaced by the evaluation of the spherical vector harmonics on the unit sphere and a matrix multiplication for the far-field and only the f_α coefficients are required for the total radiated power.

2.8 Implementation of MoM

Until this step, no specific detail has been given for the basis function other than it should model the behavior of electric current. Notably, the choice of basis function depends on the problem geometry. For instance, global basis functions, vector spherical harmonics, can be used to represent $\boldsymbol{\psi}(\boldsymbol{r})$ on a sphere [99]. In case of arbitrary geometries, global basis functions may not exist; therefore the whole structure is discretized, split up into smaller pieces, and basis functions are applied to these simpler parts. This procedure known as meshing may use a variety of shapes including quadrilaterals, triangles, or higher order geometries [21, 147]. Usually, triangular elements are preferred as they describe arbitrary surfaces in better detail than rectangular elements.

Rao-Wilton-Glisson (RWG) [124] basis functions are widely used in integral equation solvers for triangular meshes [21, 35]. The RWG basis function is illustrated in Fig. 5a. These are first order divergence conforming linear basis

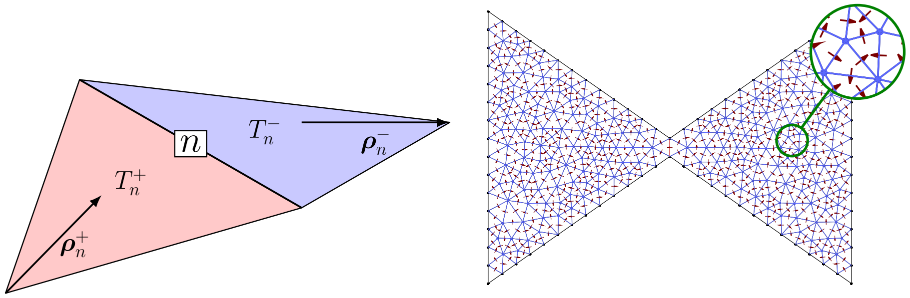

(a) RWG **(b)** bowtie

Figure 5: (a) Definition of RWG basis function, (b) bowtie antenna meshed with triangular elements and RWG current densities are depicted with red arrows.

functions that span two triangle elements, with the currents confined to triangular surfaces. Specifically for the n^{th} basis the current exits from the triangle T_n^+ and enters the triangle T_n^-. Therefore, each shared edge between triangles is assigned an RWG basis function. Fig. 5b illustrates a bowtie antenna meshed with triangular basis elements; the red arrow indicates individual RWG basis functions assigned to shared triangle edges. RWG basis functions are defined as [124]

$$\boldsymbol{\psi}_n(\boldsymbol{r}) = \begin{cases} \dfrac{\ell_n}{2A_n^{\pm}}\boldsymbol{\rho}^{\pm}(\boldsymbol{r}), & \boldsymbol{r} \in T_n^{\pm} \\ 0, & \text{otherwise} \end{cases} \tag{2.40}$$

here ℓ_n is the length of the shared edge, $A_n^{\pm}$ is the area of the corresponding triangle, and the vectors $\boldsymbol{\rho}_n^{\pm}$ are depicted in Fig. 5a.

Elements of the impedance matrix $\mathbf{Z}$, are challenging to compute when basis and test functions overlap, $\boldsymbol{r}_1 \approx \boldsymbol{r}_2$, as the Green function, see Section 2.2, is singular [35,49]. When the source and observation points are well separated, the integral can be computed using numerical quadrature. A standard method is to use barycentric coordinates to integrate over triangular surfaces, see Appendix A. The numerical integration can then be performed using symmetrical Gaussian quadrature points and weights [36].

There have been many investigations about evaluating singular integrals in the CEM community [38,54,84,95,115–117,120,121,144,151]. The primary techniques are singularity subtraction and change of variables. In the first method, the real part of the Green function that contains the singularity is subtracted, and the remaining non-singular integral is computed numerically. The latter removes the $1/R$ term in the Green function by a change of variables.

Regarding the implementation of singularity algorithms, there are certain aspects that should be carefully considered. The first is the accuracy; as singularity removal techniques differ in convergence rates. The trade-off between accuracy and speed, as high number of quadrature points may be required for convergence. Lastly, from an implementation aspect, using existing singularity libraries shortens development time and effort. Two noteworthy libraries developed specifically for this purpose are DEMCEM [118] and DIRECTFN [119].

In antenna analysis, the antenna is usually excited with a radio frequency (RF) port or incoming waves. A straightforward representation of an antenna port is the delta-gap excitation. Here the two triangles, $T_n^{\pm}$, of a RWG are separated with an infinitesimal gap and, a voltage difference is applied to the edges. Assuming the excitation is placed on the i^{th} basis, the delta-gap excitation is then the applied electric field intensity, that is the voltage normalized by the edge length ℓ_i of the RWG basis function.

3 Antenna Terms and Definitions

3.1 Q-factor

The Q-factor is an important figure-of-merit (FOM) to quantify the performance and physical limitations of antennas [30, 73]. The general definition of the Q-factor is the ratio of the time averaged stored energies over the dissipated power [43,146,156]. This parameter can be used to describe a plethora of oscillating systems, from antennas [25,146,149] and filters [114,122,126] to mechanical oscillations of cantilevers [1]. In antennas, a high Q-factor indicates large reactive fields near the radiating structure, which leads to high amplitude currents, narrow bandwidth, and conduction losses [30]. For an interesting side-note, although Q-factor is also called as the *quality-factor*, the letter "Q" was selected by Johnson in 1920 for the sole reason that all the other letters were excessively used [131].

The use of Q-factor in antennas originates from its relation to the fractional bandwidth when the system is narrow-band and has a single resonance frequency [156]. In the early days, antennas operated at long wavelengths, due to the lack of high-frequency electronics [7, 146]. For an antenna to operate efficiently its electrical size should be approximately half-a-wavelength [73,130,146]. As it was infeasible to operate such large structures, due to conduction losses and structural constraints, many antennas were electrically small in size. The optimal performance of these electrically small antennas kindled interest in the investigation of antenna physical bounds [25, 30, 43, 149].

For an antenna, tuned or untuned, the Q-factor is defined as [43, 77, 110, 156]

$$Q = \frac{2\omega \max\{W_{\mathrm{e}}, W_{\mathrm{m}}\}}{P_{\mathrm{d}}}, \tag{3.1}$$

where W_{e} and W_{m} are the time averaged stored electric and magnetic energies, respectively, and P_{d} is the dissipated power. The dissipated power for a conducting antenna is the sum of ohmic losses P_{Ω} and radiation losses P_{r},

$$P_{\mathrm{d}} = P_{\Omega} + P_{\mathrm{r}}. \tag{3.2}$$

For a lossless antenna, dissipated power equals total radiated power from the antenna. As stored energies appear in (3.1), their accurate computation has been investigated for various antennas, see Section 3.2.

While the Q-factor can be calculated using stored energies, it is also possible to approximate it with classical circuit theory. Therefore, a brief introduction of the antenna circuit parameters are outlined here. An antenna can be represented as a one-port network [122] with the input impedance expressed as [7,78,98,122]

$$Z_{\mathrm{in}}(\omega) = R_{\mathrm{in}}(\omega) + \mathrm{j}X_{\mathrm{in}}(\omega) \tag{3.3}$$

here the input impedance is frequency dependent and $R_{\mathrm{in}}(\omega)$ is the input resistance and $X_{\mathrm{in}}(\omega)$ is the input reactance. $R_{\mathrm{in}}(\omega)$ is the sum of the radiation resistance and the loss resistance of the antenna, and with only conductive losses it is $R_{\mathrm{in}}(\omega) = R_{\mathrm{r}}(\omega) + R_{\Omega}(\omega)$. The conductive, resistive, loss can be modeled as a skin depth or a resistive sheet $R_{\mathrm{s}} = 1/\sigma d$, where σ is the conductivity and d is the thickness [129]. Another parameter, the reflection coefficient Γ of an antenna is defined as

$$\Gamma = \frac{Z - Z_0}{Z + Z_0}, \tag{3.4}$$

where Z_0 is the normalization impedance. In this thesis the antenna bandwidth is defined as the frequency range where the magnitude of the antenna reflection coefficient is less than or equal to a threshold magnitude Γ_0. For narrow-band single resonance systems, the Q-factor is proportional to the fractional bandwidth of the system [156]

$$Q_{\mathrm{FBW}} = \frac{2\Gamma_0}{\sqrt{1-\Gamma_0^2}}\frac{1}{B}, \tag{3.5}$$

where B is the fractional bandwidth. Another useful approximation of the Q-factor is the angular frequency derivative of the input impedance Z_{in} [156]

$$Q_{\mathrm{Z}'_{\mathrm{in}}} = \frac{\omega\,|Z'_{\mathrm{in}}|}{2R_{\mathrm{in}}}, \tag{3.6}$$

where the antenna is tuned to resonance with an inductor or capacitor. Both (3.5) and (3.6) are convenient to approximate the Q-factor for electrically small antennas [128]. It should be noted that Q-factor obtained from the derivative in (3.6) is a local approximation and can give incorrect values for special cases [69].

3.2 Stored Energies

The fields surrounding an antenna can be separated into two waves one propagating and the other non-propagating [110]. Propagating fields are similar to traveling waves in an infinitely long lossless transmission line, where the waves travel to infinity; whereas non-propagating reactive fields are localized near the antenna [25,30,110]. Energies stored in the non-propagating reactive fields resemble the energies stored in capacitors and inductors in electric circuits [66,70]. One significant difference from the circuit analogy is that the two waves, propagating and non-propagating, are difficult to separate [25, 30, 43].

The total energy for an antenna in free-space excited with a time-harmonic signal is unbounded, as the fields decay proportionally to $1/r$ [25, 43, 110]. Moreover, the energy is not linear in terms of field components resulting in coupled energy terms and removing the possibility of superposition. Since Chu's initial work in 1948 [25], computation of stored energies has been investigated in several works [30, 43, 48, 60, 61, 94, 110, 139, 140, 143, 149, 154, 156]. A through literature review and investigation of the different stored energy estimation methods has been conducted by Schab *et al.* [128].

This thesis uses the stored energy expressions of Vandenbosch [140], which are suitable to use in antenna current optimization [63, 67], see Section 4.1. These expressions are obtained by subtracting the radiated energy density from the total energy density, and are defined for electric current densities situated in free-space [61, 140]. Integral expressions for the stored electrical and magnetic energy are

$$W_{\mathrm{e}} = \frac{\eta_0}{4\omega}\int_V\int_V \nabla_1\cdot\boldsymbol{J}(\boldsymbol{r}_1)\nabla_2\cdot\boldsymbol{J}^*(\boldsymbol{r}_2)\frac{\cos\left(k\left|\boldsymbol{r}_1-\boldsymbol{r}_2\right|\right)}{4\pi k\left|\boldsymbol{r}_1-\boldsymbol{r}_2\right|}\mathrm{dV}_1\mathrm{dV}_2 - W_{\mathrm{cor}} \qquad (3.7)$$

and

$$W_{\mathrm{m}} = \frac{\eta_0}{4\omega}\int_V\int_V k\boldsymbol{J}(\boldsymbol{r}_1)\cdot\boldsymbol{J}^*(\boldsymbol{r}_2)\frac{\cos\left(k\left|\boldsymbol{r}_1-\boldsymbol{r}_2\right|\right)}{4\pi\left|\boldsymbol{r}_1-\boldsymbol{r}_2\right|}\mathrm{dV}_1\mathrm{dV}_2 - W_{\mathrm{cor}} \qquad (3.8)$$

where V is the volume occupied by the antenna, and W_{cor} is the correction term

$$W_{\mathrm{cor}} = \frac{\eta_0}{4\omega}\int_V\int_V \left(k^2\boldsymbol{J}(\boldsymbol{r}_1)\cdot\boldsymbol{J}^*(\boldsymbol{r}_2) - \nabla_1\cdot\boldsymbol{J}(\boldsymbol{r}_1)\nabla_2\cdot\boldsymbol{J}^*(\boldsymbol{r}_2)\right) \frac{\sin\left(k\left|\boldsymbol{r}_1-\boldsymbol{r}_2\right|\right)}{8\pi}\mathrm{dV}_1\mathrm{dV}_2. \qquad (3.9)$$

Total radiated power is computed using the following integral expression [61, 140]

$$P_{\mathrm{r}} = \frac{\eta_0}{2}\int_V\int_V \left(k^2\boldsymbol{J}(\boldsymbol{r}_1)\cdot\boldsymbol{J}^*(\boldsymbol{r}_2) - \nabla_1\cdot\boldsymbol{J}(\boldsymbol{r}_1)\nabla_2\cdot\boldsymbol{J}^*(\boldsymbol{r}_2)\right) \frac{\sin(k\left|\boldsymbol{r}_1-\boldsymbol{r}_2\right|)}{4\pi k\left|\boldsymbol{r}_1-\boldsymbol{r}_2\right|}\mathrm{dV}_1\mathrm{dV}_2. \qquad (3.10)$$

Using the integral expressions (3.7), (3.8), and (3.10), it is possible to compute the Q-factor for arbitrary current distributions with (3.1). Other quantities of interest are the partial radiation intensity [66]

$$P(\hat{\boldsymbol{r}},\hat{\boldsymbol{e}}) = \frac{\left|\hat{\boldsymbol{e}}^*\cdot\boldsymbol{F}(\hat{\boldsymbol{r}})\right|^2}{2\eta_0} \qquad (3.11)$$

and the partial gain

$$G(\hat{\boldsymbol{r}},\hat{\boldsymbol{e}}) = \frac{4\pi P(\hat{\boldsymbol{r}},\hat{\boldsymbol{e}})}{P_{\mathrm{d}}} \tag{3.12}$$

where $\hat{\boldsymbol{e}}$ is the polarization direction. For a lossless antenna the partial directivity $D(\hat{\boldsymbol{r}},\hat{\boldsymbol{e}})$, equals the partial gain $G(\hat{\boldsymbol{r}},\hat{\boldsymbol{e}})$.

Computing the Stored Energies

Stored energies can be computed for arbitrarily shaped antennas in free-space using the Vandenbosch integral expressions (3.7)–(3.10). The current densities in (3.7), (3.8), and (3.10) are replaced with (2.27) resulting in the quadratic forms [66, 70]

$$W_{\mathrm{e}} \approx \frac{1}{4\omega}\mathbf{I}^{\mathrm{H}}\mathbf{X}_{\mathrm{e}}\mathbf{I}, \tag{3.13}$$

$$W_{\mathrm{m}} \approx \frac{1}{4\omega}\mathbf{I}^{\mathrm{H}}\mathbf{X}_{\mathrm{m}}\mathbf{I}, \tag{3.14}$$

and

$$P_{\mathrm{r}} \approx \frac{1}{2}\mathbf{I}^{\mathrm{H}}\mathbf{R}\mathbf{I}, \tag{3.15}$$

where $\mathbf{X}_{\mathrm{e}}$ and $\mathbf{X}_{\mathrm{m}}$ are the electric and magnetic reactance matrices; they are related to the reactance matrix by the subtraction $\mathbf{X} = \mathbf{X}_{\mathrm{e}} - \mathbf{X}_{\mathrm{m}}$, and $\mathbf{R}$ is the real part of the impedance matrix. While the reactance matrix $\mathbf{X}$ is indefinite, the matrices $\mathbf{X}_{\mathrm{e}}$ and $\mathbf{X}_{\mathrm{m}}$ are positive semi-definite for electrically small structures [61, 63, 67], these quadratic forms are also used in antenna current optimization, see Section 4.1. The Q-factor of a lossless antenna is then computed using the quadratic energy expressions and the total radiated power as

$$Q \approx \frac{\max\{\mathbf{I}^{\mathrm{H}}\mathbf{X}_{\mathrm{e}}\mathbf{I}, \mathbf{I}^{\mathrm{H}}\mathbf{X}_{\mathrm{m}}\mathbf{I}\}}{\mathbf{I}^{\mathrm{H}}\mathbf{R}\mathbf{I}}. \tag{3.16}$$

Altenatively, stored energies can be expressed with impedance matrix (2.31) and its derivative with respect to the angular frequency as [66, 70, 81]

$$W_{\mathrm{e}} \approx \frac{1}{8}\mathbf{I}^{\mathrm{H}}\left(\frac{\partial\mathbf{X}}{\partial\omega} - \frac{\mathbf{X}}{\omega}\right)\mathbf{I} = \frac{1}{4\omega}\mathbf{I}^{\mathrm{H}}\mathbf{X}_{\mathrm{e}}\mathbf{I} \tag{3.17}$$

and

$$W_{\mathrm{m}} \approx \frac{1}{8}\mathbf{I}^{\mathrm{H}}\left(\frac{\partial\mathbf{X}}{\partial\omega} + \frac{\mathbf{X}}{\omega}\right)\mathbf{I} = \frac{1}{4\omega}\mathbf{I}^{\mathrm{H}}\mathbf{X}_{\mathrm{m}}\mathbf{I}. \tag{3.18}$$

The tuned Q-factor of an antenna can then be written using the derivative of the rectance matrix as

$$Q \approx \frac{\omega\mathbf{I}^{\mathrm{H}}\mathbf{X}'\mathbf{I} + \left|\mathbf{I}^{\mathrm{H}}\mathbf{X}\mathbf{I}\right|}{2\mathbf{I}^{\mathrm{H}}\mathbf{R}\mathbf{I}}. \tag{3.19}$$

where $'$ denotes differentiation with respect to the angular frequency ω.

3.3 Fundamental Bounds

The investigation of electrically small antenna bounds started around the 40's with the works of Wheeler [149] and Chu [25]. The classical results of Chu [25] were derived for a lossless antenna enclosed by a sphere of radius a. In Chu's derivation, arbitrary current distribution and zero reactive fields were assumed inside the sphere and spherical vector waves represented the fields outside the sphere. The stored energies and Q-factor were computed, ingeniously, using circuit equivalents to the spherical vector waves, and directivity over Q-factor quotient, D/Q, bounds were derived. A majority of later works also employed the mode expansion approach to determine the bounds [30, 43, 48, 62, 74, 77, 94, 110, 139, 156]. The intuition gained from this approach was that the spherical volume enclosing the antenna should be efficiently utilized to achieve maximal bandwidth [7, 10, 25].

Another strategy in determining the bounds was introduced in [59, 64, 65]. Forward scattering sum rule was employed to bound the D/Q quotient for arbitrarily shaped antennas, using the causality, time-translational invariance, and reciprocity of the problem. It was derived in [65], that the D/Q is bounded by the electric and magnetic polarizabilities of an antenna. Utilizing a different approach, these results were later extended to electric and magnetic polarizability dyadics in [90]. One interesting outcome is that the antenna performance is bounded by the static behavior of the geometry. For an electric dipole, TM, the D/Q bounds can be reached by maximizing the electric polarizability dyadic, that physically corresponds to increasing the separation of charge on the structure.

Antenna current optimization has been employed in [63, 66] to compute the physical bounds from optimal current distributions. The utilization of current density distribution on the antenna, expands the determination of fundamental bounds to antennas with complex geometries. The method applies the Vandenbosch expressions, (3.7)–(3.10), to represent the stored energies, radiation power, and other quantities in terms of antenna currents, making it flexible for application for different optimization problems, see Section 4.1.

Here the primary optimization problem to determine the G/Q bounds is presented. For a comprehensive introduction to different antenna optimization problems see [66]. The G/Q quotient for a lossless antenna can be expressed using the partial gain (3.12) and Q-factor (3.1) expressions as [63, 66]

$$\frac{G(\hat{\boldsymbol{r}},\hat{\boldsymbol{e}})}{Q} = \frac{2\pi P(\hat{\boldsymbol{r}},\hat{\boldsymbol{e}})}{\omega \max\{W_{\mathrm{e}}, W_{\mathrm{m}}\}} \tag{3.20}$$

which can be written as the optimization problem to determine the fundamental bounds on the structure [63, 66]

$$\begin{aligned} &\text{minimize} && \max\{W_{\mathrm{e}}, W_{\mathrm{m}}\} \\ &\text{subject to} && P(\hat{\boldsymbol{r}},\hat{\boldsymbol{e}}) = P_{\mathrm{r}0} \end{aligned} \tag{3.21}$$

where the $P_{\mathrm{r}0}$ is a fixed partial radiation intensity. The computation of (3.21) for arbitrarily shaped antennas is presented in Section 4.1 using the expressions derived in Section 3.2.

4 Advanced Computational Tools

4.1 Antenna Current Optimization

Antennas are used in numerous applications, and each has its unique parameter or parameters of interest [7, 98, 146]. Antenna design is the process of developing an antenna complying with the specifications of the application. This process usually results in a trade-off between different parameters. One example common in wireless terminal design is the balance of bandwidth and directivity to the antenna's dimensions [65, 130, 142, 146, 155]. Another example is balancing the beamwidth and sidelobe levels in antenna arrays [100, 103, 150]. Usually, these design requirements can be expressed as an optimization problem. If the optimization problem is rewritten in terms of the antenna's current, it is called antenna current optimization [63, 66, 70]. This technique has been applied successfully to investigate the limitations on the G/Q quotient of different antennas in [63, 66, 67, 70], minimization of Q-factor in [18, 86], trade-off between efficiency and Q-factor in [58, 138], super-directivity in [63, 66, 92], embedded antennas in [26, 27, 63, 66], multiple-input multiple-output (MIMO) capacity in [37], and antenna arrays in [91].

The optimization problem is defined with the parameters of interest, some examples on antenna optimization problems are given in Section 3.3. The problem is then formulated in terms of the antenna currents. Once the optimization problem is solved, an optimal arrangement of surface currents is found on the antenna geometry. This technique can be used to obtain customized performance bounds of the structure under investigation. One example is the optimization of antenna bandwidth for different polarizations or radiation patterns [63, 66, 137]. The problem can be extended to embedded antennas by restricting the optimization to a specific region on the structure. This is common for mobile wireless terminals as certain parts of the terminal cannot be modified, for example, the screen, the battery, and the printed circuit board.

Using the matrices obtained in Section 3, fundamental bounds for the partial gain to Q-factor quotient in (3.20) are expressed as the optimization problem (3.21) using the matrices [66]

$$\begin{aligned} &\text{minimize} && \max\{\mathbf{I}^{\mathrm{H}}\mathbf{X}_{\mathrm{e}}\mathbf{I}, \mathbf{I}^{\mathrm{H}}\mathbf{X}_{\mathrm{m}}\mathbf{I}\} \\ &\text{subject to} && |\mathbf{F}\mathbf{I}|^2 = 1, \end{aligned} \tag{4.1}$$

where the partial radiation intensity is proportional to $|\hat{\boldsymbol{e}}^* \cdot \boldsymbol{F}(\hat{\boldsymbol{r}})|^2 \approx |\mathbf{F}\mathbf{I}|^2$ [66], and the scale invariance of G/Q with respect to the current vector $\mathbf{I}$ is used. The formulation can further be modified allowing the equality constraint $|\mathbf{FI}|^2 = 1$ to be expressed as $\mathbf{FI} = -\mathrm{j}$ [63, 66]. Hence, (4.1) can be rewritten as a convex optimization problem

$$\begin{aligned} &\text{minimize} && \max\{\mathbf{I}^{\mathrm{H}}\mathbf{X}_{\mathrm{e}}\mathbf{I}, \mathbf{I}^{\mathrm{H}}\mathbf{X}_{\mathrm{m}}\mathbf{I}\} \\ &\text{subject to} && \mathbf{FI} = -\mathrm{j}. \end{aligned} \tag{4.2}$$

The solution gives an optimal current that achieves the lowest Q-factor. The optimization problem (4.2) can alternatively be expressed as

$$\begin{aligned} &\text{maximize} && \mathbf{FI} = -\mathrm{j} \\ &\text{subject to} && \mathbf{I}^{\mathrm{H}}\mathbf{X}_{\mathrm{e}}\mathbf{I} \leq 1 \\ & && \mathbf{I}^{\mathrm{H}}\mathbf{X}_{\mathrm{m}}\mathbf{I} \leq 1. \end{aligned} \tag{4.3}$$

It is also possible to investigate the effect of antenna ohmic losses on the optimal currents. The ohmic losses can be computed with the MoM basis functions and the sheet resistance R_{s}, that was introduced in Section 3.1, as [58]

$$P_{\Omega} \approx \frac{1}{2}\mathbf{I}^{\mathrm{H}}\mathbf{R}_{\Omega}\mathbf{I} = \frac{R_{\mathrm{s}}}{2}\mathbf{I}^{\mathrm{H}}\boldsymbol{\Psi}\mathbf{I}, \tag{4.4}$$

where the elements of matrix $\boldsymbol{\Psi}$ are

$$\Psi_{mn} = \int_{S} \boldsymbol{\psi}_m(\boldsymbol{r}) \cdot \boldsymbol{\psi}_n(\boldsymbol{r}) \mathrm{dS}. \tag{4.5}$$

As (4.2) is a convex problem and $\mathbf{R}_{\Omega}$, the ohmic loss matrix in (4.4), is a positive semidefinite matrix; their linear combination with coefficients $a_n \geq 0$, $n = 1, 2$ is also convex

$$\begin{aligned} &\text{minimize} && a_1 \max_{\mathbf{I}}\{\mathbf{I}^{\mathrm{H}}\mathbf{X}_{\mathrm{e}}\mathbf{I}, \mathbf{I}^{\mathrm{H}}\mathbf{X}_{\mathrm{m}}\mathbf{I}\} + a_2\mathbf{I}^{\mathrm{H}}\mathbf{R}_{\Omega}\mathbf{I} \\ &\text{subject to} && \mathbf{FI} = -\mathrm{j}. \end{aligned} \tag{4.6}$$

The optimization problem (4.6) is called a Pareto optimality problem [14, 138] and its solution is a trade-off between the lowest achievable Q-factor and highest efficiency. Convex optimization problems (4.2), (4.3), and (4.6) can be solved with convex optimization libraries, notably with MATLAB's CVX [55].

Two applications of antenna current optimization are investigated in this thesis: the bounds for antennas above a ground plane in Paper I; the use of bounds in antenna synthesis and placement for wireless terminals in Paper II.

4.2 Characteristic Modes

Eigenfunctions are an essential tool to solve problems in electromagnetic theory [29, 80, 112, 113, 135]. In coordinate systems where the Helmholtz equation is separable, eigenfunctions can be applied to solve differential equations. One example is the spherical vector waves, see Section 2.5, that is the solution to the vector wave Helmholtz equation [75, 99, 113]. Characteristic modes are closely related to the eigenfunction method from classical electromagnetic theory. Garbacz theorized CMs in 1965 in his work [46], in order to solve electromagnetic problems in the resonance region, that is between the Rayleigh- and high-frequency regions. The mathematical foundation was laid later with the works of Harrington and Mautz in [80]. The computational framework to extend CMs to arbitrary conducting geometries using the MoM was presented in [79].

CMs has gained popularity in recent years as a tool providing new insight into electromagnetic problems. The CMs are the natural current modes of the geometry with orthogonal far-fields [79, 80], independent of excitation, or feed [15]. Therefore, CMs are only dependent on the geometric and material properties of the antenna. Moreover, CMs describe radiation properties of the geometry such as resonances and radiated far-fields. Wireless terminal antenna design has benefited from CM analysis, as a limited number of modes are sufficient to model a structure's radiation properties [15, 46, 79]. Knowledge that is gained using CM analysis can benefit in analysis, design, and even synthesis of antennas [15]. For this reason CM analysis has been applied to antenna design [12, 39, 101, 111], antenna shape and feed synthesis [16, 41, 45, 102, 157], and prediction of optimal currents [16, 66, 86].

In this section, CM theory is presented in the framework provided in [79]. The CMs for arbitrary conducting geometries are obtained from the generalized eigenvalue problem (GEP)

$$\mathbf{X}\mathbf{I}_p = \lambda_p \mathbf{R}\mathbf{I}_p, \tag{4.7}$$

where $\mathbf{R}$ and $\mathbf{X}$ are the resistance and reactance matrices in (2.34), λ_p and $\mathbf{I}_p$ are the p^{th} eigenvalue and eigenvector, respectively. These two quantities are also called the characteristic eigenvalues and characteristic currents. In (4.7), $\mathbf{R}$ is the weighting matrix, which results in orthogonal radiation patterns for the eigenvectors. The orthogonality relations of the characteristic currents are

$$\mathbf{I}_p^{\mathrm{H}}\mathbf{R}\mathbf{I}_q = \delta_{pq}, \tag{4.8}$$

$$\mathbf{I}_p^{\mathrm{H}}\mathbf{X}\mathbf{I}_q = \lambda_p\delta_{pq}, \tag{4.9}$$

$$\mathbf{I}_p^{\mathrm{H}}\mathbf{Z}\mathbf{I}_q = \left(1 + \mathrm{j}\lambda_p\right)\delta_{pq}, \tag{4.10}$$

where p, q are the mode indices, and δ_{pq} is the Kronecker delta function [6]. The magnitude of the eigenvalue λ_n is related to the radiation efficiency of the mode [15], where modes with smaller eigenvalues radiate better. Moreover, the sign of the eigenvalue indicates if the mode is inductive $\lambda_p > 0$, capacitive $\lambda_p < 0$, or resonant $\lambda_p = 0$. This can also be inferred from the Rayleigh quotient

$$\lambda_p = \frac{\mathbf{I}_p^{\mathrm{H}}\mathbf{X}\mathbf{I}_p}{\mathbf{I}_p^{\mathrm{H}}\mathbf{R}\mathbf{I}_p} = \frac{2\omega\left(W_{\mathrm{m}}^p - W_{\mathrm{e}}^p\right)}{P_{\mathrm{r}}^p}. \tag{4.11}$$

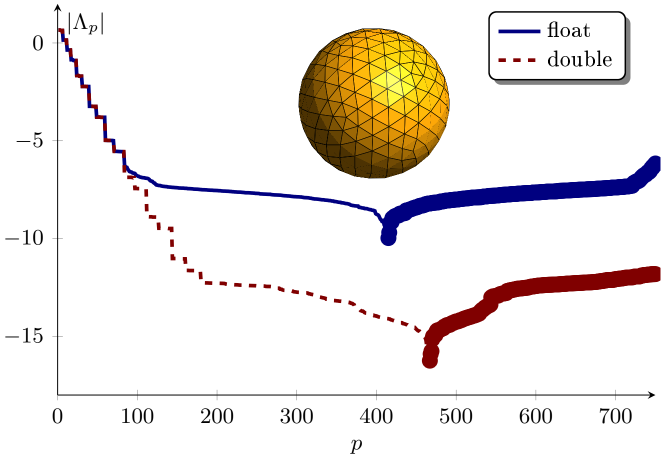

Figure 6: Eigenvalues Λ_p of the resistance matrix $\mathbf{R}$ computed with float and double precision for a sphere of electrical size $ka = 1.5$ and $N = 750$ DOF. Negative eigenvalues are denoted by the thick lines.

The total radiated power for mode p is $P_{\mathrm{r}}^{p} = 1$, while the stored electric and magnetic energies are W_{e}^{p} and W_{m}^{p}, respectively.

Eigenvalues of the GEP (4.7) depend on the properties of the matrices $\mathbf{R}$ and $\mathbf{X}$; where $\mathbf{R}$ is positive semi-definite, and $\mathbf{X}$ is symmetric indefinite. But, the matrix $\mathbf{R}$ is ill-conditioned when computed with finite precision arithmetic [17, 66, 136], see Appendix B. The precision of computations determine the numerical noise of the eigenvalues that is at minimum the unit round-off. The round-off value is approximately 10^{-7} for float and 10^{-16} for double precision [52]. Matrix computations involve numerous floating point operations, leading to higher numerical noise levels than the unit round-off.

The eigenvalues of the matrix $\mathbf{R}$ computed with float and double precision for a sphere of size $ka = 1.5$ is displayed in Fig. 6. As expected, using double precision results in more eigenvalues; a direct consequence of the unit round-off level being lower for double precision than for float precision. The accuracy of computation has a negligible impact on the spectrum of the matrix $\mathbf{X}$.

The computation of characteristic modes is influenced by the indefiniteness of the finite precision matrix $\mathbf{R}$, where most of the calculated $\mathbf{R}$ eigenvalues are numerical noise. As a result, the CMs obtained using (4.7) will also contain numerical noise. Therefore, only a limited number of modes are correctly computed. This limit can be circumvented where the conventional method is modified by replacing $\mathbf{R}$ with the factorization (2.38), see Paper III.

4.3 Macro Basis Functions

The MoM solution of the EFIE presented in Section 2.7 results in a linear system of equations with N degrees-of-freedom (DOF). As the DOF in a problem increase, the number of elements in the impedance matrix scale in the order of N^2. This quadratic growth can quickly exceed available memory limits. Moreover, the number of matrix operations in the direct solution of the system of equations in (2.30) increases in computational complexity of $\mathcal{O}(N^3)$. The macro basis function (MBF) method reduces the DOF of radiation and scattering problems [34, 106]. The MBF and similar techniques such as characteristic basis function (CBF) [104, 105, 123], synthetic function (SF) [108] can be grouped as aggregated basis function methods. While the concepts of the three techniques are close, the generation of the aggregated basis functions diverge.

The MBF method has additionally been applied to problems including planar antennas and microwave circuits [44], and regular and irregular antenna arrays [53]. To accelerate the computation of distant interactions between elements, the MBF method has been combined with the fast multipole method (FMM) [33, 47], adaptive cross approximation (ACA) [106], and adaptive integral method (AIM) [145] algorithms.

In the MBF method, the structure is first divided into smaller sub-domains [34]. A subset of induced currents on the sub-domain will characterize the MBFs. The subset is chosen to represent current distributions that can be excited on the sub-domain. For example, in an antenna array, distant sources can induce currents on the sub-domains, this can be modeled as impinging incident plane waves, also called a plane-wave spectrum [34]. Additionally, nearby elements can also influence the current distributions; these elements can be replaced by equivalent point sources. For sub-domains containing RF ports, the currents distribution generated by the port should also be included.

Considering only a single sub-domain with N DOF, the excitations which generate the induced currents described in the paragraph above are grouped into an excitation matrix

$$\mathbf{V}_{\mathrm{s}} = \left[\mathbf{v}_1,\, \mathbf{v}_2, \cdots, \mathbf{v}_{N_{\mathrm{e}}}\right], \tag{4.12}$$

where N_{e} is the total number of excitations, $\mathbf{V}_{\mathrm{s}} \in \mathbb{C}^{N \times N_{\mathrm{e}}}$, and $\mathbf{v}_i$ is the column vector for the i^{th} excitation. Assuming the sub-domain impedance matrix is denoted $\mathbf{Z}_{\mathrm{sub}}$ in the following, the response currents $\mathbf{I}_{\mathrm{s}}$ to the excitation matrix $\mathbf{V}_{\mathrm{s}}$ are calculated using (2.30),

$$\mathbf{I}_{\mathrm{s}} = \mathbf{Z}_{\mathrm{sub}}^{-1} \mathbf{V}_{\mathrm{s}}. \tag{4.13}$$

The next step is to generate an orthogonal basis from the collection of induced currents in (4.13) [34]. A singular value decomposition (SVD) is used to generate an orthogonal basis

$$\mathbf{I}_{\mathrm{s}} = \mathbf{U} \boldsymbol{\Sigma} \mathbf{V}^{\mathrm{H}}, \tag{4.14}$$

where $\mathbf{U}$ and $\mathbf{V}$ are unitary matrices containing the singular vectors and $\boldsymbol{\Sigma}$ is a diagonal matrix of the singular values σ. The MBFs, chosen as the singular vectors in $\mathbf{U}$, can be truncated if the normalized singular values are less then a specific tolerance τ, giving a truncated basis $\widehat{\mathbf{U}} \in \mathbb{C}^{N\times M}$ with $M \ll N$ DOF, which is the first M columns of the matrix $\mathbf{U}$. The linear equation system for the impedance matrix (2.30), can be compressed with a change of basis

$$\widehat{\mathbf{U}}^{\mathrm{H}}\mathbf{Z}_{\mathrm{sub}}\widehat{\mathbf{U}}\widehat{\mathbf{U}}^{\mathrm{H}}\mathbf{I} = \widehat{\mathbf{U}}^{\mathrm{H}}\mathbf{V} \tag{4.15}$$

resulting in the compressed system of equations

$$\mathbf{Z}^{\mathrm{mbf}}\mathbf{I}^{\mathrm{mbf}} = \mathbf{V}^{\mathrm{mbf}}, \tag{4.16}$$

where the compressed impedance matrix $\mathbf{Z}^{\mathrm{mbf}} \in \mathbb{C}^{M\times M}$ is

$$\mathbf{Z}^{\mathrm{mbf}} = \widehat{\mathbf{U}}^{\mathrm{H}}\mathbf{Z}_{\mathrm{sub}}\widehat{\mathbf{U}} \tag{4.17}$$

and the compressed current and excitation vectors are

$$\mathbf{I}^{\mathrm{mbf}} = \widehat{\mathbf{U}}^{\mathrm{H}}\mathbf{I}, \tag{4.18}$$

$$\mathbf{V}^{\mathrm{mbf}} = \widehat{\mathbf{U}}^{\mathrm{H}}\mathbf{V}. \tag{4.19}$$

Once (4.17) is solved the currents in RWG basis are obtained using $\mathbf{I}^{\mathrm{rwg}} = \widehat{\mathbf{U}}\mathbf{I}^{\mathrm{mbf}}$.

The MBF method described above can also be applied to problems consisting of multiple sub-domains [34]. For simplicity, assuming that sub-domains do not intersect and DOF numbering is contiguous, a set of MBFs are then generated for each sub-domain separately. The compressed impedance matrix for the problem can be written in block form as

$$\mathbf{Z}^{\mathrm{mbf}} = \begin{bmatrix} \widehat{\mathbf{U}}_1^{\mathrm{H}}\mathbf{Z}_{1,1}\widehat{\mathbf{U}}_1 & \widehat{\mathbf{U}}_1^{\mathrm{H}}\mathbf{Z}_{1,2}\widehat{\mathbf{U}}_2 & \cdots & \widehat{\mathbf{U}}_1^{\mathrm{H}}\mathbf{Z}_{1,N_{\mathrm{t}}}\widehat{\mathbf{U}}_{N_{\mathrm{t}}} \\ \widehat{\mathbf{U}}_2^{\mathrm{H}}\mathbf{Z}_{2,1}\widehat{\mathbf{U}}_1 & \widehat{\mathbf{U}}_2^{\mathrm{H}}\mathbf{Z}_{2,2}\widehat{\mathbf{U}}_2 & \cdots & \widehat{\mathbf{U}}_2^{\mathrm{H}}\mathbf{Z}_{2,N_{\mathrm{t}}}\widehat{\mathbf{U}}_{N_{\mathrm{t}}} \\ \vdots & \vdots & \ddots & \vdots \\ \widehat{\mathbf{U}}_{N_{\mathrm{t}}}^{\mathrm{H}}\mathbf{Z}_{N_{\mathrm{t}},1}\widehat{\mathbf{U}}_1 & \widehat{\mathbf{U}}_{N_{\mathrm{t}}}^{\mathrm{H}}\mathbf{Z}_{N_{\mathrm{t}},2}\widehat{\mathbf{U}}_2 & \cdots & \widehat{\mathbf{U}}_{N_{\mathrm{t}}}^{\mathrm{H}}\mathbf{Z}_{N_{\mathrm{t}},N_{\mathrm{t}}}\widehat{\mathbf{U}}_{N_{\mathrm{t}}} \end{bmatrix}, \tag{4.20}$$

where $\widehat{\mathbf{U}}_i$ is the truncated MBF for sub-block i, $\mathbf{Z}_{i,j}$ is the impedance matrix between block i and j, and N_{t} denotes the total number of sub-blocks. One possible limitation of the MBF method is the SVD, which is applied to generate the MBFs on each sub-domain. If the number of DOF is high, the SVD that has a computational complexity of $\mathcal{O}(N^3)$ becomes a bottleneck in the simulation. Therefore, the MBF method is best suited for problems that have reasonably sized sub-domains.

Another issue is the number of off-diagonal impedance matrices that have to be calculated, as it quadratically increases with the number of sub-domains. These are interactions, coupling matrices between sub-domains, that can be efficiently computed with acceleration methods [33, 34, 47, 106, 145]. One such method is the ACA [9, 83, 106, 158] and it is a purely algebraic acceleration method that operates only on the MoM matrices. It is simpler to implement than

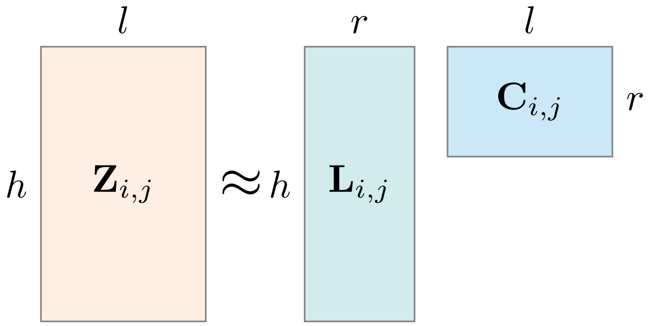

Figure 7: Approximating the coupling matrix $\mathbf{Z}_{i,j}$ between block i and j using the adaptive cross approximation (ACA).

the FMM [22, 23, 28, 57], and can be applied to different integral equation kernels making it modular for software tool development [158]. The ACA approximates the coupling matrix between sub-domains i and j by a matrix product of two lower rank matrices [158] as

$$\mathbf{Z}_{i,j} = \mathbf{L}_{i,j}\mathbf{C}_{i,j}, \tag{4.21}$$

where $\mathbf{L}_{i,j} \in \mathbb{C}^{h\times r}$, $\mathbf{C}_{i,j} \in \mathbb{C}^{r\times l}$, as depicted in Fig. 7. The $\mathbf{L}_{i,j}$ and $\mathbf{C}_{i,j}$ matrices are constructed on-the-fly, without the need of computing the whole coupling matrix.

If the array has translational symmetries, it is possible to reuse the computed matrices to assemble the full impedance matrix. The use of translational symmetries for a 2D linear array is presented below.

The MBF with ACA acceleration methods is used in Paper IV to synthesize large endfire array antennas for phased array applications. In Paper V two different methods to generate MBFs for connected geometries are compared.

To illustrate the utilization of translational symmetries a 2D linear antenna array with disconnected antenna elements is used. This topology is identical to the one used in Paper IV. The antenna array is situated on the xy-plane, the number of elements in the x and y axes are N_x and N_y. Therefore the total number of antenna elements is $N_\mathrm{t} = N_\mathrm{x}N_\mathrm{y}$. Assuming that the DOF for each block is contiguous, the full impedance matrix can be written in block matrix form as

$$\mathbf{Z} = \begin{bmatrix} \mathbf{Z}_{1,1} & \mathbf{Z}_{1,2} & \cdots & \mathbf{Z}_{1,N_\mathrm{t}} \\ \mathbf{Z}_{2,1} & \mathbf{Z}_{2,2} & \cdots & \mathbf{Z}_{2,N_\mathrm{t}} \\ \vdots & \vdots & \ddots & \vdots \\ \mathbf{Z}_{N_\mathrm{t},1} & \mathbf{Z}_{N_\mathrm{t},2} & \cdots & \mathbf{Z}_{N_\mathrm{t},N_\mathrm{t}} \end{bmatrix} \tag{4.22}$$

here $\mathbf{Z}_{i,j}$ is the coupling matrix between antenna i and j. As the full impedance matrix is transpose symmetric, we have $\mathbf{Z}_{i,j} = \mathbf{Z}_{j,i}^\mathrm{T}$. To obtain a transpose symmetric compressed matrix, the Hermitian transpose in (4.15) is replaced by a transpose [34]. Translational symmetries can be used to reduce the total number of blocks to be computed in (4.22).

Considering the simplest case of an array with identical elements, the diagonal block matrices are identical, $\mathbf{Z}_{1,1} = \mathbf{Z}_{i,i}$ with $i = 2, \cdots, N_{\mathrm{t}}$. Additionally, the block matrices for $i \neq j$ that are separated with an identical translation vector can be reused when assembling the total matrix. Consequently, the coupling matrix for a translational vector needs to be computed only once. Using the translational symmetries the number of blocks that need to be calculated is $N_{\mathrm{block}} = N_{\mathrm{t}} + (N_{\mathrm{x}} - 1)(N_{\mathrm{y}} - 1)$. For a $N_{\mathrm{x}} = 200$ by $N_{\mathrm{y}} = 100$ element array only 4×10^4 block matrices need to be computed from the total of 4×10^8, which is 0.01% of the total blocks, yielding in significant reduction in assembly time for the full impedance matrix.

5 Research Contribution

This section presents the summary of the results of the five papers included in this thesis.

5.1 Article 1 Results

In this letter, the fundamental limitation on antennas above an infinite PEC ground plane is presented. As far as the authors are aware this paper is the first to give strict bounds for this topology. Antennas above a ground plane are commonly found in wireless devices [146]. The proximity of the ground plane, for example the chassis of a mobile phone, to the antenna can either augment or impede the antenna's performance substantially [7, 130, 146]. One extreme case is when the antenna is very close to the ground plane, this will effectively short circuit the antenna, resulting in a loss of performance. On the other hand, the ground plane can be used to improve the performance of the antenna [7,130,146]. Fundamental limitations offer apriori knowledge and insight on how the antenna will be affected and are useful FOM for the antenna designer [66, 70].

Limitations on a reference rectangular patch's geometry were investigated for different combinations of patch heights, and polarizations. The bounds were determined for the rectangular patch using antenna current optimization. As expected the patch antenna's G/Q bound, and bandwidth deteriorates as the distance shortens between the ground plane and antenna. As the rectangular patch is a basic structure, additional patches with complicated geometries such as a slot loaded patch, H-shaped patch were designed. The dimension of the slot and H-shaped patches were restricted to the reference rectangular patch antenna. All of the patch antennas were then simulated with the commercial software tool FEKO [3], and their Q-factors were obtained from the derivative of the input impedance. Results show that all of the patches are bounded in G/Q by the reference patch.

5.2 Article 2 Results

In this book chapter, the use of fundamental bounds for antenna design and optimization are presented. Additionally, the problem of antenna placement on a wireless terminal is also investigated with the use of physical bounds. The major performance challenges of antennas in wireless terminals can be grouped into three broad categories; coupling to nearby components, restricted area to design the antenna, and placement of the antenna itself [7, 146, 153].

A simplified wireless terminal chassis is used in the simulations. For the antenna design and optimization, genetic algorithm (GA) and fundamentals bounds are used in a simulation framework. In the first example, an embedded antenna in a wireless terminal is designed and optimized for a single frequency. Optimal antenna performance is determined for different design areas, using the fundamental bounds. Given the design area restrictions, optimal performance of the designed antenna is always lower compared to the antenna design that utilizes the entire chassis. GA is then used to synthesize structures in the allocated design area. In each iteration, fundamental bounds are used to select the best candidates. Simulation framework was run separately for five frequencies over different design areas. All of the generated antennas were close to the optimal performance predicted by the bounds. The results were verified with the commercial software ESI-CEM [40].

The same simulation framework is used to design an embedded antenna optimized for two frequencies simultaneously. In this case, both bands were given equal fractional bandwidths of 15.8 %. Different cost functions are tried where the emphasis is either put on the optimum Q-factor obtained from the fundamental bounds, or from the Q-factor obtained from the input impedance, or a combination of both. Synthesized antennas are then matched to 50 Ω with a matching network designed using the commercial software BetaMatch [11]. Results show that all the matched antennas have less than $-6\,\mathrm{dB}$ s_{11} magnitude in the entire band.

The last example demonstrated the use of fundamental bounds in antenna placement. Nine different locations are selected on the chassis based on observation of common wireless terminals. Results show that antenna current optimization can be utilized to determine an optimal location.

5.3 Article 3 Results

This transaction presents a new technique to compute characteristic mode (CM) decomposition. The proposed method provides an improvement in the number of obtainable modes, their numerical accuracy, and also in computation efficiency. Numerical problems in the computation of high order modes are caused by the rounding errors and limited precision when calculating the MoM resistance matrix $\mathbf{R}$ [17], see Section 4.2. Consequently, the matrix $\mathbf{R}$ computed with finite precision arithmetic is low rank.

Radiation modes, derived from the matrix **R** are one of the simplest modal decompositions [127]. Eigenvalues of the matrix **R** decay rapidly, therefore, only a limited number of them can be determined before reaching the numerical noise floor. This computation is closely dependent on the numerical precision used in the computation of the matrix **R**, and the linear algebra routines used for the decomposition [52]. Considering the CM decomposition, the ill-conditioned matrix **R** is used as a weighting matrix, limiting the number of obtainable eigenvalues.

In the proposed method the matrix **R** is written as a matrix product of the matrix **S**. Due to the evaluation of **S**, numerical dynamics of matrix **R** is preserved. Additionally, as **S** is a decomposition of **R**, (2.38), it can be used for model order reduction (MOR), increasing the computation efficiency of both **R** and different modal decompositions. Several examples are constructed using two simple geometries, a sphere, and a rectangle plate. Results are then compared with the conventional method, simulations from different commercial software, and in the case of a sphere the analytical solutions. The results show that the numerical dynamics are doubled, and the number of obtainable modes is significantly increased.

5.4 Article 4 Results

In this transaction, a simulation framework used in the analysis of large endfire antenna arrays is presented. Strong coupling between antenna elements in endfire operation influences the matching of the whole antenna array. Endfire radiation also strains the RF circuits of edge elements, as they receive most of the transmitted power.

From a computational perspective, all of the factors listed above restrict the applicability of a standard large array analysis method, periodic boundary conditions. Another widely used method is the FMM [22, 23, 28, 57], that can be applied to the phased array problem to decrease the required memory significantly and accelerate the computation. But, when determining the embedded element patterns, the FMM would need to solve the whole problem for all excitations, resulting in a computational bottleneck.

An in-house computation software using both the MBF [34, 104–106, 108, 123] and ACA [9, 83, 106, 158] is implemented. The MBF is used to compress the computed MoM matrices while the ACA is used as an acceleration method. Furthermore, the number of coupling matrices are reduced by taking into account array symmetries. Convex optimization is later applied to synthesize an endfire pattern using embedded element patterns (EEPs).

This simulation framework is then applied to analyze a large array with dimensions 200×12 and of size $100\lambda \times 6\lambda$. The array consists of identical bowtie elements with 643 RWGs/element. Solving this large array directly with a MoM solver would result in 1.5×10^6 DOF requiring approximately 72 TB of memory only for the impedance matrix. Such a system cannot be directly processed by linear algebra solvers as the complexity scales as $\mathcal{O}(N^3)$. However, applying the compression, acceleration, and utilizing the symmetries the problem size is drastically reduced. 2400 EEPs are computed for a single frequency between 8 min 30 s and 27 min 20 s, where the difference is due to dependence of compression ratio to the frequency.

Once the simulations are complete, as a post-processing step, to enhance the matching, endfire pattern synthesis is performed using convex optimization. Different characteristic impedances are tested to find the optimal total active reflection coefficient (TARC) [107], that is a metric for multi-port systems. The optimization is applied with two separate methods. In the first method, discrete frequency points that the array operates, are optimized. In the second, the phase variation of the array is restricted with respect to the resonance frequency of the array. Results show that a wide bandwidth with a fractional bandwidth of approximately 53 % is obtained for endfire operation. Different array configurations with elements of 50 × 12, 100 × 12 were also investigated, and a similar performance in fractional bandwidth and endfire radiation was obtained.

5.5 Article 5 Results

This letter presents the comparison of two techniques used in interconnected array analysis with the MBF method [106, 108]. The endfire operation mode of phased arrays is an interesting case, due to the strong mutual coupling between elements. The two techniques, denoted as method A [108] and method B [106], are investigated under the endfire operation mode to determine their accuracies. In method A the DOF connecting sub-domains are composed of Half-RWGs that are independent of the MBFs. In method B adjacent sub-domains are included in the compression by using a trapezoidal windowing function [104].

Two linear arrays of 10 antennas, one composed of monopoles and the other of bowties is used to compare the methods. These arrays are tested in both broadside and endfire radiation modes. Our findings showed that the first method, method A, required more DOF to represent the currents for a specific threshold accurately. This was due to the different singular value sequences for the two methods. Both methods had their unique advantages and provided accurate solutions, although they have a higher error in endfire operation mode.

6 Conclusions

With the fast progression of new technologies and applications in the fields ranging from wireless communications to sensor systems, there is a continuous need to improve and extend the capabilities of available computational electromagnetic tools. The outcome of such efforts may increase the accuracy, or the computational efficiency of existing algorithms, or lead to the development of new modeling, simulation, analysis and design arsenal. The goal of this work has been to investigate computational tools for antenna analysis and design.

In compliance with this goal, Paper I uses antenna current optimization to determine the bounds for antennas above an infinite ground plane. This bound is a FOM for antenna designers and can aid the designer in several aspects. First, it is possible to have apriori knowledge on the limitations of the geometry allocated for the antenna, and whether or not it meets the specifications. Second, it is possible to compare antenna performance and its proximity to the bounds; this knowledge can aid the designer to decide if the antenna under design should be improved.

The second paper, Paper II, investigates the use of fundamental bounds along with a MoM and GA hybrid solver to design antennas that reach theoretical limitations. This framework is an inception of a tool that can automate both the antenna design and its placement.

Another tool, characteristic mode (CM) analysis has been improved in Paper III, by increasing not only its accuracy but also its computation efficiency. The proposed technique can also be used to compute high order modes that were not possible to determine with the conventional method and continuous far-field patterns with high efficiency. Moreover, the technique can also be easily be added to existing MoM solvers as an independent module.

Efficient synthesis of endfire patterns for large arrays has been achieved with a MoM solver using the MBFs and ACA in Paper IV. Convex optimization is used to determine the excitation coefficients to improve the impedance matching under endfire operation. It was found that the impedance matching was significantly improved over the traditional Hansen-Woodyard excitation. In Paper V two techniques used in MBF method to model interconnected domains are investigated and benchmarked. Both methods gave accurate results under endfire excitation.

7 Future Work

There are several areas of interest in which the work presented in this dissertation may be extended. The following is a short overview of leads that may provide significant contribution to the area covered by this work.

For the fundamental bounds, investigation of antennas consisting of dielectric, lossy materials is a possible next step. Other interesting options include trade-offs between various parameters, such as Q-factor, impedance matching, radiation efficiency, MIMO channel capacity, etc. These findings will provide further insight into theoretical limitations and can aid antenna designers.

The method proposed in Paper III, that is used to enhance the characteristic modes analysis, can be applied to different modal decompositions to increase the computation efficiency and accuracy. Two modal decompositions that might be of interest are the efficiency and stored energy modes.

As for the endfire array synthesis tools, a detailed theoretical analysis of different parameters, such as the association between the array arrangement and excitations, or determining optimal characteristic impedances for matching may lead to significant improvements. Moreover, the analysis can be extended to include arrays with interconnected subdomains.

Appendix A Integration over Triangles

In computational electromagnetics the model under investigation is divided into smaller elements that are solvable with differential or integral methods, this process is called *meshing* [21, 147]. The unit element of the mesh can be a line, a surface such as a triangle, quadrilateral, or higher order geometries [21, 35]. One of the widely used mesh element is the triangle that patches complex surfaces. Our in-house MoM solver that was developed as part of this work uses triangle mesh elements. Here simplex (barycentric) coordinates are used to represent the triangle. The vector $\boldsymbol{r}$ is written as [49]

$$\boldsymbol{r} = \alpha \boldsymbol{r}_1 + \beta \boldsymbol{r}_2 + \gamma \boldsymbol{r}_3 \tag{A.1}$$

in simplex coordinates, where $\boldsymbol{r}_i$, $i = \{1, 2, 3\}$, are the three vertices of the triangles and

$$\begin{aligned} \alpha &= \frac{A_1}{A}, \\ \beta &= \frac{A_2}{A}, \\ \gamma &= \frac{A_3}{A}, \end{aligned}$$

where A is the area of the triangle; A_i, $i = \{1, 2, 3\}$, are the sub-triangle areas. The sum of barycentric coordinates is $\alpha + \beta + \gamma = 1$, Fig. 8.

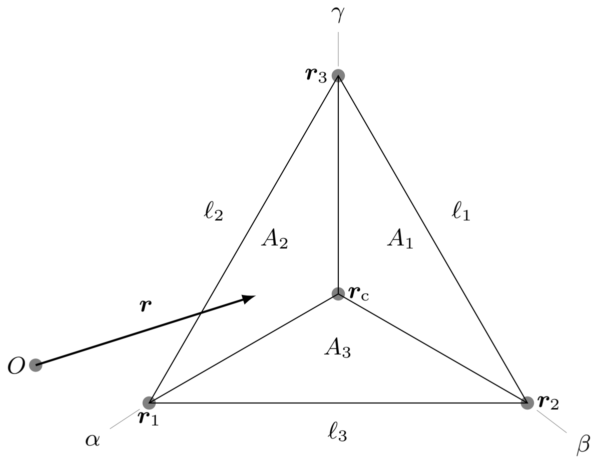

Figure 8: Simplex coordinates α, β, γ defined on an equilateral triangle with vertices $\boldsymbol{r}_i$, edge lengths ℓ_i, sub-triangle areas A_i where $i = \{1, 2, 3\}$, and $\boldsymbol{r}_\mathrm{c}$ is the barycenter.

Surface integral over the triangle is then written by a change of variables giving

$$\begin{aligned}\iint_S f(\boldsymbol{r})\mathrm{dS} &= \iint_S f(\alpha,\beta)\left|J(\alpha,\beta)\right|\mathrm{d}\alpha\mathrm{d}\beta \\ &= 2A\int_{\alpha=0}^{1}\int_{\beta=0}^{1-\alpha} f(\alpha,\beta)\,\mathrm{d}\alpha\mathrm{d}\beta \qquad \text{(A.2)}\end{aligned}$$

where $J(\alpha,\beta)$ is the Jakobian. To perform numerical integration over the triangle symmetrical Gaussian quadrature can be used [36, 49]

$$\iint_S f(\boldsymbol{r})\mathrm{dS} \approx A\sum_{i}^{N} w_i f(\alpha_i,\beta_i,\gamma_i) \qquad \text{(A.3)}$$

where w_i are the Gaussian quadrature weights and $\boldsymbol{r}_i = \alpha_i\boldsymbol{r}_1 + \beta_i\boldsymbol{r}_2 + \gamma_i\boldsymbol{r}_3$ are the quadrature points [36].

Appendix B Finite Precision Arithmetic

Computers use floating point representation to store real numbers and floating point arithmetic to process them. This is due to the limited number of bits used by the hardware to represent real numbers [51, 52]. Real numbers are rounded when they are converted to a floating point number. The number of bits that are used to represent real numbers depends on the hardware; standard values are 32- or 64-bits in modern systems. The IEEE-754 standard [159] defines 32-bit single precision as *float* and 64-bit double precision as *double*. Special arithmetic libraries such as *mpmath* [88] allow higher precisions *e.g.* 128-bits at the expense of increase computing time.

In simulating physical systems, it is essential to quantify the error in representing numbers as floats, and floating point arithmetic operations to understand their accuracy and limitations, for a detailed overview see [51, 52, 159]. Here we follow the convention in [52] and define the floating point representation, $\mathrm{fl}(x)$, of a real number $x \in \mathbb{R}$ as

$$\mathrm{fl}(x) = x(1+\delta) = \tilde{x}, \quad |\delta| \leq u. \tag{B.1}$$

The value u is the unit round-off, and is defined as $u = 0.5\varepsilon_{\mathrm{fp}}$, where $\varepsilon_{\mathrm{fp}}$ is the distance from 1 to the next floating point number. For the IEEE-754 standard [159] formats, the unit round-off, u, is approximately 10^{-7} for a float and 10^{-16} for a double [52]. Any operation, op, between two floating point numbers $\tilde{x}$ and $\tilde{y}$ also has an error associated and it is denoted with the unit round-off u

$$\mathrm{fl}(\tilde{x} \,\mathrm{op}\, \tilde{y}) = (\tilde{x} \,\mathrm{op}\, \tilde{y})(1+\delta), \quad |\delta| \leq u. \tag{B.2}$$

Relative error of any floating point arithmetic operation is then bounded above by the unit round-off u. Therefore, u represents the best accuracy of a floating point operation.

References

[1] J. D. Adams, B. W. Erickson, J. Grossenbacher, J. Brugger, A. Nievergelt, and G. E. Fantner. Harnessing the damping properties of materials for high-speed atomic force microscopy. *Nature Nanotechnology*, **11**, 147, November 2015.

[2] S. B. Adrian, F. P. Andriulli, and T. F. Eibert. Hierarchical bases preconditioners for the electric field integral equation on multiply connected geometries. *IEEE Trans. Antennas Propag.*, **62**(11), 5856–5861, Nov 2014.

[3] S. A. Altair Development S.A. (Pty) Ltd Stellenbosch. FEKO, Field Computations Involving Bodies of Arbitrary Shape, Suite 7.0, 2014. `https://www.feko.info/`, Retrieved: 24/11/2014.

[4] F. P. Andriulli, K. Cools, H. Bagci, F. Olyslager, A. Buffa, S. Christiansen, and E. Michielssen. A multiplicative Calderon preconditioner for the electric field integral equation. *IEEE Trans. Antennas Propag.*, **56**(8), 2398–2412, Aug 2008.

[5] F. P. Andriulli, K. Cools, I. Bogaert, and E. Michielssen. On a well-conditioned electric field integral operator for multiply connected geometries. *IEEE Trans. Antennas Propag.*, **61**(4), 2077–2087, April 2013.

[6] G. B. Arfken and H. J. Weber. *Mathematical Methods for Physicists.* Academic Press, New York, NY, sixth edition, 2005.

[7] C. A. Balanis. *Antenna Theory.* John Wiley & Sons, Hoboken, NJ, third edition, 2005.

[8] C. A. Balanis. *Advanced Engineering Electromagnetics.* John Wiley & Sons, New York, NY, 2012.

[9] M. Bebendorf. Approximation of boundary element matrices. *Numerische Mathematik*, **86**(4), 565–589, 2000.

[10] S. R. Best. Electrically small resonant planar antennas: Optimizing the quality factor and bandwidth. *IEEE Antennas Propag. Mag.*, **57**(3), 38–47, June 2015.

[11] MNW Scan, Singapore—BetaMatch, Software for antenna component matching. http://www.mnw-scan.com/.

[12] N. L. Bohannon and J. T. Bernhard. Design guidelines using characteristic mode theory for improving the bandwidth of PIFAs. *IEEE Trans. Antennas Propag.*, **63**(2), 459–465, Feb 2015.

[13] J. J. Bowman, T. B. A. Senior, and P. L. E. Uslenghi. *Electromagnetic and Acoustic Scattering by Simple Shapes.* North-Holland, Amsterdam, 1969.

[14] S. P. Boyd and L. Vandenberghe. *Convex Optimization.* Cambridge Univ. Pr., 2004.

[15] M. Cabedo-Fabres, E. Antonino-Daviu, A. Valero-Nogueira, and M. Bataller. The theory of characteristic modes revisited: A contribution to the design of antennas for modern applications. *IEEE Antennas Propag. Mag.*, **49**(5), 52–68, 2007.

[16] M. Capek, P. Hazdra, and J. Eichler. A method for the evaluation of radiation Q based on modal approach. *IEEE Trans. Antennas Propag.*, **60**(10), 4556–4567, 2012.

[17] M. Capek, V. Losenicky, L. Jelinek, and M. Gustafsson. Validating the characteristic modes solvers. *IEEE Trans. Antennas Propag.*, **65**(8), 4134–4145, 2017.

[18] M. Capek, M. Gustafsson, and K. Schab. Minimization of antenna quality factor. *IEEE Trans. Antennas Propag.*, **65**(8), 4115–4123, 2017.

[19] H.-C. Chang, Y. H. Cho, and D.-H. Kwon. Radiation Q bounds for small electric dipoles over a conducting ground plane. *IEEE Trans. Antennas Propag.*, **62**(4), 2031–2040, 2014.

[20] Y. Chen and C.-F. Wang. *Characteristic Modes: Theory and Applications in Antenna Engineering.* John Wiley & Sons, 2015.

[21] W. C. Chew, M. S. Tong, and B. Hu. *Integral Equation Methods for Electromagnetic and Elastic Waves*, volume 12. Morgan & Claypool, 2008.

[22] W. C. Chew, J.-M. Jin, C.-C. Lu, E. Michielssen, and J. M. Song. Fast solution methods in electromagnetics. *IEEE Trans. Antennas Propag.*, **45**(3), 533–543, March 1997.

[23] W. C. Chew, E. Michielssen, J. Song, and J. Jin. *Fast and Efficient Algorithms in Computational Electromagnetics.* Artech House, Inc., 2001.

[24] S. H. Christiansen and J.-C. Nédélec. A preconditioner for the electric field integral equation based on Calderon formulas. *SIAM Journal on Numerical Analysis*, **40**(3), 1100–1135, 2002.

[25] L. J. Chu. Physical limitations of omni-directional antennas. *J. Appl. Phys.*, **19**, 1163–1175, 1948.

[26] M. Cismasu and M. Gustafsson. Antenna bandwidth optimization with single frequency simulation. *IEEE Trans. Antennas Propag.*, **62**(3), 1304–1311, 2014.

[27] M. Cismasu and M. Gustafsson. Multiband antenna Q optimization using stored energy expressions. *IEEE Antennas Wireless Propag. Lett.*, **13**(2014), 646–649, 2014.

[28] R. Coifman, V. Rokhlin, and S. Wandzura. The fast multipole method for the wave equation: A pedestrian prescription. *IEEE Antennas Propag. Mag.*, **35**(3), 7–12, 1993.

[29] R. E. Collin. *Field Theory of Guided Waves.* IEEE Press, New York, NY, second edition, 1991.

[30] R. E. Collin and S. Rothschild. Evaluation of antenna Q. *IEEE Trans. Antennas Propag.*, **12**, 23–27, January 1964.

[31] D. Colton and R. Kress. *Integral Equation Methods in Scattering Theory.* John Wiley & Sons, New York, NY, 1983.

[32] K. Cools, F. P. Andriulli, and E. Michielssen. A Calderón multiplicative preconditioner for the PMCHWT integral equation. *IEEE Trans. Antennas Propag.*, **59**(12), 4579–4587, Dec 2011.

[33] C. Craeye. A fast impedance and pattern computation scheme for finite antenna arrays. *IEEE Trans. Antennas Propag.*, **54**(10), 3030–3034, Oct 2006.

[34] C. Craeye, J. Laviada, R. Maaskant, and R. Mittra. Macro basis function framework for solving maxwells equations in surface integral equation form. *The FERMAT Journal*, **3**, 1–16, 2014.

[35] D. B. Davidson. *Computational Electromagnetics for RF and Microwave Engineering.* Cambridge University Press, 2005.

[36] D. Dunavant. High degree efficient symmetrical gaussian quadrature rules for the triangle. *International journal for numerical methods in engineering*, **21**(6), 1129–1148, 1985.

[37] C. Ehrenborg and M. Gustafsson. Fundamental bounds on MIMO antennas. *IEEE Antennas Wireless Propag. Lett.*, **17**(1), 21–24, January 2018.

[38] T. F. Eibert and V. Hansen. On the calculation of potential integrals for linear source distributions on triangular domains. *IEEE Trans. Antennas Propag.*, **43**(12), 1499–1502, 1995.

[39] J. Eichler, P. Hazdra, M. Capek, T. Korinek, and P. Hamouz. Design of a dual-band orthogonally polarized L-probe-fed fractal patch antenna using modal methods. *IEEE Antennas Wireless Propag. Lett.*, **10**, 1389–1392, 2011.

[40] ESI Group, Paris, France—ESI Group's computational electromagnetic (CEM) solution. http://www.esi-group.com.

[41] J. L. T. Ethier and D. A. McNamara. Antenna shape synthesis without prior specification of the feedpoint locations. *IEEE Trans. Antennas Propag.*, **62**(10), 4919–4934, Oct 2014.

[42] L. C. Evans. *Partial Differential Equations.* American Mathematical Society, Providence, RI, 1998.

[43] R. L. Fante. Quality factor of general ideal antennas. *IEEE Trans. Antennas Propag.*, **17**(2), 151–155, March 1969.

[44] A. Freni, P. D. Vita, P. Pirinoli, L. Matekovits, and G. Vecchi. Fast-factorization acceleration of MoM compressive domain-decomposition. *IEEE Trans. Antennas Propag.*, **59**(12), 4588–4599, Dec 2011.

[45] R. Garbacz and D. Pozar. Antenna shape synthesis using characteristic modes. *IEEE Trans. Antennas Propag.*, **30**(3), 340–350, May 1982.

[46] R. Garbacz. Modal expansions for resonance scattering phenomena. *Proc. IEEE*, **53**(8), 856–864, Aug, 1965.

[47] E. Garcia, C. Delgado, I. G. Diego, and M. F. Catedra. An iterative solution for electrically large problems combining the characteristic basis function method and the multilevel fast multipole algorithm. *IEEE Trans. Antennas Propag.*, **56**(8), 2363–2371, Aug 2008.

[48] W. Geyi. Physical limitations of antenna. *IEEE Trans. Antennas Propag.*, **51**(8), 2116–2123, August 2003.

[49] W. C. Gibson. *The Method of Moments in Electromagnetics.* CRC press, 2014.

[50] A. W. Glisson and D. R. Wilton. Simple and efficient numerical methods for problems of electromagnetic radiation and scattering from surfaces. *IEEE Trans. Antennas Propag.*, **28**(5), 593–603, September 1980.

[51] D. Goldberg. What every computer scientist should know about floating-point arithmetic. *ACM Computing Surveys (CSUR)*, **23**(1), 5–48, 1991.

[52] G. H. Golub and C. F. van Loan. *Matrix Computations.* The Johns Hopkins University Press, Baltimore, MD, 4 edition, 2013.

[53] D. Gonzalez-Ovejero, E. d. L. Acedo, N. Razavi-Ghods, and C. Craeye. Fast MBF based method for large random array characterization. In *IEEE Antennas and Propagation Society International Symposium*, pages 1–4. IEEE, 2009.

[54] R. D. Graglia and G. Lombardi. Machine precision evaluation of singular and nearly singular potential integrals by use of gauss quadrature formulas for rational functions. *IEEE Trans. Antennas Propag.*, **56**(4), 981–998, April 2008.

[55] M. Grant and S. Boyd. CVX: Matlab software for disciplined convex programming, version 1.21. `http://cvxr.com/cvx`, April 2011.

[56] G. Green. *An essay on the application of mathematical analysis to the theories of electricity and magnetism.* Nottingham, T. Wheelhouse, 1828.

[57] L. Greengard. Fast Algorithms for Classical Physics. *Science*, **265**(5174), 909–914, 1994.

[58] M. Gustafsson, M. Capek, and K. Schab. Trade-off between antenna efficiency and Q-factor. Technical Report LUTEDX/(TEAT-7260)/1–11/(2017), Lund University, Department of Electrical and Information Technology, P.O. Box 118, S-221 00 Lund, Sweden, 2017.

[59] M. Gustafsson, M. Cismasu, and S. Nordebo. Absorption efficiency and physical bounds on antennas. *International Journal of Antennas and Propagation*, **2010**(Article ID 946746), 1–7, 2010.

[60] M. Gustafsson and B. L. G. Jonsson. Antenna Q and stored energy expressed in the fields, currents, and input impedance. *IEEE Trans. Antennas Propag.*, **63**(1), 240–249, 2015.

[61] M. Gustafsson and B. L. G. Jonsson. Stored electromagnetic energy and antenna Q. *Progress In Electromagnetics Research (PIER)*, **150**, 13–27, 2015.

[62] M. Gustafsson and S. Nordebo. Bandwidth, Q-factor, and resonance models of antennas. *Prog. Electromagn. Res.*, **62**, 1–20, 2006.

[63] M. Gustafsson and S. Nordebo. Optimal antenna currents for Q, superdirectivity, and radiation patterns using convex optimization. *IEEE Trans. Antennas Propag.*, **61**(3), 1109–1118, 2013.

[64] M. Gustafsson, C. Sohl, and G. Kristensson. Physical limitations on antennas of arbitrary shape. *Proc. R. Soc. A*, **463**, 2589–2607, 2007.

[65] M. Gustafsson, C. Sohl, and G. Kristensson. Illustrations of new physical bounds on linearly polarized antennas. *IEEE Trans. Antennas Propag.*, **57**(5), 1319–1327, May 2009.

[66] M. Gustafsson, D. Tayli, C. Ehrenborg, M. Cismasu, and S. Nordebo. Antenna current optimization using MATLAB and CVX. *FERMAT*, **15**(5), 1–29, 2016.

[67] M. Gustafsson, M. Cismasu, and B. L. G. Jonsson. Physical bounds and optimal currents on antennas. *IEEE Trans. Antennas Propag.*, **60**(6), 2672–2681, 2012.

[68] M. Gustafsson and S. Nordebo. Characterization of MIMO antennas using spherical vector waves. *IEEE Trans. Antennas Propag.*, **54**(9), 2679–2682, 2006.

[69] M. Gustafsson, D. Tayli, and M. Cismasu. Q factors for antennas in dispersive media. Technical Report LUTEDX/(TEAT-7232)/1–24/(2014), Lund University, Department of Electrical and Information Technology and P.O. Box 118 and S-221 00 Lund, Sweden, 2014. http://www.eit.lth.se.

[70] M. Gustafsson, D. Tayli, and M. Cismasu. *Physical bounds of antennas*, pages 1–32. Springer-Verlag, 2015.

[71] J. E. O. Guzman, S. B. Adrian, R. Mitharwal, Y. Beghein, T. F. Eibert, K. Cools, and F. P. Andriulli. On the hierarchical preconditioning of the PMCHWT integral equation on simply and multiply connected geometries. *IEEE Antennas Wireless Propag. Lett.*, **16**, 1044–1047, 2017.

[72] J. E. Hansen, editor. *Spherical Near-Field Antenna Measurements.* Number 26 in IEE electromagnetic waves series. Peter Peregrinus Ltd., Stevenage, UK, 1988.

[73] R. C. Hansen. Fundamental limitations in antennas. *Proc. IEEE*, **69**(2), 170–182, 1981.

[74] T. V. Hansen, O. S. Kim, and O. Breinbjerg. Stored energy and quality factor of spherical wave functions–in relation to spherical antennas with material cores. *IEEE Trans. Antennas Propag.*, **60**(3), 1281–1290, 2012.

[75] W. W. Hansen. A new type of expansion in radiation problems. *Phys. Rev.*, **47**(2), 139, 1935.

[76] W. W. Hansen and J. R. Woodyard. A new principle in directional antenna design. *Proc. IRE*, **26**(3), 333–345, 1938.

[77] R. F. Harrington. Effect of antenna size on gain, bandwidth and efficiency. *Journal of Research of the National Bureau of Standards – D. Radio Propagation*, **64D**, 1–12, January – February 1960.

[78] R. F. Harrington. *Field Computation by Moment Methods.* Macmillan, New York, NY, 1968.

[79] R. F. Harrington and J. R. Mautz. Computation of characteristic modes for conducting bodies. *IEEE Trans. Antennas Propag.*, **19**(5), 629–639, 1971.

[80] R. F. Harrington and J. R. Mautz. Theory of characteristic modes for conducting bodies. *IEEE Trans. Antennas Propag.*, **19**(5), 622–628, 1971.

[81] R. F. Harrington and J. R. Mautz. Control of radar scattering by reactive loading. *IEEE Trans. Antennas Propag.*, **20**(4), 446–454, 1972.

[82] R. L. Haupt and D. H. Werner. *Genetic Algorithms in Electromagnetics.* Wiley-IEEE Press, 2007.

[83] A. Heldring, E. Ubeda, and J. M. Rius. Simultaneously improving the efficiency and compression of the adaptive cross approximation algorithm. In *Electromagnetics in Advanced Applications (ICEAA), 2015 International Conference on*, pages 16–18. IEEE, 2015.

[84] Ismatullah and T. F. Eibert. Adaptive singularity cancellation for efficient treatment of near-singular and near-hypersingular integrals in surface integral equation formulations. *IEEE Trans. Antennas Propag.*, **56**(1), 274–278, January 2008.

[85] J. D. Jackson. *Classical Electrodynamics.* John Wiley & Sons, New York, NY, third edition, 1999.

[86] L. Jelinek and M. Capek. Optimal currents on arbitrarily shaped surfaces. *IEEE Trans. Antennas Propag.*, **65**(1), 329–341, 2017.

[87] J. M. Jin. *Theory and Computation of Electromagnetic Fields.* Wiley Online Library, 2010.

[88] F. Johansson et al. mpmath: a Python library for arbitrary-precision floating-point arithmetic (version 0.18). `http://mpmath.org/`, December 2013. Accessed: 2017-12-20.

[89] J. M. Johnson and Y. Rahmat-Samii. Genetic algorithms and method of moments GA/MOM for the design of integrated antennas. *IEEE Trans. Antennas Propag.*, **47**(10), 1606–1614, oct 1999.

[90] B. L. G. Jonsson and M. Gustafsson. Stored energies in electric and magnetic current densities for small antennas. *Proc. R. Soc. A*, **471**(2176), 20140897, 2015.

[91] B. L. G. Jonsson, C. I. Kolitsidas, and N. Hussain. Array antenna limitations. *IEEE Antennas Wireless Propag. Lett.*, **12**, 1539–1542, 2013.

[92] B. Jonsson, S. Shi, L. Wang, F. Ferrero, and L. Lizzi. On methods to determine bounds on the Q-factor for a given directivity. *arXiv preprint arXiv:1702.03234*, 2017.

[93] L. V. Kantorovich and V. I. Krylov. *Approximate Methods of Higher Analysis.* Noordhoff, 1958.

[94] A. Karlsson. Physical limitations of antennas in a lossy medium. *IEEE Trans. Antennas Propag.*, **52**, 2027–2033, 2004.

[95] M. A. Khayat and D. R. Wilton. Numerical evaluation of singular and near-singular potential integrals. *IEEE Trans. Antennas Propag.*, **53**(10), 3180–3190, October 2005.

[96] R. W. P. King and S. S. Sandler. The theory of endfire arrays. *IEEE Trans. Antennas Propag.*, **12**(3), 276–280, 1964.

[97] R. E. Kleinman and T. B. A. Senior. Rayleigh scattering. In V. V. Varadan and V. K. Varadan, editors, *Low and high frequency asymptotics*, volume 2 of *Handbook on Acoustic, Electromagnetic and Elastic Wave Scattering*, chapter 1, pages 1–70. Elsevier Science Publishers, Amsterdam, 1986.

[98] J. D. Kraus and R. J. Marhefka. *Antennas.* McGraw-Hill, New York, NY, third edition, 2002.

[99] G. Kristensson. *Scattering of Electromagnetic Waves by Obstacles.* SciTech Publishing, an imprint of the IET, Edison, NJ, 2016.

[100] H. Lebret and S. Boyd. Antenna array pattern synthesis via convex optimization. *IEEE Trans. Signal Process.*, **45**(3), 526–532, 1997.

[101] H. Li, Z. Miers, and B. K. Lau. Design of orthogonal MIMO handset antennas based on characteristic mode manipulation at frequency bands below 1 GHz. *IEEE Trans. Antennas Propag.*, **62**(5), 2756–2766, 2014.

[102] D. Liu, R. J. Garbacz, and D. M. Pozar. Antenna synthesis and optimization using generalized characteristic modes. *IEEE Trans. Antennas Propag.*, **38**(6), 862–868, Jun 1990.

[103] Y. Lo, S. Lee, and Q. Lee. Optimization of directivity and signal-to-noise ratio of an arbitrary antenna array. *IEE Proceedings*, **54**(8), 1033–1045, 1966.

[104] R. Maaskant, R. Mittra, and A. Tijhuis. Application of trapezoidal-shaped characteristic basis functions to arrays of electrically interconnected antenna elements. In *Electromagnetics in Advanced Applications, 2007. ICEAA 2007. International Conference on*, pages 567–571. IEEE, 2007.

[105] R. Maaskant, R. Mittra, and A. Tijhuis. Multi-level characteristic basis function method (MLCBFM) for the analysis of large antenna arrays. *Radio Science Bulletin*, **336**(3), 23–34, 2011.

[106] R. Maaskant, R. Mittra, and A. Tijhuis. Fast analysis of large antenna arrays using the characteristic basis function method and the adaptive cross approximation algorithm. *IEEE Trans. Antennas Propag.*, **56**(11), 3440–3451, 2008.

[107] M. Manteghi and Y. Rahmat-Samii. Multiport characteristics of a wideband cavity backed annular patch antenna for multipolarization operations. *IEEE Trans. Antennas Propag.*, **53**(1), 466–474, jan 2005.

[108] L. Matekovits, V. A. Laza, and G. Vecchi. Analysis of large complex structures with the synthetic-functions approach. *IEEE Trans. Antennas Propag.*, **55**(9), 2509–2521, 2007.

[109] J. C. Maxwell. *The Electrical Researches of the Honourable Henry Cavendish.* Cambridge, 1879.

[110] J. S. McLean. A re-examination of the fundamental limits on the radiation Q of electrically small antennas. *IEEE Trans. Antennas Propag.*, **44**(5), 672–676, May 1996.

[111] Z. Miers, H. Li, and B. K. Lau. Design of bandwidth-enhanced and multiband mimo antennas using characteristic modes. *IEEE Antennas Wireless Propag. Lett.*, **12**, 1696–1699, 2013.

[112] P. M. Morse and H. Feshbach. *Methods of Theoretical Physics*, volume 1. McGraw-Hill, New York, NY, 1953.

[113] P. M. Morse and H. Feshbach. *Methods of Theoretical Physics*, volume 2. McGraw-Hill, New York, NY, 1953.

[114] T. Ohira. What in the world is Q? *IEEE Microw. Mag.*, **17**(6), 42–49, June 2016.

[115] A. G. Polimeridis and J. R. Mosig. Evaluation of weakly singular integrals via generalized cartesian product rules based on the double exponential formula. *IEEE Trans. Antennas Propag.*, **58**(6), 1980–1988, June 2010.

[116] A. G. Polimeridis, J. M. Tamayo, J. M. Rius, and J. R. Mosig. Fast and accurate computation of hypersingular integrals in Galerkin surface integral equation formulations via the direct evaluation method. *IEEE Trans. Antennas Propag.*, **59**(6), 2329–2340, June 2011.

[117] A. G. Polimeridis, F. Vipiana, J. R. Mosig, and D. R. Wilton. DIRECTFN: Fully numerical algorithms for high precision computation of singular integrals in Galerkin SIE methods. *IEEE Trans. Antennas Propag.*, **61**(6), 3112–3122, June 2013.

[118] A. G. Polimeridis. Direct evaluation method in computational electromagnetics (DEMCEM). `https://github.com/thanospol/DEMCEM`, 2010. Accessed: 2017-12-20.

[119] A. G. Polimeridis. DIRECTFN. `https://github.com/thanospol/DIRECTFN`, 2013. Accessed: 2017-12-20.

[120] A. G. Polimeridis and J. R. Mosig. Complete semi-analytical treatment of weakly singular integrals on planar triangles via the direct evaluation method. *Int. J. Numer. Meth. Engng.*, **83**(12), 1625–1650, September 2010.

[121] A. G. Polimeridis and J. R. Mosig. On the direct evaluation of surface integral equation impedance matrix elements involving point singularities. *IEEE Trans. Antennas Propag.*, **10**, 599–602, 2011.

[122] D. M. Pozar. *Microwave Engineering.* John Wiley & Sons, New York, NY, third edition, 2005.

[123] V. V. S. Prakash and R. Mittra. Characteristic basis function method: A new technique for efficient solution of method of moments matrix equations. *Microwave and Optical Technology Letters*, **36**(2), 95–100, 2003.

[124] S. M. Rao, D. R. Wilton, and A. W. Glisson. Electromagnetic scattering by surfaces of arbitrary shape. *IEEE Trans. Antennas Propag.*, **30**(3), 409–418, 1982.

[125] L. Rayleigh. On the electromagnetic theory of light. *Phil. Mag.*, **12**, 81, 1881.

[126] L. Reinhold and B. Pavel. *RF Circuit Design: Theory and Applications.* Prentice Hall Upper Saddle River, 2000.

[127] K. R. Schab and J. T. Bernhard. Radiation and energy storage current modes on conducting structures. *IEEE Trans. Antennas Propag.*, **63**(12), 5601–5611, Dec 2015.

[128] K. Schab, L. Jelinek, M. Capek, C. Ehrenborg, D. Tayli, G. Vandenbosch, and M. Gustafsson. Energy stored by radiating systems. *IEEE Access*, 2018.

[129] T. B. Senior and J. L. Volakis. *Approximate Boundary Conditions in Electromagnetics.* Number 41. IET, 1995.

[130] A. K. Skrivervik, J.-F. Zürcher, O. Staub, and J. R. Mosig. PCS antenna design: The challenge of miniaturization. *IEEE Antennas Propag. Mag.*, **43**(4), 12–27, August 2001.

[131] K. L. Smith. On the Origins of the Quality Factor Q. *Quarterly Journal of the Royal Astronomical Society*, **27**, 695, December 1986.

[132] J. Song, C.-C. Lu, and W. C. Chew. Multilevel fast multipole algorithm for electromagnetic scattering by large complex objects. *IEEE Trans. Antennas Propag.*, **45**(10), 1488–1493, 1997.

[133] J.-E. Sten, A. Hujanen, and P. Koivisto. Quality factor of an electrically small antenna radiating close to a conducting plane. *IEEE Trans. Antennas Propag.*, **49**(5), 829–837, May 2001.

[134] G. Strang. *Linear Algebra and its Applications.* Elsevier Science, 2014.

[135] C.-T. Tai. *Dyadic Green Functions in Electromagnetic Theory.* IEEE Press, 1994.

[136] D. Tayli, M. Capek, L. Akrou, L. V., J. L., and M. Gustafsson. Accurate and efficient evaluation of characteristic modes. *arXiv preprint arXiv:1709.09976*, 2017.

[137] D. Tayli and M. Gustafsson. Physical bounds for antennas above a ground plane. *IEEE Antennas Wireless Propag. Lett.*, **15**, 1281–1284, 2016.

[138] D. Tayli and M. Gustafsson. Investigating the Q factor and efficiency for lossy antennas using convex optimization. In *Proceedings of the 8th European Conference on Antennas and Propagation (EUCAP)*, 2014.

[139] H. L. Thal. New radiation Q limits for spherical wire antennas. *IEEE Trans. Antennas Propag.*, **54**(10), 2757–2763, October 2006.

[140] G. A. E. Vandenbosch. Reactive energies, impedance, and Q factor of radiating structures. *IEEE Trans. Antennas Propag.*, **58**(4), 1112–1127, 2010.

[141] G. A. E. Vandenbosch. The future of computational electromagnetics: Science or product. In *Proceedings of the 5th European Conference on Antennas and Propagation (EUCAP)*, pages 2831–2832, April 2011.

[142] G. A. E. Vandenbosch. Simple procedure to derive lower bounds for radiation Q of electrically small devices of arbitrary topology. *IEEE Trans. Antennas Propag.*, **59**(6), 2217–2225, 2011.

[143] G. A. E. Vandenbosch. Radiators in time domain, part I: electric, magnetic, and radiated energies. *IEEE Trans. Antennas Propag.*, **61**(8), 3995–4003, 2013.

[144] F. Vipiana and D. R. Wilton. Numerical evaluation via singularity cancellation schemes of near-singular integrals involving the gradient of helmholtz-type potentials. *IEEE Trans. Antennas Propag.*, **61**(3), 1255–1265, March 2013.

[145] P. D. Vita, A. Freni, L. Matekovits, P. Pirinoli, and G. Vecchi. A combined AIM-SFX approach for large complex arrays. In *IEEE Antennas and Propagation Society International Symposium*, pages 3452–3455. IEEE, 2007.

[146] J. Volakis, C. C. Chen, and K. Fujimoto. *Small Antennas: Miniaturization Techniques & Applications*. McGraw-Hill, New York, NY, 2010.

[147] J. L. Volakis and K. Sertel. *Integral Equation Methods for Electromagnetics*. SciTech Publishing Inc., 2012.

[148] P. C. Waterman. Symmetry, unitarity, and geometry in electromagnetic scattering. *Phys. Rev. D*, **3**(4), 825–839, 1971.

[149] H. A. Wheeler. Fundamental limitations of small antennas. *Proc. IRE*, **35**(12), 1479–1484, 1947.

[150] H. Wheeler. Simple relations derived from a phased-array antenna made of an infinite current sheet. *IEEE Trans. Antennas Propag.*, **13**(4), 506–514, 1965.

[151] D. R. Wilton, F. Vipiana, and W. A. Johnson. Evaluation of 4-D reaction integrals in the method of moments: Coplanar element case. *IEEE Trans. Antennas Propag.*, **65**(5), 2479–2493, May 2017.

[152] H. J. Wintle. Maxwell and the boundary element method: a historical puzzle. *IEEE Elec. Insul. Mag.*, **14**(6), 23–25, Nov 1998.

[153] K.-L. Wong. *Planar Antennas for Wireless Communications*. John Wiley & Sons, New York, NY, 2003.

[154] A. D. Yaghjian. Internal energy, Q-energy, Poynting's theorem, and the stress dyadic in dispersive material. *IEEE Trans. Antennas Propag.*, **55**(6), 1495–1505, 2007.

[155] A. D. Yaghjian, M. Gustafsson, and B. L. G. Jonsson. Minimum Q for lossy and lossless electrically small dipole antennas. *Progress In Electromagnetics Research*, **143**, 641–673, 2013.

[156] A. D. Yaghjian and S. R. Best. Impedance, bandwidth, and Q of antennas. *IEEE Trans. Antennas Propag.*, **53**(4), 1298–1324, 2005.

[157] B. Yang and J. J. Adams. Systematic shape optimization of symmetric MIMO antennas using characteristic modes. *IEEE Trans. Antennas Propag.*, **64**(7), 2668–2678, July 2016.

[158] K. Zhao, M. N. Vouvakis, and J.-F. Lee. The adaptive cross approximation algorithm for accelerated method of moments computations of EMC problems. *IEEE Trans. Electromagn. Compat.*, **47**(4), 763–773, 2005.

[159] D. Zuras, M. Cowlishaw, A. Aiken, M. Applegate, D. Bailey, S. Bass, D. Bhandarkar, M. Bhat, D. Bindel, S. Boldo, et al. IEEE standard for floating-point arithmetic. *IEEE Std 754-2008*, pages 1–70, 2008.

Physical Bounds for Antennas Above a Ground Plane

Paper I

Doruk Tayli and Mats Gustafsson

Published as: D. Tayli and M. Gustafsson, “Physical Bounds for Antennas Above a Ground Plane”, *IEEE Antennas Wireless Propagation Letters*, Vol. 15, pp. 1281–1284, 2015.

Abstract

Physical limitations of antennas above infinite perfect electric conductor (PEC) ground planes are determined using the stored electromagnetic energy. Stored energies are computed with the method of moments (MoM) and the image theory. Convex optimization is used to derive the G/Q ratio and Q-factor for a reference geometry and the results are compared for different antenna types.

1 Introduction

The proximity of a conducting ground plane is both a blessing and a curse for antenna designers. In some cases it limits the bandwidth, while in others this additional structure can improve antenna performance significantly [22, 27].

The Q-factor, which is inversely proportional to the fractional bandwidth, is the main and traditional figure of merit for physical bounds [25]. For a system, the Q-factor is defined as the ratio of its stored energy to the dissipated energy per cycle. Similarly, the Q-factor for an antenna is the ratio of stored energy to the radiated fields and antenna losses [5, 12, 13, 25, 26].

Early pioneers in antenna theory, such as Chu [5], have investigated the physical limits of antennas since the late 1940s. Chu calculated the stored energies analytically using spherical mode expansions, excluding a small spherical region near the antenna. Although his calculations are restricted to antennas circumscribed by a sphere, they were a significant breakthrough for its time.

Today progresses in both theory and computing tools in the field allow the analysis of antennas with different geometries. Physical bounds for antennas of arbitrary shape and size were computed using the forward scattering sum rule in [13]; whereas antenna current optimization is used to compute the physical bounds of arbitrary metallic structures using method of moments (MoM) software for antennas in free-space as well as antennas with finite ground planes in [6, 12, 14]. The comparison of these different techniques with planar and cylindrical antennas can be found in [2, 10, 13, 20, 21]

This paper extends the physical bounds calculation to cover a new class of antennas, antennas above an infinite ground plane. Previous research on this topic has been conducted for low-frequency limit using spherical harmonics in [23], vertically polarized antennas [13], and infinite antenna arrays [4, 7, 19]. Our approach is based on the application of classical image theory to the calculation of antenna stored energies using the expressions for the stored energy derived by Vandenbosch [24]. The proposed method can calculate the upper bound on G/Q, for any geometry and radiation polarization.

To demonstrate the physical bounds a reference rectangular patch geometry above a ground plane is presented and compared with different patch antenna designs from literature [8]. The selected antennas are simulated using the commercial electromagnetic solver FEKO [1]. The Q-factor of the simulated antennas are computed using both the MoM impedance matrix and the differentiated input impedance [28]. Simulation results show that the Q-factor of the antennas conform to the physical bounds of the reference geometry.

2 Stored Energies and Physical Bounds

While a specific definition is established on energy dissipated by an antenna, the same cannot be claimed for the stored energy. This paper uses the stored electric energy defined by Vandenbosch [24] which is equivalent to the coordinate independent part of the stored energy expression [17]

$$W_{\mathrm{e}} = \frac{\epsilon_0}{4}\int_{\mathbb{R}^3} |\boldsymbol{E}(\boldsymbol{r})|^2 - \frac{|\boldsymbol{F}(\hat{\boldsymbol{r}})|^2}{r^2}\mathrm{dV}. \tag{2.1}$$

In (2.1) $\boldsymbol{E}(\boldsymbol{r})$ and $\boldsymbol{F}(\hat{\boldsymbol{r}})$ are respectively the electric field and the far-field with, $r = |\boldsymbol{r}|$, $\hat{\boldsymbol{r}} = \boldsymbol{r}/r$, and the integration is over an infinite sphere. The magnetic stored energy is similarly obtained by replacing the electric field with the magnetic field in (2.1).

In (2.1), the stored energies are calculated by subtracting the far-field energy density from the electric energy density. It has been shown in [11, 28] that the resulting expression (2.1) is the sum of two terms; one of them is coordinate dependent and the other coordinate independent. The coordinate independent term may yield the stored energy to have negative values [12], an indication that the model is not exact, since the result is unphysical. The coordinate independent term is very accurate for antennas smaller than $ka \leqslant 1$ in dimension, where k is the wavenumber and a is the radius of the smallest sphere enclosing the antenna [11, 17].

The Q-factor, the main parameter in quantifying the physical limits of antennas, can also be used in optimization problems. For a lossless antenna the Q-factor is usually defined as [16, 28];

$$Q = \frac{2\omega \max\{W_{\mathrm{e}}, W_{\mathrm{m}}\}}{P_{\mathrm{d}}}, \tag{2.2}$$

where ω is the angular frequency, W_{e} is the stored electric energy, W_{m} stored magnetic energy, and P_{d} is the dissipated power. A useful approximation of the Q-factor is the derivative of antenna input impedance, Z_{in}, tuned to resonance [28],

$$Q_{\mathrm{Z}'_{\mathrm{in}}} = \frac{\omega|Z'_{\mathrm{in}}|}{2R_{\mathrm{in}}}, \tag{2.3}$$

where the terms Z'_{in} and R_{in} are the derivative of the tuned input impedance with respect to angular frequency, and the real part of the input impedance, respectively. It is assumed that the antenna is tuned to resonance with a single circuit element, which can be either capacitive or inductive (2.3).

The Q-factor can be calculated from the MoM impedance matrix and its frequency derivative [15]. The impedance matrix is written as the sum of its real and imaginary parts, $\mathbf{Z} = \mathbf{R} + \mathrm{j}\mathbf{X}$. The difference of stored energies are derived as

$$W_\mathrm{m} + W_\mathrm{e} = \frac{1}{4}\mathbf{I}^\mathrm{H}\mathbf{X}'\mathbf{I}, \tag{2.4}$$

$$W_\mathrm{m} - W_\mathrm{e} = \frac{1}{4\omega}\mathbf{I}^\mathrm{H}\mathbf{X}\mathbf{I}, \tag{2.5}$$

here $\mathbf{X}'$ is the derivative of the imaginary part of the MoM impedance matrix with respect to the radial frequency, $\mathbf{I}$ is a single column matrix representing surface currents on the antenna structure, and $\mathbf{I}^\mathrm{H}$ is the Hermitian transpose of the surface currents. By substituting one equation to the other, the stored energy expressions are found as

$$W_\mathrm{m} = \frac{1}{8}\mathbf{I}^\mathrm{H}\left(\frac{\partial \mathbf{X}}{\partial \omega} + \frac{\mathbf{X}}{\omega}\right)\mathbf{I} = \frac{1}{4\omega}\mathbf{I}^\mathrm{H}\mathbf{X}_\mathrm{m}\mathbf{I}, \tag{2.6}$$

$$W_\mathrm{e} = \frac{1}{8}\mathbf{I}^\mathrm{H}\left(\frac{\partial \mathbf{X}}{\partial \omega} - \frac{\mathbf{X}}{\omega}\right)\mathbf{I} = \frac{1}{4\omega}\mathbf{I}^\mathrm{H}\mathbf{X}_\mathrm{e}\mathbf{I}, \tag{2.7}$$

both (2.6) and (2.7) can simply be calculated from the MoM impedance matrix. The tuned Q-factor can then be expressed as

$$Q = \frac{\omega\mathbf{I}^\mathrm{H}\mathbf{X}'\mathbf{I} + |\mathbf{I}^\mathrm{H}\mathbf{X}\mathbf{I}|}{2\mathbf{I}^\mathrm{H}\mathbf{R}\mathbf{I}}. \tag{2.8}$$

The partial radiation intensity of an antenna with a unit polarization vector $\hat{\boldsymbol{e}}$ and direction $\hat{\boldsymbol{k}}$, is proportional to the far-field $\boldsymbol{F}(\hat{\boldsymbol{k}})$, and is expressed as

$$\hat{\boldsymbol{e}}^* \cdot \boldsymbol{F}(\hat{\boldsymbol{k}}) = \frac{-\mathrm{j}\omega\eta_0}{4\pi}\int_S \hat{\boldsymbol{e}}^* \cdot \boldsymbol{J}(\boldsymbol{r})\mathrm{e}^{\mathrm{j}k\hat{\boldsymbol{k}}\cdot\boldsymbol{r}}\,\mathrm{dS}, \tag{2.9}$$

where η_0 is impedance of free space and k is the wavenumber. The partial gain is defined as

$$G(\hat{\boldsymbol{k}}, \hat{\boldsymbol{e}}) = \frac{2\pi}{\eta_0}\frac{|\hat{\boldsymbol{e}}^* \cdot \boldsymbol{F}(\hat{\boldsymbol{k}})|^2}{P_\mathrm{d}}, \tag{2.10}$$

the G/Q ratio is determined from (2.2) and (2.10)

$$\frac{G(\hat{\boldsymbol{k}}, \hat{\boldsymbol{e}})}{Q} = \frac{\pi|\hat{\boldsymbol{e}}^* \cdot \boldsymbol{F}(\hat{\boldsymbol{k}})|^2}{\omega\eta_0 \max\{W_\mathrm{e}, W_\mathrm{m}\}}. \tag{2.11}$$

3 Antennas Above Ground Planes

Assuming an infinite perfect electric conductor (PEC) plane in the xy-plane Fig. 1, the current density can be decomposed into horizontal and vertical components. The current density is expressed as $\boldsymbol{J}(\boldsymbol{r}) = \boldsymbol{J}_\mathrm{v}(\boldsymbol{r}) + \boldsymbol{J}_\mathrm{h}(\boldsymbol{r})$ above the

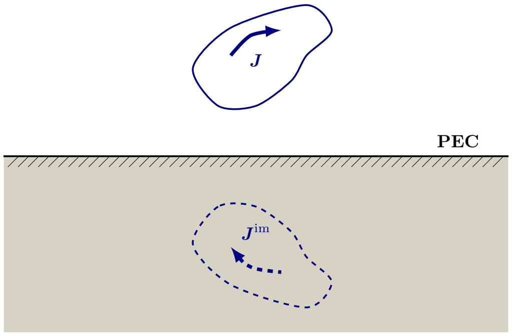

Figure 1: The image current density $\boldsymbol{J}^{\mathrm{im}}$ of an arbitrarily placed current density $\boldsymbol{J}$

PEC plane and its image current is written as [18]

$$\boldsymbol{J}^{\mathrm{im}}(\boldsymbol{r}) = \boldsymbol{J}_{\mathrm{v}}(\boldsymbol{r}_{\mathrm{i}}) - \boldsymbol{J}_{\mathrm{h}}(\boldsymbol{r}_{\mathrm{i}}) = \hat{\boldsymbol{z}}\hat{\boldsymbol{z}} \cdot \boldsymbol{J}(\boldsymbol{r}_{\mathrm{i}}) - [\boldsymbol{J}(\boldsymbol{r}_{\mathrm{i}}) - \hat{\boldsymbol{z}}\hat{\boldsymbol{z}} \cdot \boldsymbol{J}(\boldsymbol{r}_{\mathrm{i}})]\,, \tag{3.1}$$

where $\boldsymbol{r} = x\hat{\boldsymbol{x}} + y\hat{\boldsymbol{y}} + z\hat{\boldsymbol{z}}$ and $\boldsymbol{r}_i = x\hat{\boldsymbol{x}} + y\hat{\boldsymbol{y}} - z\hat{\boldsymbol{z}}$ are the positions of the current density and its image respectively. The dyadic Green's function for solving this problem can be written as [18]

$$\begin{aligned}\mathbf{G}\left(\boldsymbol{r}_1, \boldsymbol{r}_2\right) = {} & [G(\boldsymbol{r}_1, \boldsymbol{r}_2) - G(\boldsymbol{r}_1, \boldsymbol{r}_{2\mathrm{i}})]\,(\hat{\boldsymbol{x}}\hat{\boldsymbol{x}} + \hat{\boldsymbol{y}}\hat{\boldsymbol{y}}) \\ & + [G(\boldsymbol{r}_1, \boldsymbol{r}_2) + G(\boldsymbol{r}_1, \boldsymbol{r}_{2\mathrm{i}})]\,\hat{\boldsymbol{z}}\hat{\boldsymbol{z}} \;= \mathbf{G}_{\|} + \mathbf{G}_{\perp}\end{aligned} \tag{3.2}$$

here $\boldsymbol{r}_2$ is the source position, $\boldsymbol{r}_1$ is the observation point, $\mathbf{G}_{\|}$ is the parallel Green's dyadic, $\mathbf{G}_{\perp}$ is the orthogonal Green's dyadic, and G is the free-space Green's function. For horizontal currents ($\hat{\boldsymbol{x}}$ or $\hat{\boldsymbol{y}}$ directed) the source current and image current are subtracted, while for vertical currents ($\hat{\boldsymbol{z}}$ directed) the source and image currents are added.

An in-house MoM electric field integral equation (EFIE) implementation with Galerkin test functions has been used to compute the stored energies. The MoM impendence matrix elements for antennas above ground plane can be written by substituting (3.2) to the free-space Green's function

$$\begin{aligned}Z_{mn} = \mathrm{j}k\eta_0 \int_S\!\!\int_S \Big[& \boldsymbol{\psi}_m(\boldsymbol{r}_1) \cdot \boldsymbol{\psi}_n(\boldsymbol{r}_2) \\ & - \frac{1}{k^2}\nabla_1 \cdot \boldsymbol{\psi}_m(\boldsymbol{r}_1)\nabla_2 \cdot \boldsymbol{\psi}_n(\boldsymbol{r}_2)\Big]\tilde{G}\left(\boldsymbol{r}_1, \boldsymbol{r}_2\right) \mathrm{dS}_1\, \mathrm{dS}_2,\end{aligned} \tag{3.3}$$

here Z_{mn} denotes the elements of the MoM impedance matrix, $\boldsymbol{\psi}_m$ and $\boldsymbol{\psi}_n$ are the expansion of source and test basis functions that are obtained by expanding the currents in basis functions, $\boldsymbol{J}(\boldsymbol{r}) = \sum_{n=1}^{N} I_n \boldsymbol{\psi}_n(\boldsymbol{r})$. The $\tilde{G}$ Green's function is the parallel Green's dyadic or the orthogonal Green's dyadic, or their sums depending on the direction of the basis function.

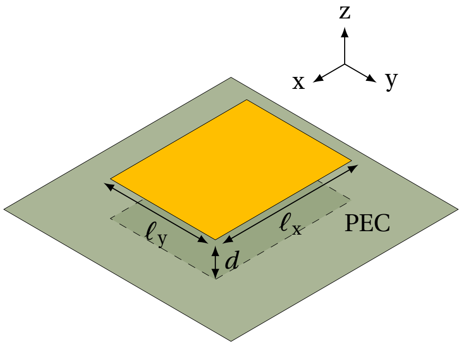

Figure 2: The reference patch geometry of dimensions ℓ_x, $\ell_y = 0.77\ell_x$ with a height of d above an infinite PEC ground plane.

The stored energy expressions (2.6), (2.7) are then used to optimize the antenna G/Q quotient. Formulating the physical bounds for the maximal G/Q quotient results in a convex optimization problem. The physical bounds are computed using convex optimization [3], where the G/Q quotient is optimized by finding the best arrangement of surface currents over the antenna geometry. This approach allows the optimization of the antenna bandwidth for different polarizations and/or radiation patterns. The convex optimization problem can be written as [12]

$$\begin{aligned} &\text{minimize} && \max\{\mathbf{I}^{\mathrm{H}}\mathbf{X}_{\mathrm{e}}\mathbf{I}, \mathbf{I}^{\mathrm{H}}\mathbf{X}_{\mathrm{m}}\mathbf{I}\} \\ &\text{subject to} && \mathrm{Re}\{\mathbf{F}\mathbf{I}\} = 1 \end{aligned} \tag{3.4}$$

the $\mathbf{F}$ is a matrix which specifies the radiation polarization and direction (2.9). The convex optimization problem (3.4) can be readily solved using the Matlab toolbox CVX [9].

4 Numerical Examples

The physical bounds for a reference metallic rectangular geometry (Fig. 2) are calculated using the convex optimization formulation (3.4). The geometry has a dimension of $\ell_y = 0.77\ell_x$. It is placed above an infinite PEC ground plane and the bounds are computed for three different patch heights $d = \{0.01, 0.05, 0.1\}\ell_x$ radiating in the $\hat{\boldsymbol{k}} = \hat{\boldsymbol{z}}$ direction, with either $\hat{\boldsymbol{x}}$, $\hat{\boldsymbol{y}}$ polarization. It should be noted that computation of the physical bounds do not require a feed point. The physical bounds for the patch in Fig. 2 are illustrated in Fig. 3 and Fig. 4 with respect to ℓ_x/λ, the patch length normalized to the wavelength. As expected, the G/Q bound and hence the patch bandwidth deteriorates rapidly as the proximity to the ground plane increases.

The physical bounds of the reference rectangular region are also compared with different patch antennas with identical maximum dimensions, for a height

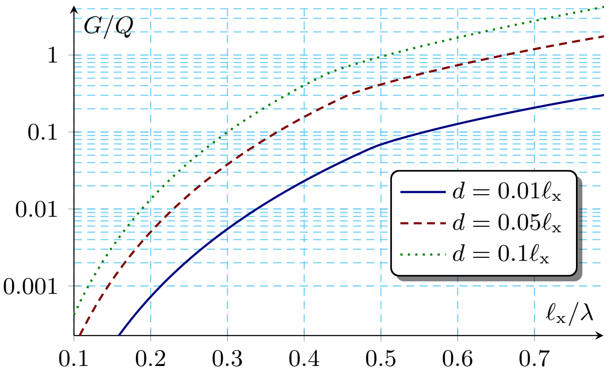

Figure 3: Physical bounds G/Q for a patch above a PEC ground plane for different patch heights $d = \{0.01, 0.05, 0.1\}\ell_x$.

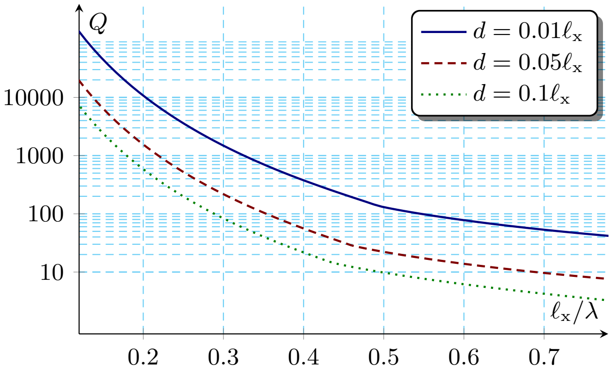

Figure 4: The resulting Q-factor from the physical bounds Fig. 3 for a patch above a PEC ground plane for different patch heights $d = \{0.01, 0.05, 0.1\}\ell_x$.

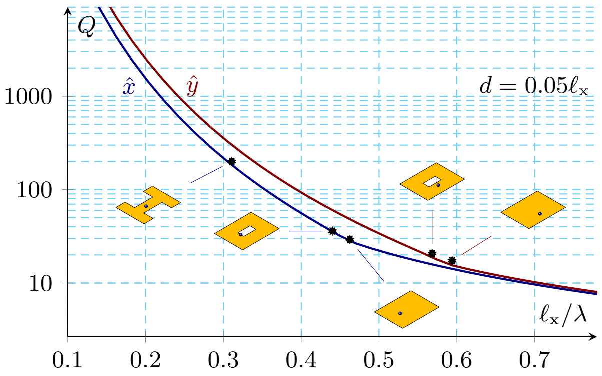

Figure 5: Comparison of the Q-factor from the physical bound on G/Q for the patch geometry in Fig. 2 with $d = 0.05\ell_{\mathrm{x}}$ for six patch antennas.

of $d = 0.05\ell_{\mathrm{x}}$. The patch antennas are simulated in FEKO and matched to 50Ω. The Q-factors are computed with (2.3). The comparison of the physical bounds and antenna Q-factor is illustrated in Fig. 5. The simulated patch antennas match the physical bounds and demonstrate that the bound for a single rectangular patch cannot be exceeded using special geometries or configurations.

The simulated antennas include: a rectangular patch antenna, a slot loaded patch antenna, a H-shaped antenna. From these the rectangular patch and the slot loaded patch are fed in both $\hat{\boldsymbol{x}}$ and $\hat{\boldsymbol{y}}$ polarizations. The feed points for the patch antenna are $0.18\ell_{\mathrm{x}}$ for $\hat{\boldsymbol{x}}$ and $0.25\ell_{\mathrm{x}}$ for $\hat{\boldsymbol{y}}$ polarization from the center of the antenna. The slot size of the slot loaded antenna is $(0.2 \times 0.2)\ell_{\mathrm{x}}$ and the feed points are located at $0.1\ell_{\mathrm{x}}$ for $\hat{\boldsymbol{x}}$ and $0.2\ell_{\mathrm{x}}$ for $\hat{\boldsymbol{y}}$ polarization from the center. The H-shaped antenna feed point is located at $0.06\ell_{\mathrm{x}}$ from the center of the antenna. All of the antennas are matched to 50 Ω and their Q-factor is calculated using (2.3) at the match frequency. The H-shaped antenna and slot antennas resonate at lower frequencies than the patch antenna as the effective length is increased by extending the current path in both antenna types.

5 Conclusion

The paper discusses the estimation of the physical bounds of antennas above a PEC ground plane, based on the classical image theory and the use of Vandenbosch‘s expressions for stored energy. The proposed method calculates the Q-factor for antennas of any geometry and radiation polarization. Numerical results performed for a metallic rectangular region match well with the simulation results using FEKO. Further work should include multi-layered dielectric patches.

References

[1] S. A. Altair Development S.A. (Pty) Ltd Stellenbosch. FEKO, Field Computations Involving Bodies of Arbitrary Shape, Suite 7.0, 2014. `https://www.feko.info/`, Retrieved: 24/11/2014.

[2] S. R. Best. Electrically small resonant planar antennas: Optimizing the quality factor and bandwidth. *IEEE Antennas Propag. Mag.*, **57**(3), 38–47, June 2015.

[3] S. P. Boyd and L. Vandenberghe. *Convex Optimization.* Cambridge Univ. Pr., 2004.

[4] H.-C. Chang, Y. H. Cho, and D.-H. Kwon. Radiation Q bounds for small electric dipoles over a conducting ground plane. *IEEE Trans. Antennas Propag.*, **62**(4), 2031–2040, 2014.

[5] L. J. Chu. Physical limitations of omni-directional antennas. *J. Appl. Phys.*, **19**, 1163–1175, 1948.

[6] M. Cismasu and M. Gustafsson. Antenna bandwidth optimization with single frequency simulation. *IEEE Trans. Antennas Propag.*, **62**(3), 1304–1311, 2014.

[7] J. P. Doane, K. Sertel, and J. L. Volakis. Matching bandwidth limits for arrays backed by a conducting ground plane. *IEEE Trans. Antennas Propag.*, **61**(5), 2511–2518, 2013.

[8] R. Garg. *Microstrip Antenna Design Handbook.* Antennas and Propagation Library. Artech House, 2001.

[9] M. Grant and S. Boyd. CVX: Matlab software for disciplined convex programming, version 1.21. `http://cvxr.com/cvx`, April 2011.

[10] M. Gustafsson, M. Cismasu, and S. Nordebo. Absorption efficiency and physical bounds on antennas. *International Journal of Antennas and Propagation*, **2010**(Article ID 946746), 1–7, 2010.

[11] M. Gustafsson and B. L. G. Jonsson. Antenna Q and stored energy expressed in the fields, currents, and input impedance. *IEEE Trans. Antennas Propag.*, **63**(1), 240–249, 2015.

[12] M. Gustafsson and S. Nordebo. Optimal antenna currents for Q, superdirectivity, and radiation patterns using convex optimization. *IEEE Trans. Antennas Propag.*, **61**(3), 1109–1118, 2013.

[13] M. Gustafsson, C. Sohl, and G. Kristensson. Illustrations of new physical bounds on linearly polarized antennas. *IEEE Trans. Antennas Propag.*, **57**(5), 1319–1327, May 2009.

[14] M. Gustafsson, M. Cismasu, and B. L. G. Jonsson. Physical bounds and optimal currents on antennas. *IEEE Trans. Antennas Propag.*, **60**(6), 2672–2681, 2012.

[15] M. Gustafsson, D. Tayli, and M. Cismasu. Q factors for antennas in dispersive media. Technical Report LUTEDX/(TEAT-7232)/1–24/(2014), Lund University, Department of Electrical and Information Technology and P.O. Box 118 and S-221 00 Lund, Sweden, 2014. http://www.eit.lth.se.

[16] R. F. Harrington. *Field Computation by Moment Methods*. Macmillan, New York, NY, 1968.

[17] P. Hazdra, M. Capek, and J. Eichler. Radiation Q-factors of thin-wire dipole arrangements. *Antennas and Wireless Propagation Letters, IEEE*, **10**, 556–560, 2011.

[18] J. M. Jin. *Theory and Computation of Electromagnetic Fields*. Wiley, 2011.

[19] B. L. G. Jonsson, C. I. Kolitsidas, and N. Hussain. Array antenna limitations. *IEEE Antennas Wireless Propag. Lett.*, **12**, 1539–1542, 2013.

[20] K. Mohammadpour-Aghdam, R. Faraji-Dana, G. A. Vandenbosch, S. Radiom, and G. G. Gielen. Physical bound on Q factor for planar antennas. In *Microwave Conference (EuMC), 2011 41st European*, pages 250–252. IEEE, 2011.

[21] M. Shahpari, D. Thiel, and A. Lewis. An investigation into the Gustafsson limit for small planar antennas using optimization. *IEEE Trans. Antennas Propag.*, **62**(2), 950–955, Feb 2014.

[22] A. K. Skrivervik, J.-F. Zürcher, O. Staub, and J. R. Mosig. PCS antenna design: The challenge of miniaturization. *IEEE Antennas Propag. Mag.*, **43**(4), 12–27, August 2001.

[23] J.-E. Sten, A. Hujanen, and P. Koivisto. Quality factor of an electrically small antenna radiating close to a conducting plane. *IEEE Trans. Antennas Propag.*, **49**(5), 829–837, May 2001.

[24] G. A. E. Vandenbosch. Reactive energies, impedance, and Q factor of radiating structures. *IEEE Trans. Antennas Propag.*, **58**(4), 1112–1127, 2010.

[25] J. Volakis, C. C. Chen, and K. Fujimoto. *Small Antennas: Miniaturization Techniques & Applications*. McGraw-Hill, New York, NY, 2010.

[26] H. A. Wheeler. Fundamental limitations of small antennas. *Proc. IRE*, **35**(12), 1479–1484, 1947.

[27] K.-L. Wong. *Planar Antennas for Wireless Communications*. John Wiley & Sons, New York, NY, 2003.

[28] A. D. Yaghjian and S. R. Best. Impedance, bandwidth, and Q of antennas. *IEEE Trans. Antennas Propag.*, **53**(4), 1298–1324, 2005.

Fundamental Bounds and Optimization of Small Antennas

Paper II

Doruk Tayli, Marius Cismasu, and Mats Gustafsson

Submitted: D. Tayli, M. Cismasu, and M. Gustafsson, "Fundamental bounds and optimization of small antennas", *Developments in Antenna Analysis and Synthesis*, edited by R. Mittra, IET, *in press*, 2018.

Abstract

This chapter discusses fundamental bounds of small antennas and their use in small antenna optimization. Different techniques to estimate and compute the Q-factor and fundamental bounds are presented based on the Q and $Q_{\mathrm{Z}'_{\mathrm{in}}}$ computation from current densities and antenna current optimization. Genetic algorithm (GA) is reviewed, followed by a step-by-step demonstration of its use in small antenna optimization. Examples using the fundamental bounds and the GA to design a simplified small antenna in a mobile wireless terminal are presented. A final example illustrates the use of current optimization for small antenna placement on a mobile wireless terminal.

1 Introduction

Mobile wireless standards have been introduced nearly every decade since early 80's. The introduction of a new standard increases performance requirements and expected capabilities of mobile terminal components. For instance, multiple antennas are expected to fit into confined spaces on a terminal. As an antenna's performance is restricted by its physical size, this presents a challenge for antenna designers [57].

Fundamental bounds are a figure of merit that specify the optimal performance of an antenna with respect to one or several performance parameters [6,8,11,13,21–23,27,28,33,37,46,52,54,58,61]. In case of a mobile terminal the most important parameters are bandwidth, efficiency, and capacity. It has been demonstrated in [21, 23] that the fundamental bounds of any arbitrary shaped antenna can be determined using antenna current optimization. One other widely used performance indicator is the Q-factor computed from the derivative of the input impedance [61]. The latter provides a close estimate of the bandwidth for narrow band antennas. It has recently been shown that the Q-factor can also be computed from the current distribution on a radiating structure at a single frequency [19, 21, 24, 56]. This method is based on expressing the electric and magnetic energies stored in the fields, and the power radiated by an antenna in terms of the current densities [56]. The derivation is further explained in [18, 19] where it is shown that it is accurate in many situations, especially for electrically small antennas.

Optimization is widely used in antenna design to search for optimal geometric, material parameters that satisfy antenna performance requirements. One of the popular optimization classes in antenna design is meta-heuristic algorithms such as genetic algorithm (GA), particle swarm, and ant colony. In this chapter a combined genetic algorithm (GA) and method of moments (MoM) with an ant colony optimization technique is used to synthesize antennas [36, 47, 51]. Moreover, the optimization procedure uses a Q-factor estimation method to predict antenna performance [9, 10]. Antenna current optimization is used to compute the fundamental bounds that are then compared with the synthesized structures.

Examples of planar synthesized structures have been analyzed in [9, 10, 51]. Here these are extended to 3D structures that represent simplified models of common mobile wireless terminals [27]. An in-house GA/MoM solver is used to generate/synthesize optimal antennas with minimum Q-factor for these terminals. Furthermore, optimal antenna placement on a terminal is studied using antenna current optimization. Customized bounds and optimum currents are used in the antenna placement study. The objective of this study is to determine the antenna location that maximizes the performance of the device, measured as G/Q-ratio or Q-factor. Single resonance, [20, 61], and multiple resonance Brune synthesis models, [4, 18, 59], are employed to evaluate the Q-factor of the structures from their input impedance. The results have been validated with simulations from the commercial electromagnetic solver ESI-CEM [12].

The chapter is organized as follows. A background overview is presented in Section 2. Stored energies and their computation using the MoM are illustrated in Section 2.1. The single frequency $Q_{\mathrm{Z}'}$ estimation method is presented in Section 2.2. Fundamental bounds on G/Q and the convex optimization formulation are described in Section 2.3. Section 3 presents antenna optimization and the combined GA/MoM simulation setup used to synthesize antennas, including GA and convex optimization. Sections 3.1 and 3.2 describes genetic algorithm (GA) and convex optimization, respectively. Section 4 presents numerical simulations performed in this chapter and their results. The performance and examples of GA/MoM optimized 3D structures are presented and compared with optimum-current performance in Section 4.1. An antenna placement problem using optimum currents and physical limitations is investigated in Section 4.3. The chapter ends with conclusions in Section 5.

2 Stored Energies and Fundamental Bounds for Antenna Analysis and Design

Antenna analysis and design is usually performed using numerical techniques that solve differential and/or integral equations describing an electromagnetic problem. Examples and details of numerical techniques for electromagnetics can be found in text books such as [15, 29, 34, 44]. These techniques are based, in general, on a discretized computation domain. The method of moments (MoM) is a numerical technique where the surface and/or volume of the structure is discretized [15]. When solving an electromagnetic problem with the MoM technique the current density $\boldsymbol{J}$ excited on the structure is approximated in terms of basis functions $\boldsymbol{\psi}_n$ as

$$\boldsymbol{J}(\boldsymbol{r}) \approx \sum_{n=1}^{N} I_n \boldsymbol{\psi}_n(\boldsymbol{r}), \tag{2.1}$$

where $\boldsymbol{r}$ is the position vector, I_n is the current expansion coefficients, and N is the number of basis functions used to approximate the current density. In this chapter we use a Galerkin type MoM implementation of the electric field integral equation (EFIE) using surface currents [15,34,44]. This gives the following system of equations

$$\mathbf{Z}\mathbf{I} = \mathbf{V}, \tag{2.2}$$

where $\mathbf{V}$ is the excitation column matrix, $\mathbf{Z}$ is the impedance matrix describing the structure, and $\mathbf{I}$ is the column matrix containing the current expansion coefficients. The impedance matrix can be written as $\mathbf{Z} = \mathbf{R} + \mathrm{j}\mathbf{X}$, where $\mathbf{R}$ and $\mathbf{X}$ are the real and imaginary parts, respectively. The elements of $\mathbf{Z}$ are,

$$\begin{aligned} Z_{mn} = \mathrm{j}\eta_0 \int_{\partial V}\int_{\partial V} & k\boldsymbol{\psi}_m(\boldsymbol{r}_1)\cdot\boldsymbol{\psi}_n(\boldsymbol{r}_2)\frac{\mathrm{e}^{-\mathrm{j}kR_{12}}}{4\pi R_{12}} \\ & - \frac{1}{k}\nabla_1\cdot\boldsymbol{\psi}_m(\boldsymbol{r}_1)\nabla_2\cdot\boldsymbol{\psi}_n(\boldsymbol{r}_2)\frac{\mathrm{e}^{-\mathrm{j}kR_{12}}}{4\pi R_{12}}\,\mathrm{dS}_1\,\mathrm{dS}_2, \end{aligned} \tag{2.3}$$

where η_0 is the free space impedance, $k = \omega/\mathrm{c}_0$ is the wave number, c_0 is the speed of light in free space, $R_{12} = |\boldsymbol{r}_1 - \boldsymbol{r}_2|$ is the distance between the source and observation points in the two integration domains, and V is the the volume occupied by the antenna, bounded by the surface ∂V. The derivative of the MoM impedance matrix with respect to the wavenumber is,

$$\begin{aligned} \frac{k\partial Z_{mn}}{\eta_0\partial k} = & \int_{\partial V}\int_{\partial V} \mathrm{j}\left(k\boldsymbol{\psi}_m(\boldsymbol{r}_1)\cdot\boldsymbol{\psi}_n(\boldsymbol{r}_2) + \frac{1}{k}\nabla_1\cdot\boldsymbol{\psi}_m(\boldsymbol{r}_1)\nabla_2\cdot\boldsymbol{\psi}_n(\boldsymbol{r}_2)\right)\frac{\mathrm{e}^{-\mathrm{j}kR_{12}}}{4\pi R_{12}} \\ & + \left(k^2\boldsymbol{\psi}_m(\boldsymbol{r}_1)\cdot\boldsymbol{\psi}_n(\boldsymbol{r}_2) - \nabla_1\cdot\boldsymbol{\psi}_m(\boldsymbol{r}_1)\nabla_2\cdot\boldsymbol{\psi}_n(\boldsymbol{r}_2)\right)\frac{\mathrm{e}^{-\mathrm{j}kR_{12}}}{4\pi}\,\mathrm{dS}_1\,\mathrm{dS}_2 \end{aligned} \tag{2.4}$$

which is a straight-forward addition to existing MoM software, and incurs marginal computational cost. It should be noted that the first term on the right-hand-side is identical to (2.3) with an addition instead of a subtraction. Moreover, the second term is a combination of both current and charge terms, and does not involve the $1/R$ singularity of the free-space Green's function.

The Q-factor is the ratio of stored energy to total radiated and dissipated energy in time-harmonic systems [1]. For a lossless antenna the Q-factor is defined as [9, 61]

$$Q = \frac{2\omega\max\{W_\mathrm{e}, W_\mathrm{m}\}}{P_\mathrm{r}} \tag{2.5}$$

here W_e, W_m, P_r are the stored electric energy, stored magnetic energy and radiated power, respectively. This definition is equivalent to that in [1] for resonant antennas. The Q-factor can be used to estimate antenna's fractional bandwidth and is a useful parameter in antenna optimization. An overview of expressions for the Q-factor of antennas can be found in [50].

2.1 Stored Energies

Stored energy of radiating systems is an intricate topic, with a far-reaching history in the antenna community. This is the result of the ambiguous definition of the stored energy in many radiating electromagnetic problems. Recently, both the definition and the history of stored energies have been reviewed in [50].

Stored electric and magnetic energies of the radiating structure presented here are based on the energy expressions derived in [56]. The energies are quadratic forms in terms of the discrete current density matrix **I** [21],

$$W_{\mathrm{e}} \approx \frac{1}{4\omega}\mathbf{I}^{\mathrm{H}}\mathbf{X}_{\mathrm{e}}\mathbf{I} \quad \text{and} \quad W_{\mathrm{m}} \approx \frac{1}{4\omega}\mathbf{I}^{\mathrm{H}}\mathbf{X}_{\mathrm{m}}\mathbf{I}, \tag{2.6}$$

where ω is the angular frequency, $\mathbf{X}_{\mathrm{e}}$ and $\mathbf{X}_{\mathrm{m}}$ are the electric and magnetic reactance matrices, respectively, and the exponent $^{\mathrm{H}}$ denotes Hermitian transpose. The electric and magnetic reactance matrices are obtained from a modified MoM implementation of the impedance matrix $\mathbf{Z}$ and their explicit representations are [21, 56]

$$\begin{aligned} X_{\mathrm{e},mn} = \eta_0 \int_{\partial V}\int_{\partial V} & \nabla_1 \cdot \boldsymbol{\psi}_m(\boldsymbol{r}_1)\nabla_2 \cdot \boldsymbol{\psi}_n(\boldsymbol{r}_2)\frac{\cos(kR_{12})}{4\pi kR_{12}} \\ & - \big(k^2\boldsymbol{\psi}_m(\boldsymbol{r}_1)\cdot\boldsymbol{\psi}_n(\boldsymbol{r}_2) - \nabla_1\cdot\boldsymbol{\psi}_m(\boldsymbol{r}_1)\nabla_2\cdot\boldsymbol{\psi}_n(\boldsymbol{r}_2)\big)\frac{\sin(kR_{12})}{8\pi}\,\mathrm{dS}_1\,\mathrm{dS}_2 \end{aligned} \tag{2.7}$$

and,

$$\begin{aligned} X_{\mathrm{m},mn} = \eta_0 \int_{\partial V}\int_{\partial V} & k^2\boldsymbol{\psi}_m(\boldsymbol{r}_1)\cdot\boldsymbol{\psi}_n(\boldsymbol{r}_2)\frac{\cos(kR_{12})}{4\pi kR_{12}} \\ & - \big(k^2\boldsymbol{\psi}_m(\boldsymbol{r}_1)\cdot\boldsymbol{\psi}_n(\boldsymbol{r}_2) - \nabla_1\cdot\boldsymbol{\psi}_m(\boldsymbol{r}_1)\nabla_2\cdot\boldsymbol{\psi}_n(\boldsymbol{r}_2)\big)\frac{\sin(kR_{12})}{8\pi}\,\mathrm{dS}_1\,\mathrm{dS}_2, \end{aligned} \tag{2.8}$$

these matrices can also be expressed in terms of the imaginary part of the impedance matrix and its derivative (2.4) with respect to angular frequency ω [23, 26, 53]

$$\mathbf{X}_{\mathrm{e}} = \frac{\omega}{2}\left(\frac{\partial\mathbf{X}}{\partial\omega} - \frac{\mathbf{X}}{\omega}\right) \quad \text{and} \quad \mathbf{X}_{\mathrm{m}} = \frac{\omega}{2}\left(\frac{\partial\mathbf{X}}{\partial\omega} + \frac{\mathbf{X}}{\omega}\right) \tag{2.9}$$

combining both equations in (2.9). The sum of the stored energies is written as

$$W_{\mathrm{e}} + W_{\mathrm{m}} \approx \frac{1}{4\omega}\mathbf{I}^{\mathrm{H}}\left(\mathbf{X}_{\mathrm{e}} + \mathbf{X}_{\mathrm{m}}\right)\mathbf{I} = \frac{1}{8}\mathbf{I}^{\mathrm{H}}\mathbf{X}'\mathbf{I} \tag{2.10}$$

where $\mathbf{X}'$ is the derivative of $\mathbf{X}$ with respect to the angular frequency, (2.4).

The power radiated by an antenna can be written as a quadratic form [14, 19, 45, 56],

$$P_{\mathrm{r}} \approx \frac{1}{2}\mathbf{I}^{\mathrm{H}}\mathbf{R}\mathbf{I}, \tag{2.11}$$

where $\mathbf{R} = \mathrm{Re}\{\mathbf{Z}\}$ is the radiation resistance matrix. The Q-factor of a lossless antenna can be expressed in the stored electric and magnetic reactance matrices

$$Q = \frac{2\max\left\{\mathbf{I}^{\mathrm{H}}\mathbf{X}_{\mathrm{e}}\mathbf{I}, \mathbf{I}^{\mathrm{H}}\mathbf{X}_{\mathrm{m}}\mathbf{I}\right\}}{\mathbf{I}^{\mathrm{H}}\mathbf{R}\mathbf{I}}. \tag{2.12}$$

In the case of a self-resonant lossless antenna (2.12) simplifies to

$$Q_{\mathrm{res}} = \frac{\omega}{2} \frac{\mathbf{I}^{\mathrm{H}} \mathbf{X}' \mathbf{I}}{\mathbf{I}^{\mathrm{H}} \mathbf{R} \mathbf{I}}. \tag{2.13}$$

MoM matrices, $\mathbf{Z}$, $\mathbf{X}_{\mathrm{e}}$, *etc.*, are intrinsically suitable for global optimization algorithms such as GA/MoM optimization [36, 47], current optimization [21]. In such algorithms the optimization time of some antenna parameters; *e.g.* the bandwidth may be evaluated using the single frequency expression (2.12) for Q.

2.2 $Q_{\mathrm{Z}'_{\mathrm{in}}}$ Computation from Current Densities

It is also of interest to study another widely used Q-factor definition the $Q_{\mathrm{Z}'_{\mathrm{in}}}$ [61]; that is obtained from the derivative of the input impedance of an antenna. Consider an antenna having the input impedance

$$Z_{\mathrm{in}}(k) = R_{\mathrm{in}}(k) + \mathrm{j}X_{\mathrm{in}}(k). \tag{2.14}$$

This antenna is tuned to achieve resonance at the wave number k_0 using a series-connected, ideal, lumped inductor or capacitor, as in [61]. The input impedance of the tuned antenna becomes

$$Z_{\mathrm{in,t}}(k) = Z_{\mathrm{in}}(k) + \mathrm{j}X_{\mathrm{t}}(k), \tag{2.15}$$

where $X_{\mathrm{t}}(k)$ is the tuning term. In case of a capacitive ($X_{\mathrm{in}}(k_0) < 0$) or inductive ($X_{\mathrm{in}}(k_0) > 0$) input impedance, the tuning term $X_{\mathrm{t}}(k)$ is

$$X_{\mathrm{t}}(k) = \frac{-kX_{\mathrm{in}}(k_0)}{k_0} \quad \text{and} \quad X_{\mathrm{t}}(k) = \frac{-k_0 X_{\mathrm{in}}(k_0)}{k}, \tag{2.16}$$

respectively. At the resonance frequency the input impedance is real valued, *i.e.*

$$Z_{\mathrm{in,t}}(k_0) = R_{\mathrm{in}}(k_0). \tag{2.17}$$

The Q-factor, $Q_{\mathrm{Z}'_{\mathrm{in}}}$, of the antenna tuned to resonance, is [61]

$$Q_{\mathrm{Z}'_{\mathrm{in}}}(k_0) = \frac{k_0 \left| Z'_{\mathrm{in,t}}(k_0) \right|}{2R_{\mathrm{in}}(k_0)}, \tag{2.18}$$

where prime denotes first derivative with respect to wave number. Note the change of variables $k = \omega/\mathrm{c}_0$, performed in order for Z_{in} to be expressed in terms of the same frequency variable as $\mathbf{Z}$, whose elements are (2.3). If the single resonance assumption does not hold, the derivative of the input impedance may approach zero [20], $Q_{\mathrm{Z}'_{\mathrm{in}}} \approx 0$. Replacing (2.15) and (2.16) in (2.18) gives

$$Q_{\mathrm{Z}'_{\mathrm{in}}}(k_0) = \left| \frac{k_0 Z'_{\mathrm{in}}(k_0)}{2R_{\mathrm{in}}(k_0)} + \mathrm{j}\frac{|X_{\mathrm{in}}(k_0)|}{2R_{\mathrm{in}}(k_0)} \right|. \tag{2.19}$$

A MoM solver provides all quantities needed to evaluate (2.19) except Z'_{in}. This quantity is traditionally computed using a numerical approximation based on evaluating Z_{in} for two closely spaced frequencies. Here, we present an alternative approach using current densities to compute $Q_{\mathrm{Z}'_{\mathrm{in}}}$ that only requires a single frequency impedance matrix computation.

The input impedance derivative is expressed in terms of the input admittance. The admittance matrix is $\mathbf{Y} = \mathbf{Z}^{-1}$. This matrix defines the input impedance of the antenna using a voltage gap model of feeding edge elements:

$$Y_{\mathrm{in}} = \frac{\mathbf{V}^{\mathrm{T}}\mathbf{Y}\mathbf{V}}{V_{\mathrm{in}}^2}, \tag{2.20}$$

where V_{in} is the voltage applied across the gap. We assume that the voltage source is real-valued and frequency independent, *i.e.* $\mathbf{V}' = \mathbf{0}$. The input impedance derivative becomes

$$Z'_{\mathrm{in}} = \left(\frac{1}{Y_{\mathrm{in}}}\right)' = -\frac{Y'_{\mathrm{in}}}{Y_{\mathrm{in}}^2} = -\frac{\left(\mathbf{V}^{\mathrm{T}}\mathbf{Y}\mathbf{V}\right)'}{V_{\mathrm{in}}^2 Y_{\mathrm{in}}^2} = -\frac{\mathbf{V}^{\mathrm{T}}\mathbf{Y}'\mathbf{V}}{V_{\mathrm{in}}^2 Y_{\mathrm{in}}^2}. \tag{2.21}$$

Consider the following identity: $\mathbf{0} = \left(\mathbf{Z}^{-1}\mathbf{Z}\right)' = \left(\mathbf{Z}^{-1}\right)'\mathbf{Z} + \mathbf{Z}^{-1}\mathbf{Z}$. Multiplication from the right by $\mathbf{Z}^{-1}$ gives

$$\left(\mathbf{Z}^{-1}\right)' = \mathbf{Y}' = -\mathbf{Z}^{-1}\mathbf{Z}'\mathbf{Z}^{-1} = -\mathbf{Y}\mathbf{Z}'\mathbf{Y}, \tag{2.22}$$

such that the input impedance derivative is obtained as

$$Z'_{\mathrm{in}} = \frac{\mathbf{I}^{\mathrm{T}}\mathbf{Z}'\mathbf{I}}{V_{\mathrm{in}}^2 Y_{\mathrm{in}}^2}, \tag{2.23}$$

using the fact that $\mathbf{Z} = \mathbf{Z}^{\mathrm{T}}$ and $\mathbf{Y} = \mathbf{Y}^{\mathrm{T}}$. Replace (2.23) in (2.19) to obtain

$$Q_{\mathrm{Z}'_{\mathrm{in}}}(k_0) \approx \left| \frac{k_0 Z_{\mathrm{in}}^2(k_0)\mathbf{I}^{\mathrm{T}}\mathbf{Z}'\mathbf{I}}{2R_{\mathrm{in}}(k_0)V_{\mathrm{in}}^2} + \mathrm{j}\frac{|X_{\mathrm{in}}(k_0)|}{2R_{\mathrm{in}}(k_0)} \right|, \tag{2.24}$$

the first derivative with respect to wave number of the impedance matrix, $\mathbf{Z}'$, is computed for the wave number k_0. It should be noted that (2.24) is similar to (2.13), with a transpose in place of the Hermitian transpose. For small antennas the frequency derivative of the real part $\mathbf{R}$ of the impedance matrix $\mathbf{Z}$ is negligible $\mathbf{I}^{\mathrm{T}}\mathbf{Z}'\mathbf{I} \approx \mathbf{I}^{\mathrm{T}}\mathbf{X}'\mathbf{I}$. Therefore the Q-factor for a self-resonant antenna becomes

$$Q_{\mathbf{Z}'} \approx \frac{\omega}{2}\frac{|\mathbf{I}^{\mathrm{T}}\mathbf{X}'\mathbf{I}|}{\mathbf{I}^{\mathrm{H}}\mathbf{R}\mathbf{I}} \leqslant \frac{\omega}{2}\frac{\mathbf{I}^{\mathrm{H}}\mathbf{X}'\mathbf{I}}{\mathbf{I}^{\mathrm{H}}\mathbf{R}\mathbf{I}} \tag{2.25}$$

the inequality holds in the case that $\mathbf{X}'$ is real valued symmetric positive definite matrix and becomes an equality if $\mathbf{I}$ is equiphase. This formulation of the impedance derivative speeds up the computational process significantly as it only requires to compute the impedance matrix once unlike using the numerical difference to compute the derivative of the input impedance.

The corresponding expression for $Q_{Z'_{\text{in}}}$ in [5] differs from (2.24) as the former includes frequency derivatives of the current density and complex conjugates. An expression similar to (2.24) can be derived using a parallel tuning susceptance.

2.3 Fundamental Bounds

The main parameters of interest in small antenna design are the bandwidth, efficiency, input impedance, and SAR [8, 11, 13, 21–23, 28, 37, 46, 52, 54, 58, 61]. In many cases electrically small antenna design becomes a trade-off between the antenna's physical size and its bandwidth. As the antenna becomes smaller its bandwidth performance deteriorates. Therefore, it is important to determine the antennas physical (fundamental) bounds in order to estimate its optimal performance. One common figure-of-merit is the Q-factor , (2.13) and (2.18), as it is related to the inverse of the fractional bandwidth [61].

Physical bounds of antennas have been extensively investigated since the 1940's. Consequently, a plethora of different techniques are available to compute the physical bounds. These can be grouped as in [27] into circuit models [8, 58], mode expansions [11, 13, 28, 37], forward-scattering sum rule [22], and antenna current optimization [7, 19, 21].

Antenna current optimization is a powerful approach in which customized bounds are derived without restrictive assumptions; *e.g.* bounding geometry, electrical size [23]. In antenna current optimization antenna current densities are the parameter of interest. Using the current densities minimization of G/Q and Q can be expressed as optimization problems. For the gain Q-factor quotient, the optimization problem is convex and can be solved using convex optimization [20]. In the case of minimizing the Q-factor the optimization problem is non-convex but a dual problem can be constructed [6]. Once the optimization problem is solved, optimal currents of the antenna are obtained defining an upper bound on the performance of the physical structure. In the gain Q-factor quotient case the optimal currents can be found using the following convex optimization formulation

$$\begin{aligned} &\text{minimize}_{\mathbf{I}} && \max\{\mathbf{I}^{\mathrm{H}}\mathbf{X}_{\mathrm{e}}\mathbf{I}, \mathbf{I}^{\mathrm{H}}\mathbf{X}_{\mathrm{m}}\mathbf{I}\} \\ &\text{subject to} && \mathbf{F}\mathbf{I} = -\mathrm{j}. \end{aligned} \tag{2.26}$$

Alternatively, its dual problem [23] that is maximized over α with the following constraints

$$\begin{aligned} &\text{minimize}_{\mathbf{I}} && \mathbf{I}^{\mathrm{H}}\left(\alpha\mathbf{X}_{\mathrm{e}} + (1-\alpha)\mathbf{X}_{\mathrm{m}}\right)\mathbf{I} \\ &\text{subject to} && \mathbf{F}\mathbf{I} = -\mathrm{j}, \quad 0 \leqslant \alpha \leqslant 1 \end{aligned} \tag{2.27}$$

For a fixed α the solution of (2.27) is

$$\mathbf{I} = \frac{-\mathrm{j}\left(\alpha\mathbf{X}_{\mathrm{e}} + (1-\alpha)\mathbf{X}_{\mathrm{m}}\right)^{-1}\mathbf{F}^{\mathrm{H}}}{\mathbf{F}\left(\alpha\mathbf{X}_{\mathrm{e}} + (1-\alpha)\mathbf{X}_{\mathrm{m}}\right)^{-1}\mathbf{F}^{\mathrm{H}}}, \tag{2.28}$$

with appropriate scaling of $\mathbf{I}$ such that $\mathbf{FI}$ is dimensionless. The $1 \times N$ matrix $\mathbf{F}$, with the elements

$$F_n = \frac{-\mathrm{j}k\eta_0}{4\pi} \int_V \hat{\boldsymbol{e}}^* \cdot \boldsymbol{\psi}_n(\boldsymbol{r}) \mathrm{e}^{\mathrm{j}k\hat{\boldsymbol{k}}\cdot\boldsymbol{r}} \, \mathrm{dV}, \tag{2.29}$$

is used to approximate the far field, $\boldsymbol{F}$, in the fixed direction $\hat{\boldsymbol{k}}$, projected on the polarization vector, $\hat{\boldsymbol{e}}$, as

$$\hat{\boldsymbol{e}}^* \cdot \boldsymbol{F}(\hat{\boldsymbol{k}}) \approx \mathbf{FI}. \tag{2.30}$$

Formulation (2.27) minimizes the energy stored in the fields created by a radiating structure for a fixed partial radiation intensity in a specific direction. A more detailed presentation of the optimization formulations (2.26) and (2.27) and the quantities involved can be found in [21, 23].

3 Antenna Optimization

Antenna performance can be improved by employing various optimization algorithms. These algorithms include different antenna parameters, used as figures of merit; *e.g.* gain, shape, impedance, *etc.*, in their optimization goals. In this chapter we use GA and convex optimization.

An evolutionary optimization method, the GA, has been chosen for the examples presented here mainly due to the specifics of the problems considered. GA belongs to the class of global optimization algorithms, for a non-exhaustive introduction to this class and some of its applications see [3, 16, 31, 32, 39, 41, 42, 48]. Many antennas embedded in modern devices have a performance that can be predicted with a reasonable accuracy by numerical simulation. Such simulations require significant amount of computing power. Furthermore, fine details of the structure need to be modeled which translate into a large number of possible solutions. Attempting to study all possible solutions becomes prohibitive from a practical perspective in many situations. However, heuristic methods have been shown to provide reasonable solutions to optimization problems prohibitive for deterministic methods. A few examples of heuristic optimization methods are genetic algorithms, random search, particle swarm optimization and ant colony [30, 47, 49, 55].

Table 1 explains the procedure to obtain the simulation results. Further details about the items above can be found throughout the chapter: general descriptions are given in Sec. 4 for the problems considered there (item 1). The following two paragraphs introduce the in-house MoM solver and commercial simulator (items 2 and 5). The GA (item 3) is described in more detail in Sec. 3.1. Bounds derived from current optimization (item 4) are the topic of Sec. 2.3.

The in-house MoM-solver is based on Galerkin's method and a mixed-potential EFIE-formulation [29, 34, 44]. The basis and testing functions have a "rooftop"

Table 1: Steps used to obtain the simulation data

1. General description of problem – Definition of the antenna type to be studied, details to be considered, general bounding shape, *etc.*, parameters that apply to later items.

2. Generation of mother matrices – An in-house EFIE-based MoM solver computes the matrices $\mathbf{Z}$, $\mathbf{X}_{\mathrm{e}}$, $\mathbf{X}_{\mathrm{m}}$, $\mathbf{R}$, and $\mathbf{F}$ that describe the antennas studied, see Sec. 2.

3. Performing antenna optimization – The mother matrices are used in GA/MoM [36]; the resulting optimized designs are presented here.

4. Computing the bounds – The mother matrices are used for antenna current optimization [21]; these bounds are used as comparison for the optimized designs of item 3

5. Verification using a commercial simulator – The antennas obtained through optimization at item 3 are evaluated using a commercial simulator.

profile on pairs of adjacent rectangular mesh elements, *i.e.* rectangles sharing a common edge [40], as illustrated in Fig. 4. Such a function has the amplitude linearly increasing toward the common edge and the direction from the first to the second rectangle (numbered according to a fixed mesh element numbering rule). The Green's function $1/R$ singularities for self and near-singular terms are integrated using a change of variable [38].

The commercial electromagnetic solver ESI-CEM [12] is used to verify the results obtained with the in-house solver through genetic optimization. This commercial solver uses a triangular mesh to discretize the surfaces. Therefore, the rectangular mesh used in the in-house simulation software is converted to a triangular mesh to be used in the ESI-CEM solver. The antenna feed location is maintained at the same position in both solvers. The ESI-CEM simulation of the GA/MoM-optimized antenna is used to calculate the cost function. This provides a comparison between the results obtained using the in-house solver and the commercial solver ESI-CEM.

3.1 Genetic Algorithms

Genetic algorithms applied to antenna problems converges with reasonable speed to suboptimal solutions and avoids local extrema [47]. These algorithms mimic human, animal, plant population evolution using genetic principles well-established in genetics–a field of biology. Typically, such principles are conci-

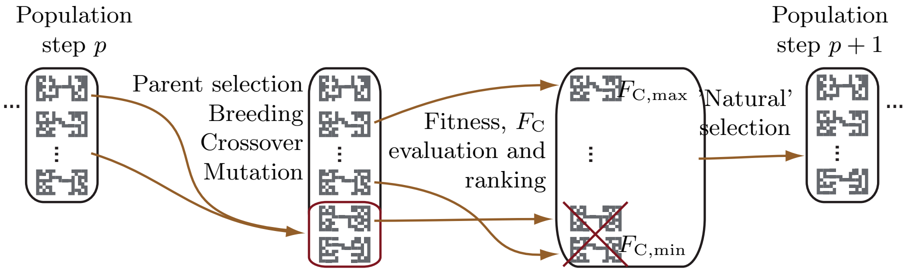

Figure 1: Illustration of a genetic algorithm implementation for antenna optimization.

sely contained in the concepts: "generation", "individual", "population", "gene", "chromosome", "breeding", "offspring", "crossover", "mutation", *etc.* These concepts are used in the context of antenna optimization in the following paragraphs, for a detailed explanation refer to [47].

The GA used in the examples to search realistic structures with performance close to physical limitations is depicted in Fig. 1 [9, 10]. We developed this algorithm starting from the implementation distributed with PB-FDTD [55]. An initial-random, 200-individual antennas are improved according to evolutionary principles in steps. At each step 80 random individuals compete to become one of two breeding parents. The resulting two offsprings are affected by two-point cross-over (which happens 80 % of the time) and single-gene mutation (with 20 % probability). These offsprings are placed in the population, doubling its size. Antennas of the expanded population are ranked according to their fitness. The two least-fit antennas are removed from the population. Fitness is evaluated as an objective (cost) function that is minimized during optimization. This function is a combination of antenna parameters with different weights. After 300 consecutive steps without population improvement the algorithm enters a phase where the offspring produced always have up to 4 genes mutated. This phase is meant to reduce the solution time of the GA (however, this time improvement has not been studied). Once improvement is observed, the algorithm returns to "natural" conditions, single-gene mutation with 20 % probability. The optimization is stopped after $2\ 10^5$ steps or when genetic stability during $2\ 10^4$ steps is observed.

As an example consider the over-simplified structure of Fig. 2a as a starting point for antenna optimization using GA/MoM [36, 47]. The problem in this example can be formulated as (item 1, Table 1):
"Optimized antennas made of thin perfect electric conductor (PEC). A possible optimal candidate is obtained by placing up to 6 rectangular patches (shaded) in the mesh (black solid lines) of Fig. 2a. The mesh assures electrical connection between patches at their edges."
Based on this summarized description the GA/MoM can be set up. The six patches (mesh elements in MoM) are the binary genes describing an antenna "population." "Individuals" (antennas) have a genotype made of a single chro-

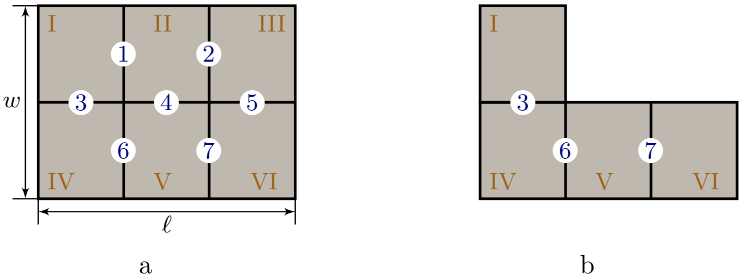

Figure 2: Illustration of a mother structure (a) and an individual derived from it (b). Gray-shaded rectangles—PEC mesh elements/patches. Solid, black lines—mesh edges (they connect patches electrically). Mesh elements are numbered using roman numerals. Mesh edges interior to basis functions domain of definition are numbered with arabic numerals, *i.e.* there is a surface current perpedicularly across each of these numbered edges corresponding to a basis function.

mosome with information about all six genes. The chromosomes are encoded as a 1×6 matrix where 1 denotes a patch placed in the mesh and 0 an empty space in the mesh. Fig. 2b depicts an antenna with 4 patches placed in the mesh as described by the matrix $(1, 0, 0, 1, 1, 1)$.

The interaction between GA and MoM appears during population evolution when the fitness of each individual is evaluated and ranked. This interaction is the method to obtain the MoM solution, (2.2), for each individual in the population. We use a method in which the solution is obtained using matrix operations such that computationally intensive calculations, *e.g.* integration of a Green's function, are not performed unnecessarily. The "mother" matrices needed for these matrix operations, obtained at item 2, Table 1, are the 7×7 matrices $\mathbf{Z}_{\mathrm{M}} = \mathbf{R}_{\mathrm{r,M}} + \mathrm{j}(\mathbf{X}_{\mathrm{m,M}} - \mathbf{X}_{\mathrm{e,M}})$ and the 7×1 matrix $\mathbf{F}_{\mathrm{M}}$, introduced in Sec. 2. The subscript "$_{\mathrm{M}}$" stands for "mother." The matrix size is given by the number of edge elements (basis functions) in the problem definition (Fig. 2). Note that a feed model and position is not necessary for the computation of mother matrices, *i.e.* $\mathbf{Z}_{\mathrm{M}}$, $\mathbf{R}_{\mathrm{r,M}}$, $\mathbf{X}_{\mathrm{m,M}}$, $\mathbf{X}_{\mathrm{e,M}}$ and $\mathbf{F}_{\mathrm{M}}$ depend on geometry alone and are linked with electromagnetics through η_0 and k. Mother matrices are pre-computed and then passed to the GA as parameters; *i.e.* the integration of Green's functions is performed once outside the main evolutionary algorithm.

The electromagnetic solution is obtained during the iterative evolutionary part of the GA using the MoM equation (2.2). The solution we look for is the column-matrix $\mathbf{I}$ of complex surface-current coefficients. All matrices involved in the equations mentioned above have sizes that depend on the "individual" (antenna) for which the solution is derived. In the example of Fig. 2 the mother impedance matrix is

$$\mathbf{Z}_\mathrm{M} = \begin{pmatrix} z_{11} & z_{12} & z_{13} & z_{14} & z_{15} & z_{16} & z_{17} \\ z_{21} & z_{22} & z_{23} & z_{24} & z_{25} & z_{26} & z_{27} \\ z_{31} & z_{32} & z_{33} & z_{34} & z_{35} & z_{36} & z_{37} \\ z_{41} & z_{42} & z_{43} & z_{44} & z_{45} & z_{46} & z_{47} \\ z_{51} & z_{52} & z_{53} & z_{54} & z_{55} & z_{56} & z_{57} \\ z_{61} & z_{62} & z_{63} & z_{64} & z_{65} & z_{66} & z_{67} \\ z_{71} & z_{72} & z_{73} & z_{74} & z_{75} & z_{76} & z_{77} \end{pmatrix}, \tag{3.1}$$

where rows and columns with indexes 3, 6 and 7 are colored. These indexes result when translating the genetic information of the antenna in Fig. 2b to MoM basis functions. These functions and their interaction with each other are already contained in the mother matrix $\mathbf{Z}_\mathrm{M}$ such that extracting the elements at the intersections of rows 3, 6, and 7 with columns 3, 6, and 7 gives the impedance matrix describing the individual antenna in Fig. 2b, *i.e.*

$$\mathbf{Z}_\mathrm{I} = \begin{pmatrix} z_{33} & z_{36} & z_{37} \\ z_{63} & z_{66} & z_{67} \\ z_{73} & z_{76} & z_{77} \end{pmatrix}, \tag{3.2}$$

where the subscript $_\mathrm{I}$ stands for "individual" in an antenna population. The feed model must be defined in the column matrix $\mathbf{V}$ now, when calculating the MoM solution. Considering, for example, that we may only feed a unitary voltage gap model across the edges of basis functions 1 and 6, we can define a "mother" feed matrix as

$$\mathbf{V}_\mathrm{M} = \begin{pmatrix} 1 & 0 & 0 & 0 & 0 & 1 & 0 \end{pmatrix}^\mathrm{T}. \tag{3.3}$$

The excitation matrix for the antenna in Fig. 2b is found with the same set of indexes as the impedance matrix, *i.e.*

$$\mathbf{V}_\mathrm{I} \;\; = \begin{pmatrix} & & 0 & & & 1 & 0 \end{pmatrix}^\mathrm{T}. \tag{3.4}$$

The MoM solution for the individual antenna is

$$\mathbf{I}_\mathrm{I} = \mathbf{Z}_\mathrm{I}^{-1}\mathbf{V}_\mathrm{I} = \begin{pmatrix} z_{33} & z_{36} & z_{37} \\ z_{63} & z_{66} & z_{67} \\ z_{73} & z_{76} & z_{77} \end{pmatrix}^{-1} \begin{pmatrix} 0 \\ 1 \\ 0 \end{pmatrix}. \tag{3.5}$$

The same indexes are used to extract individual matrices to compute stored energies or far-fields, *e.g.* using equations (2.6) or (2.30) where all matrices are replaced with individual matrices, including $\mathbf{I}_\mathrm{I}$ calculated above.

A GA is neither an exhaustive search of the optimum solution nor an exhaustive evaluation of the characteristics of certain individuals. Such an algorithm uses genetic principles to drive an initially random population toward a suboptimal solution avoiding to some extent local extrema, [47]. Genetic principles allow the

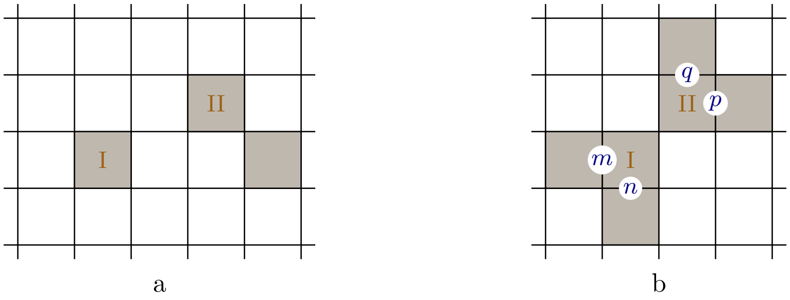

Figure 3: Example of "malformations" (unwanted characteristics) that may appear in GA-optimized antennas: a—isolated mesh elements "I" and "II"; b—corner connection between mesh elements "I" and "II" that are in the domain of definition of basis functions $m, n, p,$ and q. Metallic regions are depicted in gray shading.

appearance of unwanted characteristics of offsprings ("malformations"). Such characteristics may have unpredictable effects on the performance of a fabricated structure, [10, 35, 43, 60]. Two frequent "malformations" are isolated patches and corner connections, Fig. 3. Isolated patches are active mesh elements (*i.e.* included in the genotype of an individual) that do not affect the MoM solution because none of the basis functions is defined on such elements. Isolated elements may have no other neighboring active elements or neighboring elements in the corners. These isolated elements are "purged" after each offspring generation in the GA used here. Corner connections are pairs of active mesh elements that are in the domain of definition of two different basis functions and neighbors through a common corner vertex. Different methods can be used to avoid corner connections such as random geometry refinement, [43], patch overlapping, [35], faulty-gene purging (used here), [10], *etc.*

3.2 Convex Optimization

Fundamental bounds presented in Section 2.3 are computed with the optimization problems (2.26) and (2.27) that are in fact formulated as convex optimization problems. Convex optimization has a well developed theory and can be solved efficiently [3]. Moreover, it gives a posteriori error estimates on the solution. Unlike global optimization methods such as GA, it finds the optimal solution; as the local optimum is also the global optimum.

Fundamental bounds on the G/Q quotient for an antenna, (2.26), can be computed with any convex optimization software package. One example Matlab library is CVX [17]. The optimization problem (2.26) can be easily written as a CVX model in Matlab [23]. If the fundamental bounds on the whole structure are of interest the mother matrices (item 2, Table 1) are used directly as inputs of the Matlab CVX model. In the case of embedded antennas, where only part

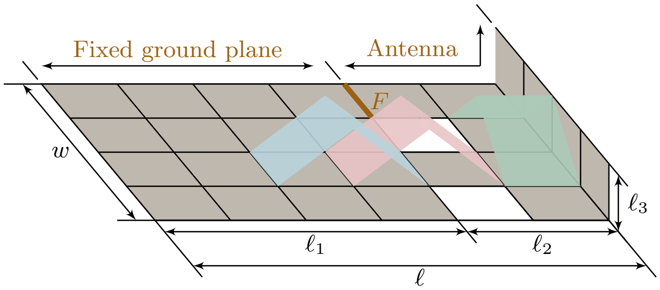

Figure 4: Illustration of rectangular mesh element discretization and "rooftop" basis function amplitude for a three-dimensional radiating structure. Metal areas are depicted in gray shading. The amplitudes of three of the total $7 \times 3 + 6 \times 4 - 4 - 3$ basis functions are depicted in blue, pink and green shading. The feeding edge is marked F.

of the structure should have the controlled currents, a constraint can be added to the optimization problem [21, 23]. Once the optimization problem is solved the optimal currents that give the maximum G/Q quotient, the fundamental bounds on G/Q, are found. If the dual problem (2.27) is solved with a similar approach another set of optimal currents giving the same bound are found.

4 Examples

Combining GA antenna optimization with the fundamental bounds results in a powerful tool to synthesize small antennas. The first two examples illustrate this by finding the optimum antenna for a simplified wireless terminal chassis. The last example demonstrates optimal antenna placement on a wireless terminal. In all examples the wireless terminal chassis is divided into separate parts; the ground plane and, the radiating antenna. The ground plane is kept fixed while the optimization is done on the antenna part. The wireless terminal is a modeled as an infinitely-thin PEC in vacuum.

4.1 Bent-End Simple Phone Model

The analyzed structures are spatially confined to three rectangular regions connected together as illustrated in Fig. 4. The first region has the length ℓ_1 and width $w = 7\,\text{cm}$. This region is the fixed ground plane, [9, 10]. The second and third rectangular regions, with the lengths ℓ_2 and $\ell_3 = 0.7\,\text{cm}$, respectively, and width w, represent the antenna region, [9, 10]. The lengths ℓ_1 and ℓ_2 are chosen such that $\ell_1 + \ell_2 = \ell = 14\,\text{cm}$. The region with the length ℓ_3 extends in a direction perpendicular to the common plane of the other two regions.

Three cases of the above arrangement are considered. The structures corresponding to these cases have $\ell_2 = 0.7\,\text{cm}$, $1.4\,\text{cm}$ and $2.8\,\text{cm}$, *i.e.* $5\,\%$, $10\,\%$ and

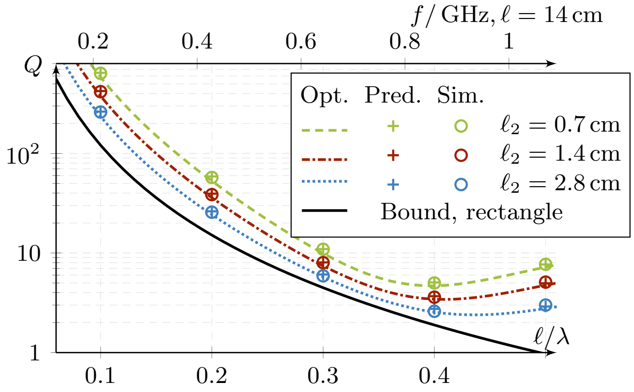

Figure 5: The Q-factors of antennas optimized using a genetic algorithm ("+") compared to corresponding Q-factors of G/Q-optimum current densities, [21] (dashed, dash-dotted, and dotted lines), for the bent-end model illustrated in Fig. 4 with $\ell_2 = 0.7$ cm, 1.4 cm and 2.8 cm and $\ell = 14$ cm. The input impedance of the GA-optimized structures, computed by ESI-CEM, [12], has been used to calculate the Q-factors "∘" using a resonance model [20, 59, 61]. The physical bound on Q for a rectangular PEC surface $14 \times 7\,\mathrm{cm}^2$, [22], is depicted in solid black line.

20 % of ℓ, respectively. To reiterate the whole procedure; the antenna region is used for current optimization, to derive physical limitations (item 4, Table 1), and for genetic optimization, to synthesize antennas close to their physical limitations (item 3, Table 1). Physical limitations are derived using convex optimization formulation (2.27) for the G/Q-ratio in each situation, [21]. Antennas are optimized for minimum Q through the GA/MoM optimization procedure, [36, 47], see Sec. 3.

The mother structure, [36, 47], corresponding to the arrangement described above consists of three infinitely thin PEC rectangular surfaces with the lengths ℓ_1, ℓ_2 and ℓ_3, and width w arranged as in Fig. 4. This structure is discretized with a non-uniform mesh, finer in the antenna region than in the ground plane for all cases considered. The first 11.2 cm in the ℓ-direction from the left in Fig. 4 are divided in 40 mesh elements (and 25 in the w-direction). The remaining 2.8 cm in the ℓ-direction are divided in 20 mesh elements (and 50 in the w-direction). The bent region is divided in 5 by 50 mesh elements in the ℓ_3 and w directions, respectively. This particular choice of discretization results in square mesh elements with the side 1.4 mm in the antenna region and 2.8 mm in the ground plane. A row of overlapping basis functions in the ℓ-direction at the place of the discontinuity in the mesh size couples electrically the regions with different discretizations.

The mother matrices, *i.e.* the matrices $\mathbf{Z}$, $\mathbf{X}_\mathrm{e}$, *etc.*, describing the mother structure, are square with 4435 rows (item 2, Table 1). A block matrix de-

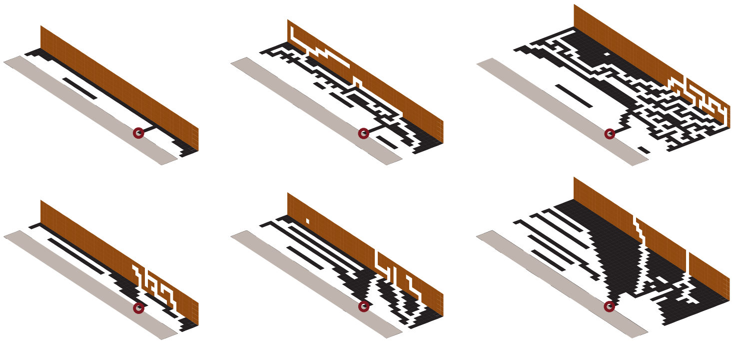

Figure 6: Example of GA optimized structures with Q-factors depicted in Fig. 5 for $\ell/\lambda = 0.1$ (top row) and $\ell/\lambda = 0.5$ (bottom row), and $\ell_2 = 0.7\,\mathrm{cm}$ (left column), $1.4\,\mathrm{cm}$ (middle column), and $2.8\,\mathrm{cm}$ (left column). Gray shading—part of the ground plane, black—antenna region part coplanar with the ground plane, bronze—antenna region part normal to the ground plane. Feeding edges are circled.

composition is applied to these matrices, [36]. This decomposition reduces the sizes of the matrices manipulated repetitively during the GA/MoM optimization. These latter matrices are square with 990, 1485 and 2475 rows respectively for $\ell_2 = 0.7\,\mathrm{cm}$, $1.4\,\mathrm{cm}$ and $2.8\,\mathrm{cm}$.

The genetic optimization of antenna Q has been run for five frequencies, given by $\ell/\lambda = 0.1,\ 0.2,\ 0.3,\ 0.4,$ and 0.5. Five optimized structures have been generated by the GA for each combination of ℓ_2 and frequency. The smallest optimized-structure Q-factor (2.5) of the five corresponding to each combination of ℓ_2 and frequency is labeled "Pred." in Fig. 5. The optimized structures with these smallest Q-factors (of which six are depicted in Fig. 6) have been simulated using the commercial solver ESI-CEM, [12] (item 5, Table 1). The input impedance of these structures is used to obtain the Q-factors labeled "Sim." in Fig. 5. These Q-factors agree to a large extent with those obtained using the in-house MoM solver and the discrete expressions (2.6)–(2.5) (less than 6 % deviation relative to the former Q values). The single-resonance model described in [20, 61], equation (2.18), is employed to compute the Q-factor for $\ell/\lambda = 0.1$ and 0.2. The Q-factors for the other frequencies are computed using the multiple-resonance, Brune-synthesis model, [18, 59]. The single-frequency $Q_{\mathrm{Z}'_{\mathrm{in}}}$ (2.24) has been applied to the structures having the smallest Q-factors mentioned above. The $Q_{\mathrm{Z}'_{\mathrm{in}}}$ values in these cases have less than 5 % difference relative to corresponding $Q_{\mathrm{Z}'_{\mathrm{in}}}$ values computed using (2.18).

The Q-factors obtained in optimization and simulation are compared to Q-factors given by optimum antenna current distributions, labeled "Opt." in Fig. 5. These distributions are obtained using the convex optimization formulation (2.27) for the G/Q-quotient, [21]. The matrices involved in these formulations are square with 990, 1485 and 2475 rows respectively for $\ell_2 = 0.7\,\mathrm{cm}$, $1.4\,\mathrm{cm}$ and $2.8\,\mathrm{cm}$.

These matrices are obtained using a uniform, 1.4 mm-side square mesh element discretization of the mother structure—same mother structure as that considered for GA optimization. The physical bound on the Q-factor of a rectangular PEC region with the dimensions $14 \times 7\,\mathrm{cm}^2$, computed using the results in [22], is included for illustration. It is observed in Fig. 5 that the optimized-structure Q-factors are close to those achieved by optimum antenna currents (less than 13 % deviation relative to the optimum-current Q-factors). Note that the current distributions used to compute the curves labeled "Opt." in Fig. 5 are optimum in the sense of G/Q. However, the Q-factors computed from these distributions may not be optimum in the sense of the Q-factor. This may result in structures that are on the "wrong side" of the G/Q-optimum current Q-factor, *e.g.* below the curves in Fig. 5. The G/Q-quotient of such structures is on the "right side" of the physical bound.

4.2 Bent-End Simple Phone Model—Optimization for $Q_{\mathrm{Z}'}$

The bent-end model with $\ell_1 = 12.6\,\mathrm{cm}$ and $\ell_2 = 1.4\,\mathrm{cm}$, described in Sec. 4.1, has been optimized using the GA for operation between 700 MHz and 960 MHz. This frequency band is divided in two sub-bands with the center frequencies $f_{\mathrm{c},1} = 759.5\,\mathrm{MHz}$ and $f_{\mathrm{c},2} = 889.5\,\mathrm{MHz}$, The fractional bandwidths of the two sub-bands are equal, $\mathrm{FBW}_{1,2} \approx 15.8\,\%$. The matrices $\mathbf{Z}$, $\mathbf{X}_{\mathrm{e}}$, $\mathbf{X}_{\mathrm{m}}$ and $\mathbf{R}$ are computed for the center frequencies. Two extra impedance matrices are computed for the frequencies $1.001 f_{\mathrm{c},1,2}$ in order to evaluate $Q_{\mathrm{Z}'_{\mathrm{in}}}$ at $f_{\mathrm{c},1,2}$ using (2.18). The cost function minimized by the GA is

$$\begin{aligned} F_{\mathrm{C}} = \alpha_{\mathrm{Q,M}} \max\left\{\frac{Q_1}{7}, \frac{Q_2}{7}\right\} + \alpha_{\mathrm{Q,S}} \left(\frac{Q_1}{7} + \frac{Q_2}{7}\right) \\ + \alpha_{\mathrm{Q}_{\mathrm{Z}'},\mathrm{M}} \max\left\{Q_{\mathrm{Z}',1}, Q_{\mathrm{Z}',2}\right\} + \alpha_{\mathrm{Q}_{\mathrm{Z}'},\mathrm{S}} \left(Q_{\mathrm{Z}',1} + Q_{\mathrm{Z}',2}\right), \end{aligned} \tag{4.1}$$

where the indexes 1 and 2 denote the sub-band, Q is the energy-based antenna-Q (2.5), $Q_{\mathrm{Z}'_{\mathrm{in}}}$ is the single-resonance input-impedance-derivative antenna-Q (2.18), and the weights α define the optimization target. The normalization values for Q, 7, ensure less than $-6\,\mathrm{dB}$ reflection coefficient magnitude at the antenna input for the targeted FBW, under the assumption of single-resonance [61]. The

Table 2: GA cost function parameters and results for different optimization objectives

	Target	α_{Q},		$\alpha_{\mathrm{Q}_{\mathrm{Z}'}}$,		Q_1	Q_2	$Q_{\mathrm{Z}',1}$	$Q_{\mathrm{Z}',2}$
		M	S	M	S				
1	min Q	1	0.1	0	0	4.6	3.7	2.9	0.3
2	min $Q_{\mathrm{Z}'_{\mathrm{in}}}$	0	0	1	0.1	8.2	8.9	0.01	0.01
3	min Q & $Q_{\mathrm{Z}'_{\mathrm{in}}}$	1	0.1	1	0.1	8.7	6.8	0.08	0.08
4						6.5	5.5	1.1	1.1

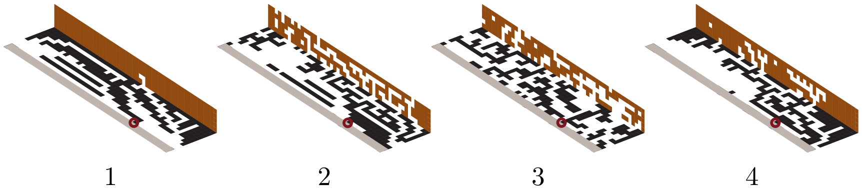

Figure 7: GA-optimized structures whose Q-factors are listed in Table 2. Gray shading—part of the ground plane, black—antenna region part coplanar with the ground plane, bronze—antenna region part normal to the ground plane. Feeding edges are circled.

$Q_{Z'_{\text{in}}}$ values are not normalized because some applications target as low $Q_{Z'_{\text{in}}}$ as possible, *i.e.* little variation of the input impedance in the operation band.

The GA has been run five times for each optimization target whose α-values are listed in Table 2. The Q-factors of the four GA-optimized structures depicted in Fig. 7 (of the total 15 structures) are presented in the same table. The structures corresponding to rows 1, 2 and 3 have the minimum cost function. The structure whose Q-factors are listed on row 4 has been optimized for simultaneous minimum Q and $Q_{Z'_{\text{in}}}$, does not have the minimum cost function, but has minimum Q on both sub-bands (out of the total 5 GA-optimized structures with this target). The values for $Q_{Z'_{\text{in}}}$ listed in Table 2 are evaluated with (2.18). These values agree to a large extent with the same values reevaluated at the center frequencies with (2.24). The four structures of Fig. 7 have been simulated in ESI-CEM [12]. The magnitudes of the reflection coefficients at the inputs of these structures are depicted in Fig. 8. Matching networks that yield less than -6 dB reflection coefficient in the entire band have been designed using BetaMatch [2]. These networks are depicted in Fig. 9 and the resulting S_{11} magnitudes in Fig. 8. Real component models of surface-mount device (SMD) lumped elements, including losses, have been used for matching. The curves in Fig. 8 offer information about the effort needed to design matching networks for the structures and situation considered.

Table 3: Dimensions of MoM matrices for the structures of Fig. 10

Struct.	a	b	c	d	e, f	g	h	i
N	7584	8256	7568	7584	8256	8256	10830	7584
N_{AR}	1936	2608	1928	1944	2616	2612	5168	1992

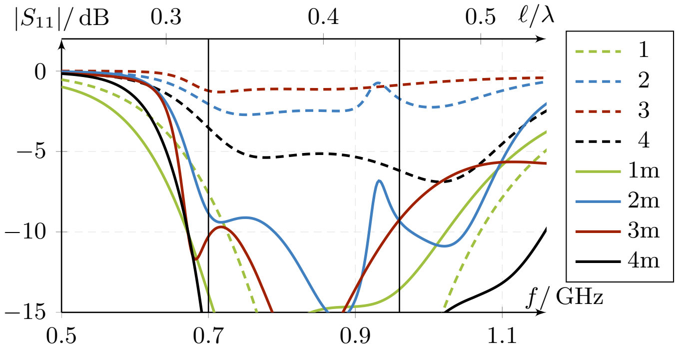

Figure 8: Magnitude of S_{11} at the input of the structures depicted in Fig. 7 without matching network, the curves labeled 1, 2, 3 and 4, and with the matching networks sketched in Fig. 9, the curves labeled 1m, 2m, 3m and 4m.

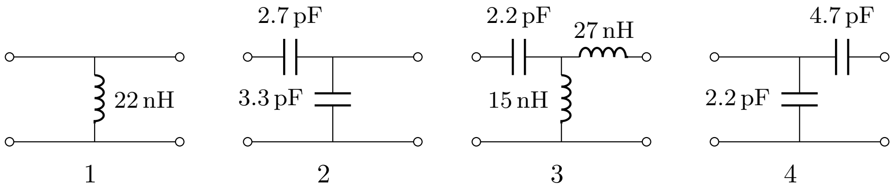

Figure 9: Matching networks designed for the structures depicted in Fig. 7 to yield less than −6 dB reflection coefficient magnitude between 700 . . . 960 MHz (solid curves in Fig. 8).

4.3 Wireless Terminal Antenna Placement Using Optimum Currents

Optimum antenna currents can be employed for evaluation and comparison of the performance achievable by a device with antennas placed at different locations. For illustration, we would like to determine the position and shape of the antenna region, [9, 10], that has the smallest Q-factor in the frequency range of Fig. 5. The nine 3D simplified models of common hand-held wireless terminals depicted in Fig. 10 are analyzed. These models have been chosen based on observations of common hand-held devices. The models are limited to a rectangular parallelepiped with dimensions $\ell \times w \times h = 14 \times 7 \times 0.7\,\mathrm{cm}^3$ (*i.e.* length × width × height). Note that limiting the structures to a parallelepiped is introduced for illustration purpose and does not restrict the applicability of the procedure exemplified here. Each model is drawn in Fig. 10 to scale in three side views from the ℓ, w and h-directions (except for Fig. 10h where an h-side view and two sections through the symmetry planes are depicted). Gray and black represent the ground plane and antenna region, respectively.

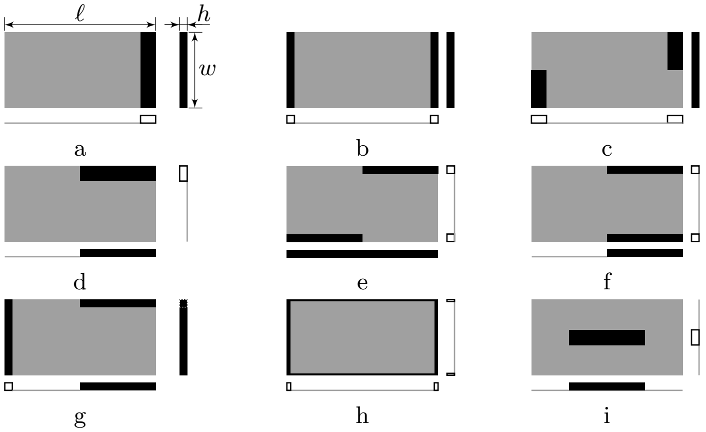

Figure 10: Nine simplified wireless-device models limited to a parallelepiped, consisting of a planar ground region extending 90 % of one length×width face, *i.e.* $\ell \times w$, and an antenna region occupying 10 % of the parallelepiped volume. Three side views are depicted for a-g and i, *i.e.* structures as seen along the length, width and height. A side view along the height and two sections at the symmetry planes are depicted for h. Gray shading—ground plane; black—antenna region, [9, 10].

The ground plane, [9, 10] covers 90 % of the area of one $\ell \times w$ face of the parallelepiped bounding the antenna. The remaining 10 % of that face represents the support of the antenna region, which may be continuous or divided in more sub-regions. Here, a maximum of two sub-regions have been used. The structures in the antenna regions are limited to infinitely thin PEC sheets placed on faces of the 3D shape of the antenna region. This shape is obtained by translating the 10 % of the $\ell \times w$-face area reserved for the antenna region a distance h perpendicularly to the ground plane (*i.e.* by extruding the 10 % in the h-direction to the opposed face). The shapes resulting in the antenna region are made of rectangular parallelepipeds. These parallelepipeds are covered with PEC sheets on the four largest-area faces (in the case depicted in Fig. 10h there are four openings adjacent to the ground plane corners in the $w \times h$-plane; these are one mesh-element wide and extend the entire h-dimension).

The antenna region placement cases introduced above are discretized using a uniform mesh of $1.75 \times 1.75\,\mathrm{mm}^2$ rectangular elements. The total number of basis functions, N, resulting for the structures depicted in Fig. 10 are presented in Table 3 (*i.e.* the number of rows and columns, where applicable, of $\mathbf{Z}$, $\mathbf{Z}'$, $\mathbf{X}_{\mathrm{e}}$, $\mathbf{X}_{\mathrm{m}}$, $\mathbf{R}$, and $\mathbf{F}$). The same table presents the number of rows, and columns where applicable, N_{AR}, of the blocks, [36], corresponding to the 10 %-$\ell \times w$-area antenna region [9, 10]. These blocks are computed for the matrices involved in the convex optimization formulation (2.27).

The bounds on G/Q using formulation (2.27) for the simplified models of

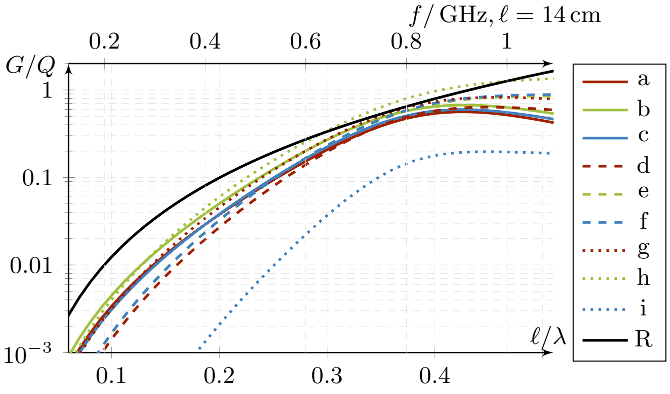

Figure 11: Physical bounds on G/Q for the structures depicted in Fig. 10 obtained using the convex optimization formulation (2.27), [21], when only the antenna region (black in Fig. 10) is optimized. The physical bound on G/Q for a rectangular PEC surface $14 \times 7\,\mathrm{cm}^2$, [22], is depicted in solid black line and labeled "R."

Fig. 10 are depicted in Fig. 11. The formulation has been solved for 46 ℓ/λ-values between 0.06 and 0.51 (frequency between 128 MHz and 1.092 GHz). Linear polarization along the length and directivity in the direction of the height of the parallelepiped bounding the models are considered. The bound computed using the results in [22][1] for a rectangular, infinitely thin, $14 \times 7\,\mathrm{cm}^2$ PEC sheet is labeled "R" in Fig. 11. The G/Q-optimum current distributions giving the physical bounds in Fig. 11 are used to compute the Q-factors (2.5) depicted in Fig. 12. The physical bound on Q for a rectangular $14 \times 7\,\mathrm{cm}^2$ PEC sheet, [22], is labeled "R" in Fig. 12. The ring structure depicted in Fig. 10h outperforms all other structures in the figure in terms of G/Q and Q, except for a frequency region around $\ell/\lambda \approx 0.1$ where the structure in Fig. 10b has a greater G/Q. We also note that around $\ell/\lambda \approx 0.37$ a few of the structures in Fig. 10 reach close to the G/Q bound of a rectangular region and the structure in Fig. 10h has a G/Q value greater than that of a rectangular region. The optimum-current Q-factors do not reach as close to the physical bound on Q for a rectangular region as the G/Q-values.

Note that, in this example, we have done items 1, 2 and 5 in Table 1. The next step would be to run the GA/MoM for the structure in Fig. 10h by assuming a feed location (item 3, Table 1). Further on, GA-optimized structures should be verified using a commercial simulator, item 5, Table 1.

---

[1] http://www.mathworks.se/matlabcentral/fileexchange/26806-antennaq

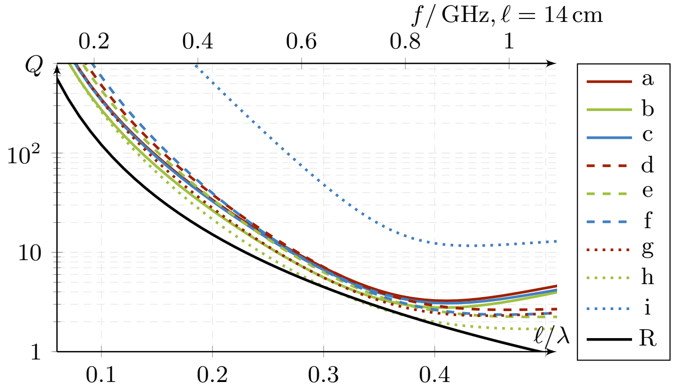

Figure 12: The Q-factors (2.5) achieved by the currents that give the optimum G/Q-values depicted in Fig. 11. The Q-factor of a $14 \times 7\,\mathrm{cm}^2$ PEC rectangle, [22], is labeled "R."

5 Conclusions

This chapter reviewed the use of fundamental bounds and the Q-factor in small antenna optimization. With the fundamental bounds the antenna designer can estimate how well the antenna will perform before the design process. This can provide insight if the design specifications can be met with the structure at hand. Moreover, knowledge of the antennas bounds can be used in a physical limitation-aware optimization, where the optimization process can be terminated once the target is achieved with a certain margin.

Formulating the bounds as a convex optimization problem offers the flexibility to add additional "convex" constraints with minor effort. Examples of additional constraints include, limitations on efficiency, SAR, and the radiation pattern or optimizing the antenna region of embedded antennas. The antenna designer can investigate numerous situations by adding the previous constraints to the original convex problem.

The introduction of a method to estimate $Q_{\mathrm{Z}'_{\mathrm{in}}}$ of antennas from the current distribution computed for a single frequency; the application of fundamental bounds and of the $Q_{\mathrm{Z}'_{\mathrm{in}}}$ single-frequency estimation method to design cases of three-dimensional radiating structures has not been considered previously in the literature. The results suggest that customized physical bounds, optimum currents, and single-frequency expressions, are tools that are useful for antenna design, *e.g.* to stop an optimization process, assess realizability of specifications, assess performance of antenna locations. While the examples in this chapter considered PEC material, the optimization can be extended to antennas consisting of composite materials such as, PEC and dielectrics [25].

References

[1] 145-2013 – IEEE standard for definitions of terms for antennas. pages 1–50, March 2014.

[2] MNW Scan, Singapore—BetaMatch, Software for antenna component matching. http://www.mnw-scan.com/.

[3] S. P. Boyd and L. Vandenberghe. *Convex Optimization.* Cambridge Univ. Pr., 2004.

[4] O. Brune. Synthesis of a finite two-terminal network whose driving-point impedance is a prescribed function of frequency. *MIT J. Math. Phys.*, **10**, 191–236, 1931.

[5] M. Capek, L. Jelinek, P. Hazdra, and J. Eichler. The measurable Q factor and observable energies of radiating structures. *IEEE Trans. Antennas Propag.*, **62**(1), 311–318, Jan 2014.

[6] M. Capek, M. Gustafsson, and K. Schab. Minimization of antenna quality factor. *IEEE Trans. Antennas Propag.*, **65**(8), 4115–4123, 2017.

[7] M. Capek, L. Jelinek, and G. A. E. Vandenbosch. Stored electromagnetic energy and quality factor of radiating structures. *Proc. R. Soc. A*, **472**(2188), 2016.

[8] L. J. Chu. Physical limitations of omni-directional antennas. *J. Appl. Phys.*, **19**, 1163–1175, 1948.

[9] M. Cismasu and M. Gustafsson. Antenna bandwidth optimization with single frequency simulation. *IEEE Trans. Antennas Propag.*, **62**(3), 1304–1311, 2014.

[10] M. Cismasu and M. Gustafsson. Multiband antenna Q optimization using stored energy expressions. *IEEE Antennas Wireless Propag. Lett.*, **13**(2014), 646–649, 2014.

[11] R. E. Collin and S. Rothschild. Evaluation of antenna Q. *IEEE Trans. Antennas Propag.*, **12**, 23–27, January 1964.

[12] ESI Group, Paris, France—ESI Group's computational electromagnetic (CEM) solution. http://www.esi-group.com.

[13] W. Geyi. Physical limitations of antenna. *IEEE Trans. Antennas Propag.*, **51**(8), 2116–2123, August 2003.

[14] W. Geyi. *Foundations of Applied Electrodynamics.* John Wiley & Sons, 2011.

[15] W. C. Gibson. *The Method of Moments in Electromagnetics.* CRC press, 2014.

[16] P. E. Gill, W. Murray, and M. H. Wright. *Practical Optimization.* Academic Press, London, 1981.

[17] M. Grant and S. Boyd. CVX: Matlab software for disciplined convex programming, version 1.21. `http://cvxr.com/cvx`, April 2011.

[18] M. Gustafsson and B. L. G. Jonsson. Antenna Q and stored energy expressed in the fields, currents, and input impedance. *IEEE Trans. Antennas Propag.*, **63**(1), 240–249, 2015.

[19] M. Gustafsson and B. L. G. Jonsson. Stored electromagnetic energy and antenna Q. *Progress In Electromagnetics Research (PIER)*, **150**, 13–27, 2015.

[20] M. Gustafsson and S. Nordebo. Bandwidth, Q-factor, and resonance models of antennas. *Prog. Electromagn. Res.*, **62**, 1–20, 2006.

[21] M. Gustafsson and S. Nordebo. Optimal antenna currents for Q, superdirectivity, and radiation patterns using convex optimization. *IEEE Trans. Antennas Propag.*, **61**(3), 1109–1118, 2013.

[22] M. Gustafsson, C. Sohl, and G. Kristensson. Illustrations of new physical bounds on linearly polarized antennas. *IEEE Trans. Antennas Propag.*, **57**(5), 1319–1327, May 2009.

[23] M. Gustafsson, D. Tayli, C. Ehrenborg, M. Cismasu, and S. Nordebo. Antenna current optimization using MATLAB and CVX. *FERMAT*, **15**(5), 1–29, 2016.

[24] M. Gustafsson, M. Cismasu, and B. L. G. Jonsson. Physical bounds and optimal currents on antennas. *IEEE Trans. Antennas Propag.*, **60**(6), 2672–2681, 2012.

[25] M. Gustafsson and C. Ehrenborg. State-space models and stored electromagnetic energy for antennas in dispersive and heterogeneous media. *Radio Sci.*, **52**, 2017.

[26] M. Gustafsson, D. Tayli, and M. Cismasu. Q factors for antennas in dispersive media. Technical Report LUTEDX/(TEAT-7232)/1–24/(2014), Lund University, Department of Electrical and Information Technology and P.O. Box 118 and S-221 00 Lund, Sweden, 2014. http://www.eit.lth.se.

[27] M. Gustafsson, D. Tayli, and M. Cismasu. *Physical bounds of antennas*, pages 1–32. Springer-Verlag, 2015.

[28] R. F. Harrington. *Time Harmonic Electromagnetic Fields.* McGraw-Hill, New York, NY, 1961.

[29] R. F. Harrington. *Field Computation by Moment Methods.* Macmillan, New York, NY, 1968.

[30] R. L. Haupt and D. H. Werner. *Genetic Algorithms in Electromagnetics.* Wiley-IEEE Press, 2007.

[31] D. Hertog. *Interior Point Approach to Linear, Quadratic and Convex Programming.* Kluwer Academic Publishers, 1994.

[32] R. Horst, P. Pardalos, and N. Van Thoai. *Introduction to Global Optimization.* Nonconvex Optimization and Its Applications. Springer-Verlag, 2000.

[33] L. Jelinek and M. Capek. Optimal currents on arbitrarily shaped surfaces. *IEEE Trans. Antennas Propag.*, **65**(1), 329–341, 2017.

[34] J. M. Jin. *Theory and Computation of Electromagnetic Fields.* Wiley, 2011.

[35] M. John and M. Ammann. Wideband printed monopole design using a genetic algorithm. *Antennas and Wireless Propagation Letters, IEEE*, **6**, 447–449, 2007.

[36] J. M. Johnson and Y. Rahmat-Samii. Genetic algorithms and method of moments GA/MOM for the design of integrated antennas. *IEEE Trans. Antennas Propag.*, **47**(10), 1606–1614, oct 1999.

[37] A. Karlsson. Physical limitations of antennas in a lossy medium. *IEEE Trans. Antennas Propag.*, **52**, 2027–2033, 2004.

[38] M. A. Khayat and D. R. Wilton. Numerical evaluation of singular and near-singular potential integrals. *IEEE Trans. Antennas Propag.*, **53**(10), 3180–3190, October 2005.

[39] L. S. Lasdon. *Optimization Theory for Large Systems.* Dover Books on Mathematics. Dover Publications, 2002.

[40] J. R. Mosig and F. E. Gardiol. A dynamical radiation model for microstrip structures. In P. W. Hawkes, editor, *Advances in Electronics and Electron Physics*, volume 59, pages 139 – 237. Academic Press, 1982.

[41] Y. Nesterov and A. Nemirovsky. *Interior Point Polynomial Methods in Convex Programming*, volume 13. Studies in Applied Mathematics, Society for Industrial and Applied Mathematics, Philadelphia, PA, 1994.

[42] J. Nocedal and S. J. Wright. *Numerical Optimization.* Operations Research and Financial Engineering. Springer-Verlag, New York, NY, 2006.

[43] M. Ohira, H. Deguchi, M. Tsuji, and H. Shigesawa. Multiband single-layer frequency selective surface designed by combination of genetic algorithm and geometry-refinement technique. *IEEE Trans. Antennas Propag.*, **52**(11), 2925–2931, Nov 2004.

[44] A. F. Peterson, S. L. Ray, and R. Mittra. *Computational Methods for Electromagnetics.* IEEE Press, New York, NY, 1998.

[45] D. M. Pozar. Considerations for millimeter wave printed antennas. *IEEE Trans. Antennas Propag.*, **31**(5), 740–747, September 1983.

[46] D. M. Pozar. New results for minimum Q, maximum gain, and polarization properties of electrically small arbitrary antennas. In *Antennas and Propagation, 2009. EuCAP 2009. 3rd European Conference on*, pages 1993–1996, March 2009.

[47] Y. Rahmat-Samii and E. Michielssen. *Electromagnetic Optimization by Genetic Algorithms.* Wiley Series in Microwave and Optical Engineering. John Wiley & Sons, 1999.

[48] A. Rinnooy Kan and G. Timmer. Stochastic global optimization methods part I: Clustering methods. *Mathematical Programming*, **39**(1), 27–56, 1987.

[49] J. Robinson and Y. Rahmat-Samii. Particle swarm optimization in electromagnetics. *IEEE Trans. Antennas Propag.*, **52**(2), 397 – 407, feb. 2004.

[50] K. Schab, L. Jelinek, M. Capek, C. Ehrenborg, D. Tayli, G. Vandenbosch, and M. Gustafsson. Energy stored by radiating systems. Technical Report LUTEDX/(TEAT-7251)/1–32/(2017), Lund University, Department of Electrical and Information Technology, P.O. Box 118, S-221 00 Lund, Sweden, 2017.

[51] M. Shahpari, D. Thiel, and A. Lewis. An investigation into the Gustafsson limit for small planar antennas using optimization. *IEEE Trans. Antennas Propag.*, **62**(2), 950–955, Feb 2014.

[52] J. C.-E. Sten, P. K. Koivisto, and A. Hujanen. Limitations for the radiation Q of a small antenna enclosed in a spheroidal volume: axial polarisation. *AEÜ Int. J. Electron. Commun.*, **55**(3), 198–204, 2001.

[53] D. Tayli and M. Gustafsson. Physical bounds for antennas above a ground plane. *IEEE Antennas Wireless Propag. Lett.*, **15**, 1281–1284, 2016.

[54] H. L. Thal. New radiation Q limits for spherical wire antennas. *IEEE Trans. Antennas Propag.*, **54**(10), 2757–2763, October 2006.

[55] B. Thors, H. Steyskal, and H. Holter. Broad-band fragmented aperture phased array element design using genetic algorithms. *IEEE Trans. Antennas Propag.*, **53**(10), 3280 – 3287, oct. 2005.

[56] G. A. E. Vandenbosch. Reactive energies, impedance, and Q factor of radiating structures. *IEEE Trans. Antennas Propag.*, **58**(4), 1112–1127, 2010.

[57] J. Volakis, C. C. Chen, and K. Fujimoto. *Small Antennas: Miniaturization Techniques & Applications.* McGraw-Hill, New York, NY, 2010.

[58] H. A. Wheeler. Fundamental limitations of small antennas. *Proc. IRE*, **35**(12), 1479–1484, 1947.

[59] O. Wing. *Classical Circuit Theory.* Springer, New York, 2008.

[60] B. G. Xia, J. Meng, D. H. Zhang, and J. S. Zhang. PMM-GA method to synthesize quasi-optical frequency selective surface on SiO2 substrate. *Prog. Electromagn. Res.*, **139**, 599–610, 2013.

[61] A. D. Yaghjian and S. R. Best. Impedance, bandwidth, and Q of antennas. *IEEE Trans. Antennas Propag.*, **53**(4), 1298–1324, 2005.

Accurate and Efficient Evaluation of Characteristic Modes

Paper III

Doruk Tayli, Miloslav Capek, Lamyae Akrou, Vit Losenicky,
Lukas Jelinek, and Mats Gustafsson

Submitted: D. Tayli, M. Capek, L. Akrou, V. Losenicky, L. Jelinek, and M. Gustafsson, "Accurate and Efficient Evaluation of Characteristic Modes", *IEEE Transactions on Antennas and Propagation*, 2017.

Abstract

A new method to improve the accuracy of characteristic mode (CM) decomposition for perfectly conducting bodies is presented. The method uses the expansion of the Green dyadic in spherical vector waves. This expansion is utilized in the method of moments (MoM) solution of the electric field integral equation (EFIE) to improve the numerical range of the real part of the impedance matrix, **R**, that determines the number of obtainable modes from CM decomposition. Computation speed of the **R** matrix and CMs are improved. The method can easily be integrated in existing MoM solvers. Several structures are investigated illustrating the improved accuracy and performance of the new method.

1 Introduction

The method of moments (MoM) solution to electromagnetic field integral equations was introduced by Harrington [22] and has prevailed as a standard in solving open (radiating) electromagnetic problems [38]. While memory-demanding, MoM represents operators as matrices (notably the impedance matrix [22]) allowing for direct inversion and modal decompositions [18]. The latter option is becoming increasingly popular, mainly due to characteristic mode (CM) decomposition [25], a leading formalism in antenna shape and feeding synthesis [7, 45], determination of optimal currents [8, 19], and performance evaluation [41].

Utilization of CMs decomposition is especially efficient when dealing with electrically small antennas [11], particularly if they are made solely of perfect electric conductor (PEC), for which only a small number of modes are needed to describe their radiation behavior. Yet, decompositions involving the real part of impedance matrix are known [9, 25] to be ill conditioned for electrically small structures, since only a few modes radiate well, while the rest is numerical noise [9]. This drawback affects the performance of CMs decomposition and prohibits the superposition of modes [7].

The aforementioned deficiency is resolved in this paper by a two-step procedure. First, the real part of the impedance matrix is constructed using spherical wave expansion of the dyadic Green function [30]. This makes it possible to decompose the real part of the impedance matrix as a product of a spherical modes projection matrix with its hermitian conjugate. The second step consists of reformulating the modal decomposition so that only the stand alone spherical modes projection matrix is involved. This avoids the loss of attainable numerical dynamics during the matrix multiplication process.

The proposed implementation doubles the numerical accuracy with respect to the used arithmetic precision in computing, significantly increasing the number of correctly found modes. For example, the proposed procedure yields more than 280 modes versus 70 modes reported in [9] on a spherical shell (at given electrical size). The improvement in correctly found modes is also accompanied by an additional computation speed. Moreover, the projection on spherical waves in the proposed method introduces several appealing properties. First is an easy monitoring of the numerical dynamics, since the different spherical waves (of different numerical dynamics) occupy separate rows in the projection matrix. Second is the ability to control the spectrum of impedance matrix which plays important role in an optimal design [19].

The paper is organized as follows. The construction of the impedance matrix using classical procedure is briefly reviewed in Section 2.1 and the proposed procedure is presented in Section 2.2. Numerical aspects of evaluating the impedance matrix are discussed in Section 2.3. In Section 3, the spherical modes projection matrix is utilized to reformulate modal decomposition techniques, namely the evaluation of radiation modes in Section 3.1 and CMs in Section 3.2. These two applications cover both the standard and generalized eigenvalue problems. The advantages of the proposed procedure are demonstrated on a series of practical examples in this section. Various aspects of the proposed method are discussed in Section 4 and the paper is concluded in Section 5.

2 Evaluation of Impedance Matrix

This paper investigates mode decompositions for PEC structures in free space. The time-harmonic quantities under the convention $\boldsymbol{\mathcal{J}}(\boldsymbol{r},t) = \mathrm{Re}\left\{\boldsymbol{J}(\boldsymbol{r},\omega)\exp(\mathrm{j}\omega t)\right\}$, with ω being the angular frequency, are used throughout the paper.

2.1 Method of Moments Implementation of the EFIE

Let us consider the electric field integral equation (EFIE) [22] for PEC bodies, defined as

$$\mathcal{Z}(\boldsymbol{J}) = \mathcal{R}(\boldsymbol{J}) + \mathrm{j}\mathcal{X}(\boldsymbol{J}) = \hat{\boldsymbol{n}} \times (\hat{\boldsymbol{n}} \times \boldsymbol{E}), \tag{2.1}$$

with $\mathcal{Z}(\boldsymbol{J})$ being the impedance operator, $\boldsymbol{E}$ the incident electric field [23], $\boldsymbol{J}$ the current density, j the imaginary unit, and $\hat{\boldsymbol{n}}$ the unit normal vector to the PEC surface. The EFIE (2.1) is explicitly written as

$$\hat{\boldsymbol{n}} \times \boldsymbol{E}(\boldsymbol{r}_2) = \mathrm{j}kZ_0\hat{\boldsymbol{n}} \times \int_\Omega \mathbf{G}(\boldsymbol{r}_1,\boldsymbol{r}_2) \cdot \boldsymbol{J}(\boldsymbol{r}_1)\,\mathrm{d}S_1, \tag{2.2}$$

where $\boldsymbol{r}_2 \in \Omega$, k is the wave number, Z_0 the free space impedance, and $\mathbf{G}$ the dyadic Green function for the electric field in free-space defined as [12, 30]

$$\mathbf{G}(\boldsymbol{r}_1,\boldsymbol{r}_2) = \left(\mathbf{1} + \frac{1}{k^2}\nabla\nabla\right)\frac{\mathrm{e}^{-\mathrm{j}k|\boldsymbol{r}_1-\boldsymbol{r}_2|}}{4\pi|\boldsymbol{r}_1-\boldsymbol{r}_2|}. \tag{2.3}$$

Here, $\mathbf{1}$ is the identity dyadic, and $\boldsymbol{r}_1$, $\boldsymbol{r}_2$ are the source and observation points. The EFIE (2.2) is solved with the MoM by expanding the current density $\boldsymbol{J}(\boldsymbol{r})$

into real-valued basis functions $\{\boldsymbol{\psi}_p(\boldsymbol{r})\}$ as

$$\boldsymbol{J}(\boldsymbol{r}) \approx \sum_{p=1}^{N_\psi} I_p \boldsymbol{\psi}_p(\boldsymbol{r}) \tag{2.4}$$

and applying Galerkin testing procedure [12,17]. The impedance operator $\mathcal{Z}(\boldsymbol{J})$ is expressed as the impedance matrix $\mathbf{Z} = \mathbf{R} + \mathrm{j}\mathbf{X} = [Z_{pq}] \in \mathbb{C}^{N_\psi \times N_\psi}$, where $\mathbf{R}$ is the resistance matrix, and $\mathbf{X}$ the reactance matrix. The elements of the impedance matrix are

$$Z_{pq} = \mathrm{j}kZ_0 \int_\Omega \int_\Omega \boldsymbol{\psi}_p(\boldsymbol{r}_1) \cdot \mathbf{G}(\boldsymbol{r}_1, \boldsymbol{r}_2) \cdot \boldsymbol{\psi}_q(\boldsymbol{r}_2) \, \mathrm{d}S_1 \, \mathrm{d}S_2. \tag{2.5}$$

2.2 Spherical Wave Expansion of the Green Dyadic

The impedance matrix $\mathbf{Z}$ can alternatively be computed by expanding the Green dyadic (2.3), in the real-valued spherical vector waves

$$\mathbf{G}(\boldsymbol{r}_1, \boldsymbol{r}_2) = -\mathrm{j}k \sum_\alpha \mathbf{u}_\alpha^{(1)}(k\boldsymbol{r}_<) \, \mathbf{u}_\alpha^{(4)}(k\boldsymbol{r}_>) \tag{2.6}$$

where $\boldsymbol{r}_< = \boldsymbol{r}_1$ and $\boldsymbol{r}_> = \boldsymbol{r}_2$ if $|\boldsymbol{r}_1| < |\boldsymbol{r}_2|$, and $\boldsymbol{r}_< = \boldsymbol{r}_2$ and $\boldsymbol{r}_> = \boldsymbol{r}_1$ if $|\boldsymbol{r}_1| > |\boldsymbol{r}_2|$. The regular and outgoing spherical vector waves [21,30,31,42] are $\mathbf{u}_\alpha^{(1)}(k\boldsymbol{r}_<)$ and $\mathbf{u}_\alpha^{(4)}(k\boldsymbol{r}_>)$, see Appendix B. The mode index α for real-valued spherical vector waves is [20, 21]

$$\alpha(\tau, \sigma, m, l) = 2\left(l^2 + l - 1 + (-1)^s m\right) + \tau \tag{2.7}$$

with $\tau \in \{1, 2\}$, $m \in \{0, \dots, l\}$, $l \in \{1, \dots, L\}$, $s = 0$ for even azimuth functions ($\sigma = \mathrm{e}$), and $s = 1$ for odd azimuth functions ($\sigma = \mathrm{o}$). Inserting the spherical vector waves expansion of the Green dyadic (2.6) into (2.5), the impedance matrix $\mathbf{Z}$ becomes

$$Z_{pq} = k^2 Z_0 \sum_\alpha \int_\Omega \int_\Omega \boldsymbol{\psi}_p(\boldsymbol{r}_1) \cdot \mathbf{u}_\alpha^{(1)}(k\boldsymbol{r}_<) \, \mathbf{u}_\alpha^{(4)}(k\boldsymbol{r}_>) \cdot \boldsymbol{\psi}_q(\boldsymbol{r}_2) \, \mathrm{d}S_1 \, \mathrm{d}S_2. \tag{2.8}$$

For a PEC structure the resistive part of (2.8) can be factorized as

$$R_{pq} = k^2 Z_0 \sum_\alpha \int_\Omega \boldsymbol{\psi}_p(\boldsymbol{r}_1) \cdot \mathbf{u}_\alpha^{(1)}(k\boldsymbol{r}_1) \, \mathrm{d}S_1 \int_\Omega \mathbf{u}_\alpha^{(1)}(k\boldsymbol{r}_2) \cdot \boldsymbol{\psi}_q(\boldsymbol{r}_2) \, \mathrm{d}S_2 \tag{2.9}$$

where $\mathbf{u}_\alpha^{(1)}(k\boldsymbol{r}) = \mathrm{Re}\{\mathbf{u}_\alpha^{(4)}(k\boldsymbol{r})\}$. Reactance matrix, $\mathbf{X}$, cannot be factorized in a similar way as two separate spherical waves occur.

Resistance matrix can be written in matrix form as

$$\mathbf{R} = \mathbf{S}^{\mathrm{T}} \mathbf{S}, \tag{2.10}$$

where $^{\mathrm{T}}$ is the matrix transpose. Individual elements of the matrix $\mathbf{S}$ are

$$S_{\alpha p} = k\sqrt{Z_0}\int_{\Omega}\boldsymbol{\psi}_p\left(\boldsymbol{r}\right)\cdot\mathbf{u}_{\alpha}^{(1)}\left(k\boldsymbol{r}\right)\,\mathrm{d}S \tag{2.11}$$

and the size of the matrix $\mathbf{S}$ is $N_{\alpha}\times N_{\psi}$, where

$$N_{\alpha} = 2L\left(L+2\right) \tag{2.12}$$

is the number of spherical modes and L the highest order of spherical mode, see Appendix B. For complex-valued spherical vector waves [21] the transpose $^{\mathrm{T}}$ in (2.10) is replaced with the hermitian transpose $^{\mathrm{H}}$. The individual integrals in (2.8) are in fact related to the T-matrix method [42, 43], where the incident and scattered electric fields are expanded using regular and outgoing spherical vector waves, respectively.

The radiated far-field $\boldsymbol{F}\left(\hat{\boldsymbol{r}}\right)$ can conveniently be computed using spherical vector harmonics, and the matrix $\mathbf{S}$ as

$$\boldsymbol{F}\left(\hat{\boldsymbol{r}}\right) = \frac{1}{k}\sum_{\alpha}\mathrm{j}^{l-\tau+2}f_{\alpha}\mathbf{Y}_{\alpha}\left(\hat{\boldsymbol{r}}\right), \tag{2.13}$$

where $\mathbf{Y}_{\alpha}\left(\hat{\boldsymbol{r}}\right)$ are the real-valued spherical vector harmonics, see Appendix B, and the expansion coefficients f_{α} are given by

$$\left[f_{\alpha}\right] = \mathbf{SI}, \tag{2.14}$$

where the column matrix $\mathbf{I}$ contains the current density coefficients I_p. The total time-averaged radiated power of a lossless antenna can be expressed as a sum of expansion coefficients

$$P_{\mathrm{r}} \approx \frac{1}{2}\mathbf{I}^{\mathrm{H}}\mathbf{RI} = \frac{1}{2}|\mathbf{SI}|^2 = \frac{1}{2}\sum_{\alpha}|f_{\alpha}|^2. \tag{2.15}$$

2.3 Numerical Considerations

The spectrum of the matrices $\mathbf{R}$ and $\mathbf{X}$ differ considerably [9,19]. The eigenvalues of the $\mathbf{R}$ matrix decrease exponentially and are limited by numerical noise, while this is not the case for the matrix $\mathbf{X}$. As a result, if the matrix $\mathbf{R}$ is used, only a few modes can be extracted. This major limitation can be overcome with the use of the matrix $\mathbf{S}$ in (2.11), whose elements vary several order of magnitude, as the result of the increased order of spherical modes with increasing row number. If the matrix $\mathbf{R}$ is directly computed with the matrix product (2.10) or equivalently from matrix produced by (2.5) small values are truncated due to floating-point arithmetic[1] [6, 46]. Subsequently, the spectrum of the matrix $\mathbf{R}$ should be found by preserving the numerical range of the matrix $\mathbf{S}$ as presented in Section 3.

---

[1] As an example to the loss of significance in double precision arithmetic consider the sum $1.0 + 1\times 10^{-30} = 1.0$.

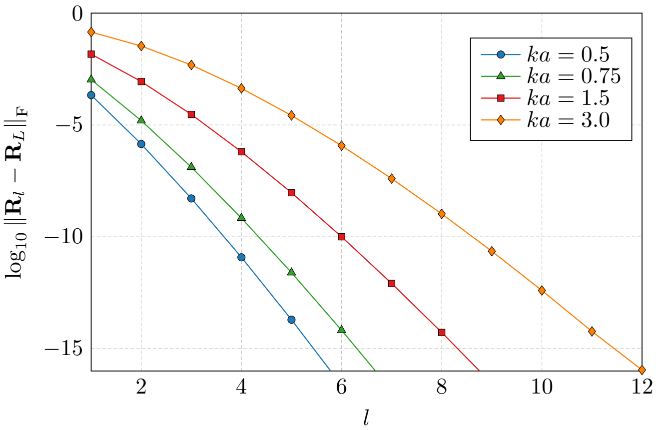

Figure 1: Convergence of the matrix $\mathbf{R}_l = \mathbf{S}_l^\mathrm{T}\mathbf{S}_l$ to the matrix $\mathbf{R}_L = \mathbf{S}_L^\mathrm{T}\mathbf{S}_L$ on the rectangular plate (Example #5) for different order of spherical modes $l = \{1, \ldots, L\}$ and multiple electric sizes $ka \in \{0.5, 0.75, 1.5, 3.0\}$, with the highest spherical mode order $L = 12$. The superscript $^\mathrm{F}$ denotes the Frobenius norm. The convergence is computed with quadruple precision using the mpmath Python library [29].

The matrix **S** also provides a low-rank matrix approximation of the matrix **R**. This is the result of the quick convergence of regular spherical waves where usually $L_\mathrm{max} \approx ka + C$ order of modes is required, a being the radius of the sphere enclosing the scatterer and C a small number typically 10 [21]. Fig. 1 shows the convergence of the matrix **R** for Example #5.

Substitution of the spherical vector waves, introduced in Section 2.2, separates (2.5) into two separate surface integrals reducing computational complexity. Table 1 presents computation times[2] of different matrices[3] **Z**, **R**, **S**, and $\mathbf{S}^\mathrm{T}\mathbf{S}$ for the examples given in Table 2. As expected, the matrix **Z** requires the most computational resources, as it includes both the matrix **R** and **X**. The computation of the matrix **R** using MoM is faster than the matrix **Z** since the underlying integrals are regular. The computation of the matrix **R** using (2.10) is the quickest for most of the examples. The computational gain is notable for structures with more degrees-of-freedom (d-o-f), N_ψ.

3 Modal Decomposition with the Matrix S

Modal decomposition using the matrix **S** is applied to two structures; a spherical shell of radius a (Fig. 2), and a rectangular plate of length L and width $W = L/2$

---

[2] Computations are done on a workstation with i7-3770 CPU @ 3.4 GHz and 32 GB RAM, operating under Windows 7.

[3] Computation time for the **X** matrix is omitted as it takes longer than the **R** matrix, due to Green function singularity.

Example	Time to assemble matrices in IDA (s)			
(see Table 2)	$\mathbf{Z}$	$\mathbf{R}$	$\mathbf{S}$	$\mathbf{R}=\mathbf{S}^{\mathrm{T}}\mathbf{S}$
#1	2.62	0.09	0.036	0.045
#3	14.12	1.77	0.149	0.315
#5	2.34	0.07	0.019	0.024
#6	11.10	1.11	0.072	0.136

Table 1: Time to assemble matrices in IDA. Simulation setup for the examples are in Table 2, $N_q = 4$, matrix multiplication $\mathbf{S}^{\mathrm{T}}\mathbf{S}$ is performed with dgemm from the Intel MKL library [26].

Structure	Example	ka	N_ψ	N_α
Spherical shell (see Fig. 2)	#1	1/2	750	880
	#2	3/2	750	880
	#3	1/2	3330	880
Rectangular plate (see Fig. 3) ($L/W = 2$)	#4	1/2	199	510
	#5	1/2	655	510
	#6	1/2	2657	1920

Table 2: Summary of examples used throughout the paper, ka is the electrical size, N_ψ is the number of basis functions (2.4), and N_α is number of spherical modes calculated as (2.12). The order of the symmetric quadrature rule used to compute the non-singular integrals in (2.5) is $N_q = 3$ [14].

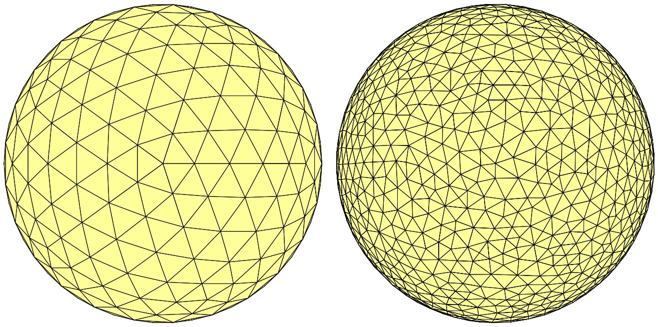

Figure 2: Spherical shell mesh with 500 triangles (left) and 2220 triangles (right) with 750 (left) and 3330 (right) RWG basis functions, respectively. The same mesh grids are used in [9] to make the results comparable.

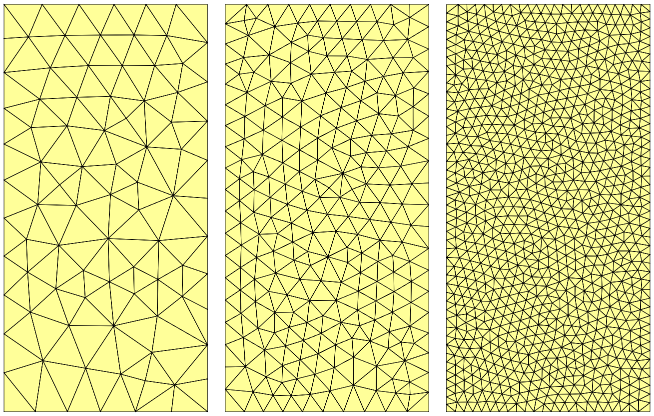

Figure 3: Rectangular plate mesh with 144, 456, and 1818 triangles (from left to right) with 199, 655, and 2657 RWG basis functions, respectively.

(Fig. 3), presented in Table 2. Both structures are investigated for different number of d-o-f, RWG functions [37] are used as the basis functions $\boldsymbol{\psi}_p$. The matrices used in modal decomposition have been computed using in-house solvers AToM [1] and IDA [40], see Appendix A for details. Results from the commercial electromagnetic solver FEKO [4] are also presented for comparison. Computations that require a higher precision than the double precision arithmetic are performed using the mpmath Python library [29], and the Advanpix Matlab toolbox [3].

3.1 Radiation Modes

The eigenvalues for the radiation modes [39] are easily found using the eigenvalue problem

$$\mathbf{R}\mathbf{I}_n = \xi_n \mathbf{I}_n, \tag{3.1}$$

where ξ_n are the eigenvalues of the matrix $\mathbf{R}$, and $\mathbf{I}_n$ are the eigencurrents. The symmetry and indefiniteness of the matrix $\mathbf{R}$ pose a problem in the eigenvalue decomposition (3.1) as illustrated in [9, 19]. In this paper we show that the indefiniteness caused by the numerical noise can be bypassed using the matrix $\mathbf{S}$. We start with the singular value decomposition (SVD) of the matrix $\mathbf{S}$

$$\mathbf{S} = \mathbf{U}\boldsymbol{\Lambda}\mathbf{V}^{\mathrm{H}}, \tag{3.2}$$

where $\mathbf{U}$ and $\mathbf{V}$ are unitary matrices, and $\boldsymbol{\Lambda}$ is a diagonal matrix containing singular values of $\mathbf{S}$. Inserting (2.10), (3.2) into (3.1) and multiplying the left with $\mathbf{V}^{\mathrm{H}}$ yields

$$\boldsymbol{\Lambda}^{\mathrm{H}}\boldsymbol{\Lambda}\widetilde{\mathbf{I}}_n = \xi_n \widetilde{\mathbf{I}}_n \tag{3.3}$$

where the eigenvectors are rewritten as $\widetilde{\mathbf{I}}_n \equiv \mathbf{V}^{\mathrm{H}}\mathbf{I}_n$, and the eigenvalues are $\xi_n = \Lambda_{nn}^2$.

To compare the eigenvalues ξ_n of different mesh grids, the MoM matrices have to be normalized. The normalized matrices are $\widehat{\mathbf{R}} = \mathbf{L}\mathbf{R}\mathbf{L}$, $\widehat{\boldsymbol{\xi}} = \mathbf{L}\boldsymbol{\xi}\mathbf{L}$, $\widehat{\mathbf{S}} = \mathbf{S}\mathbf{L}$, $\widehat{\mathbf{I}}_n = \mathbf{L}^{-1}\mathbf{I}_n$, where $\mathbf{L}$ is the diagonal matrix of basis functions' reciprocal edge lengths, *i.e.*, $L_{pp} = 1/l_p$.

The advantage of using (3.3) to compute the radiation modes is illustrated in Fig. 4 for a spherical shell (Example #1). It can be seen that the number of modes computed using (3.3) is significantly higher compared to (3.1). The number of computed modes can be extended further by using quadruple precision to compute the SVD of the matrix $\mathbf{S}$. The results are similar for the rectangular plate (Example #5) illustrated in Fig. 5. The number of correct modes are shown in Table 3 for all the examples.

3.2 Characteristic Modes (CMs)

The generalized eigenvalue problem (GEP) with the matrix $\mathbf{R}$ on the right hand side, *i.e.*, serving as a weighting operator [44], is much more involved as the

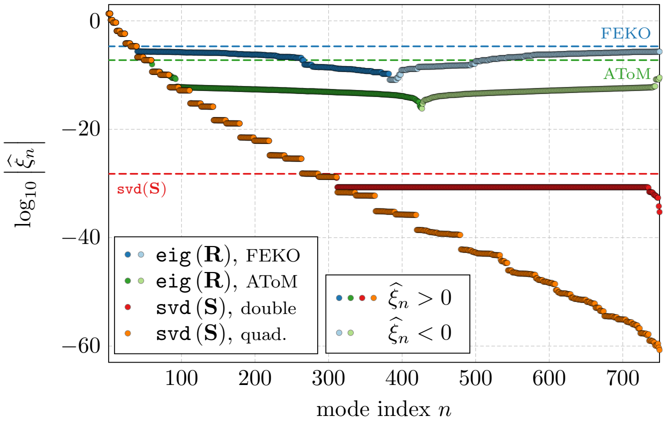

Figure 4: Normalized eigenvalues of the matrix **R** of a spherical shell with electrical size $ka = 0.5$ discretized into 500 triangles (Example #1). Multiprecision package Advanpix [3] has been used for evaluation in quadruple precision. The number of well-determined modes is delimited by horizontal dashed lines.

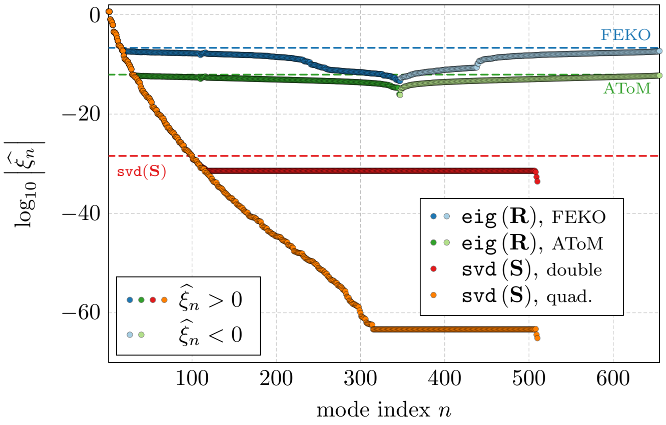

Figure 5: Normalized eigenvalues of the matrix **R** of rectangular plate (Example #5). Since the matrix **S** has only 510 rows, the number of modes is limited. The number of well-determined modes is delimited by horizontal dashed lines.

Example	Number of properly calculated modes				
	$\mathbf{RI} = \xi_n \mathbf{I}_n$		$\mathbf{XI}_n = \lambda_n \mathbf{RI}_n$		
(see Table 2)	(3.1)	(3.3)	(3.4)	$\mathbf{R} = \mathbf{S}^{\mathrm{T}}\mathbf{S}$	(3.8)
#1	59	284	**70** (5)	96 (6)	**284** (11)
#2	96	364	**105** (6)	197 (9)	**389** (13)
#3	59	311	**70** (5)	96 (6)	**306** (11)
#4	31	109	**29**	35	**37**
#5	29	117	**26**	33	**98**
#6	28	116	**22**	26	**98**

Table 3: Comparison of the number of modes correctly found by the classical and the novel methods for examples listed in Table 2. Columns 2–3 summarize the radiation modes and columns 4–6 summarize the CMs. Values in parentheses depicts the number of non-degenerated TM and TE modes found on spherical shell. The main outcome of the table, comparison of the CMs is highlighted by bold type.

problem cannot be completely substituted by the SVD. Yet, the SVD of the matrix $\mathbf{S}$ in (3.2) plays an important role in the CM decomposition.

The CM decomposition is defined here with a GEP as

$$\mathbf{XI}_n = \lambda_n \mathbf{RI}_n, \tag{3.4}$$

which is known to suffer from limited numerical dynamics [9], therefore delivering only a limited number of modes. The first step is to represent the solution in a basis of singular vectors $\mathbf{V}$ by substituting the matrix $\mathbf{R}$ in (3.4) as (2.10), with (3.2) and multiplying (3.4) from the left by the matrix $\mathbf{V}^{\mathrm{H}}$

$$\mathbf{V}^{\mathrm{H}}\mathbf{X}\mathbf{V}\mathbf{V}^{\mathrm{H}}\mathbf{I}_n = \lambda_n \boldsymbol{\Lambda}^{\mathrm{H}}\boldsymbol{\Lambda}\mathbf{V}^{\mathrm{H}}\mathbf{I}_n. \tag{3.5}$$

Formulation (3.5) can formally be expressed as a GEP with an already diagonalized right hand side [5]

$$\widetilde{\mathbf{X}}\widetilde{\mathbf{I}}_n = \lambda_n \widetilde{\mathbf{R}}\widetilde{\mathbf{I}}_n, \tag{3.6}$$

i.e., $\widetilde{\mathbf{X}} \equiv \mathbf{V}^{\mathrm{H}}\mathbf{X}\mathbf{V}$, $\widetilde{\mathbf{R}} \equiv \boldsymbol{\Lambda}^{\mathrm{H}}\boldsymbol{\Lambda}$, and $\widetilde{\mathbf{I}}_n \equiv \mathbf{V}^{\mathrm{H}}\mathbf{I}_n$.

Since the matrix $\mathbf{S}$ is in general rectangular, it is crucial to take into account cases where $N_\alpha < N_\psi$. This is equivalent to a situation in which there are limited number of spherical projections to recover the CMs. Consequently, only limited number of singular values Λ_{nn} exist. In such a case, the procedure similar to the one used in [24] should be undertaken by partitioning (3.6) into two linear systems

$$\widetilde{\mathbf{X}}\widetilde{\mathbf{I}} = \begin{pmatrix} \widetilde{\mathbf{X}}_{11} & \widetilde{\mathbf{X}}_{12} \\ \widetilde{\mathbf{X}}_{21} & \widetilde{\mathbf{X}}_{22} \end{pmatrix} \begin{pmatrix} \widetilde{\mathbf{I}}_{1n} \\ \widetilde{\mathbf{I}}_{2n} \end{pmatrix} = \begin{pmatrix} \lambda_{1n}\widetilde{\mathbf{R}}_{11}\widetilde{\mathbf{I}}_{1n} \\ \mathbf{0} \end{pmatrix} \tag{3.7}$$

where $\widetilde{\mathbf{I}}_{1n} \in \mathbb{C}^{N_\alpha}$, $\widetilde{\mathbf{I}}_{2n} \in \mathbb{C}^{N_\psi - N_\alpha}$, and $N_\alpha < N_\psi$. The Schur complement is obtained by substituting the second row of (3.7) into the first row

$$\left(\widetilde{\mathbf{X}}_{11} - \widetilde{\mathbf{X}}_{12}\widetilde{\mathbf{X}}_{22}^{-1}\widetilde{\mathbf{X}}_{21}\right)\widetilde{\mathbf{I}}_{1n} = \lambda_{1n}\widetilde{\mathbf{R}}_{11}\widetilde{\mathbf{I}}_{1n} \tag{3.8}$$

with expansion coefficients of CMs defined as

$$\widetilde{\mathbf{I}}_n = \begin{pmatrix} \widetilde{\mathbf{I}}_{1n} \\ -\widetilde{\mathbf{X}}_{22}^{-1}\widetilde{\mathbf{X}}_{21}\widetilde{\mathbf{I}}_{1n} \end{pmatrix}. \tag{3.9}$$

As far as the matrices $\mathbf{U}$ and $\mathbf{V}$ in (3.2) are unitary, the decomposition (3.6) yields CMs implicitly normalized to

$$\widetilde{\mathbf{I}}_n^{\mathrm{H}}\widetilde{\mathbf{R}}\widetilde{\mathbf{I}}_m = \delta_{nm}, \tag{3.10}$$

which is crucial since the standard normalization cannot be used without decreasing the numerical dynamics. In order to demonstrate the use of (3.8), various examples from Table 2 are calculated and compared with the conventional approach (3.4).

The CMs of the spherical shell from Example #1 are calculated and shown as absolute values in logarithmic scale in Fig. 6. It is shown that the number of the CMs calculated by classical procedure (FEKO, AToM) is limited to the lower modes, especially considering the degeneracy $2l+1$ of the CMs on the spherical shell [9]. The number of properly found CMs is significantly higher when using (3.8) than the conventional approach (3.4) and numerical dynamics are doubled. Notice that, even (3.4) where the matrix $\mathbf{R}$ calculated from (2.10) yields slightly better results than the conventional procedure. This fact is confirmed in Fig. 7 dealing with Example #5, where the multiprecision package Advanpix is used as a reference. The same calculation proves that the matrix $\mathbf{R}$ contains all information to recover the same number of modes as (3.8), but this can be done only at the expense of higher computational time, see Table 4.

Two tests proposed in [9] are performed to validate the conformity of characteristic current densities and the characteristic far fields with the analytically known values. The results of the former test are depicted in Fig. 8 for Example #1 and #3 that are spherical shells with two different d-o-f. Similarity coefficients $\chi_{\tau n}$ are depicted both for the CMs using the matrix $\mathbf{R}$ (3.4) and for the CMs calculated by (3.8). The number of valid modes correlates well with Table 3 and the same dependence on the quality and size of the mesh grid as in [9] is observed.

Qualitatively the same behavior is also observed in the latter test, depicted in Fig. 9. The similarity of the characteristic far fields, expressed by coefficient $\zeta_{\tau n}$ [9], were slightly modified here to preserve the numerical dynamics of

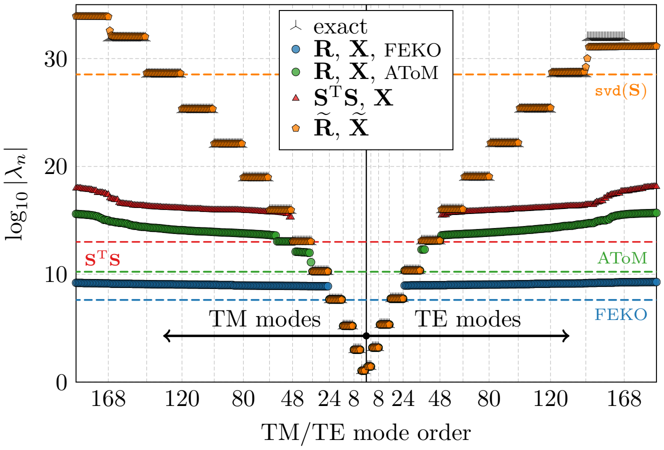

Figure 6: The absolute values of the CMs of spherical shell with electrical size $ka = 0.5$ (Example #1). Data calculated with classical procedure (3.4) are compared with techniques from this paper, (3.5), (3.8), and with the analytical results valid for the spherical shell [9].

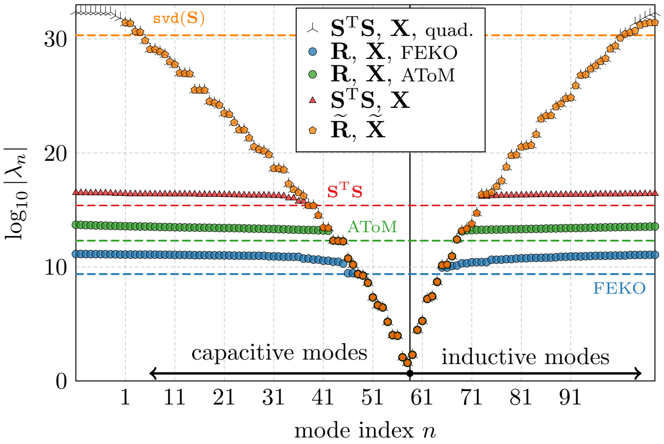

Figure 7: The absolute values of the CMs of rectangular plate (Example #5). Since unknown analytical results, the multiprecision package Advanpix has been used instead to calculate the first 150 modes from impedance matrix in quadruple precision.

Example		Time to calculate N_λ CMs (s)			
(see Table 2)	N_λ	(3.4)	$\mathbf{R} = \mathbf{S}^{\mathrm{T}}\mathbf{S}$	(3.8)	(3.4) & Advanpix
#1	300	5.5	2.9	**2.5**	**53334.4**
#4	100	0.7	0.7	**0.5**	**1324.8**

Table 4: Comparison of computational time required by various methods capable to calculate first N_λ CMs. Only the methods in the last two columns (highlighted by bold type) are able to calculate required modes properly. The multiprecision package Advanpix was used to calculate decomposition (3.4) using quadruple precision. The calculations were done on Windows Server 2012 with 2×Xeon E5-2665 CPU @ 2.4 GHz and 72 GB RAM.

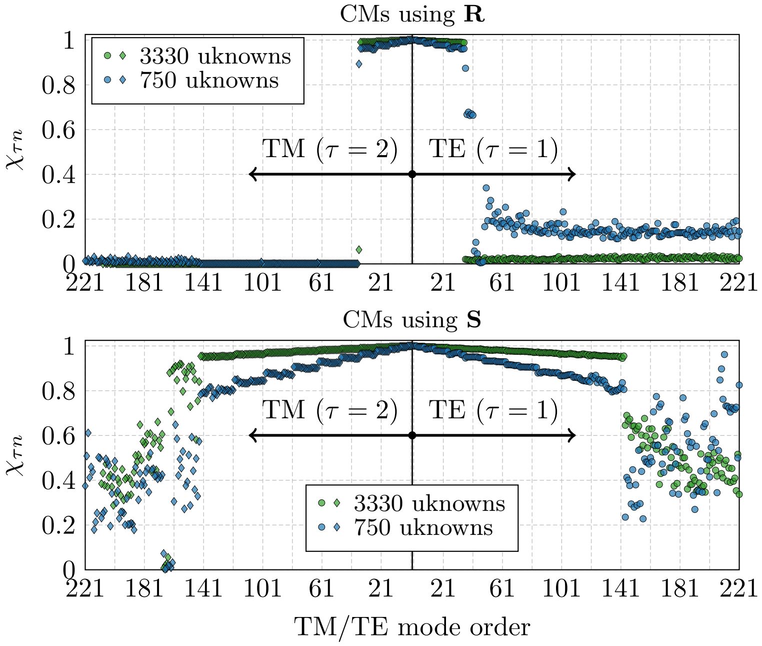

Figure 8: Similarity of numerically evaluated characteristic currents for a spherical shell of two different discretizations (Example #1 and #3) and the analytically known currents [9]. The coefficients $\chi_{\tau n}$ were calculated according to [9], top panel depicts results for the conventional procedure (3.4), bottom panel for the procedure from this paper (3.8).

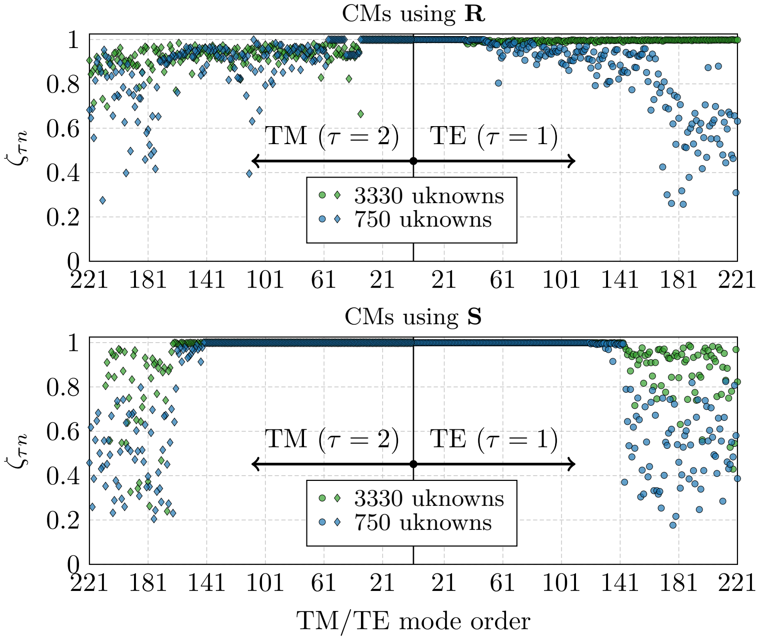

Figure 9: Similarity of numerically and analytically evaluated characteristic far fields for a spherical shell of two different discretizations (Example #1 and #3) and analytically known far fields [9]. The coefficients $\zeta_{\tau n}$ were calculated according to [9], top panel depicts results for the conventional procedure (3.4), bottom panel for the procedure from this paper (3.8).

the calculated characteristic far fields. The coefficients read

$$\zeta_{\tau n} = \frac{\max\limits_{l} \sum\limits_{\sigma m} \left|P_{\alpha n}\right|^2}{\sum\limits_{\alpha} \left|P_{\alpha n}\right|^2}, \tag{3.11}$$

where

$$P_{\alpha n} = \frac{1}{2Z_0} \int_0^{2\pi} \int_0^{\pi} \mathbf{Y}_\alpha\left(\hat{\boldsymbol{r}}\right) \cdot \boldsymbol{F}_n\left(\hat{\boldsymbol{r}}\right) \sin\vartheta \, \mathrm{d}\vartheta \, \mathrm{d}\varphi \tag{3.12}$$

with $\boldsymbol{F}_n$ being the characteristic far fields evaluated for a spherical shell using (2.13) with $[\widetilde{f}_\alpha] = \mathbf{S}\mathbf{I}_n$. The characteristic far fields computed from the conventional procedure (3.4) and the procedure presented in this paper (3.8) are illustrated in Fig. 9.

Lastly, practical advantages of using (3.8) over (3.4), are demonstrated in the Fig. 10, comparing the 41st CM of the rectangular plate (Example #5). The surface current density in the left panel, calculated using $\mathbf{I}_{41}$ in (3.4) is, in fact, only the numerical noise. However, in the right panel, the current density calculated by (3.8) corresponds to some of the higher-order modes. Refining the mesh grid, even higher modes can be calculated with (3.8), see Fig. 11. These higher-order modes can be utilized for specialized applications covering antenna arrays, electrically large structures, numerical benchmarks, or precise tracking algorithms.

4 Discussion

Important aspects of the utilization of the matrix $\mathbf{S}$ are discussed under independent headings, covering the theory, numerical treatments, and potential improvements to be considered for the future.

4.1 Physical Meaning and Usefulness

Unlike the reactance matrix $\mathbf{X}$, the resistance matrix $\mathbf{R}$ suffers from high condition number. This fact is a direct consequence of only a a small number of well-radiating (spherical) modes, especially notable in the electrically small regime. Therefore, the combined approach to evaluate the impedance matrix (matrix $\mathbf{R}$ using matrix $\mathbf{S}$, matrix $\mathbf{X}$ using conventional Green function technique with double integration) takes advantages of both methods and seems to be optimal for, *e.g.*, modal decomposition techniques dealing with the matrix $\mathbf{R}$ (radiation modes [39], CMs, energy modes [28,39], and solution of optimization problems [10]). Evaluation and the SVD of the matrix $\mathbf{S}$ are also used to estimate number of modes, *cf.* number of modes of the matrix $\mathbf{S}$ found by (3.2) and number of CMs found by (3.8) in Table 3.

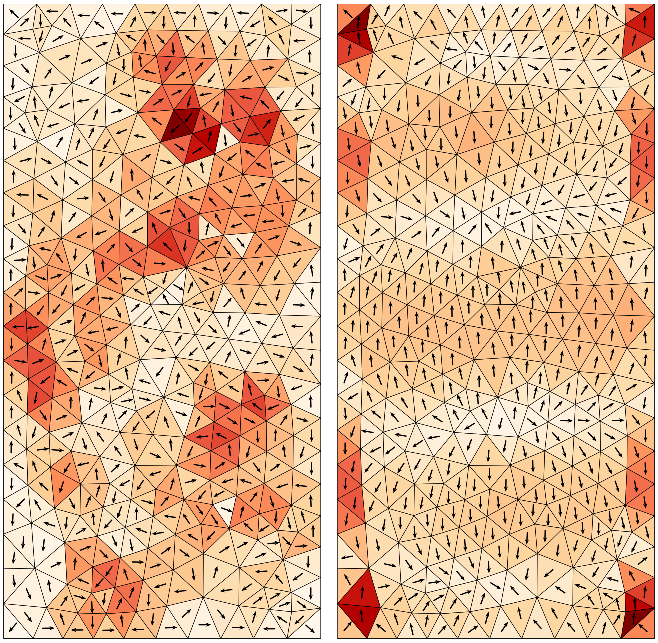

Figure 10: Comparison of the 41^{st} CM of the rectangular plate (Example #5), left panel: conventional procedure (3.4), right panel: procedure from this paper (3.8).

Evaluation of the matrix $\mathbf{S}$ is done only for source current in free-space. This requirement is, however, quite common in the context of the modal methods: the CMs are originally defined exclusively in free-space as the far fields have to be orthogonal [16].

The fact that all modes cannot be recovered even with specialized techniques poses a question about completeness of the modal bases. This theoretical problem is left aside in this paper as it has been observed that the number of properly found modes is strictly limited by the number of projections N_α, the number of basis functions N_ψ, the electrical size ka, and, for particular numerical procedure, by limited numerical dynamics. Therefore, the completeness of the modes is far from being granted, which introduces serious problems for applications that require a complete basis, *e.g.* in selective excitation of modes.

4.2 Computational Aspects

Computational gains of the proposed method presented in Table 1 can be interpreted in two ways: either the same amount of modes can be calculated faster than the conventional approach, or a (significantly) higher number of modes can be calculated investing the same amount of computational time as the conventional method.

Importantly, convergence requirements summarized in Fig. 1 can easily be

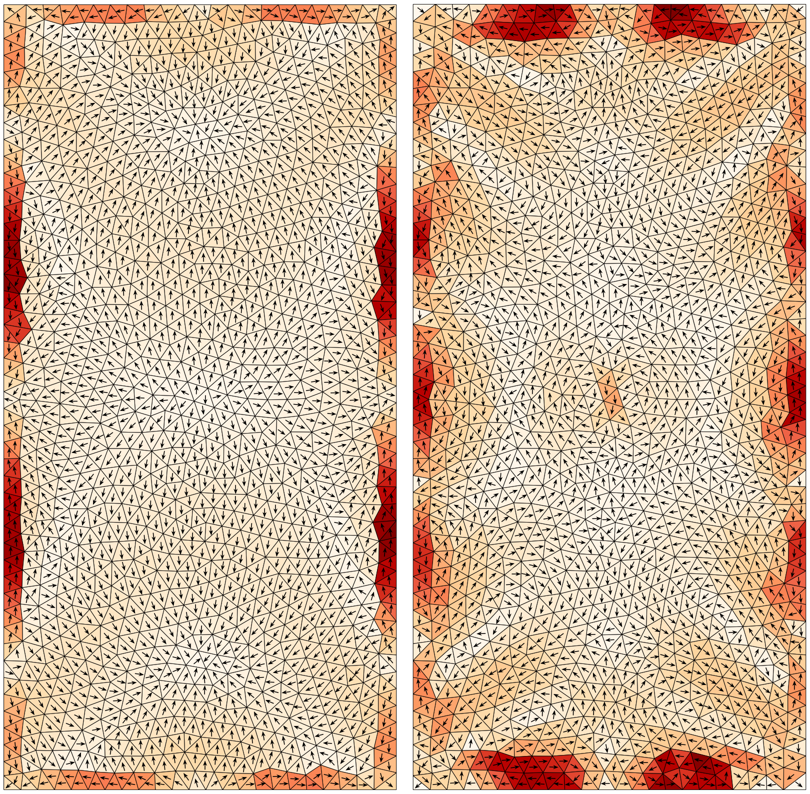

Figure 11: Two high-order modes of rectangular plate (Example #6), found by procedure from this paper. Mode in the left panel is capacitive with $\lambda_{77} = -1.947 \cdot 10^{24}$, mode in the right panel is inductive with $\lambda_{17} = 2.461 \cdot 10^{17}$.

met. Subsequently, only spherical Bessel functions up to the order $L = 12$ are needed to get double precision matching between matrices $\mathbf{R}$ and $\mathbf{S}^{\mathrm{T}}\mathbf{S}$ even for relatively high frequencies ($ka = 3$).

An advantage of the proposed method is that the matrix $\mathbf{S}$ is rectangular for $N_\alpha < N_\psi$, allowing independent selection of the parameters N_ψ and N_α. While the parameter N_ψ controls the details in the model, the parameter N_α (or alternatively L) controls the convergence of the matrix $\mathbf{S}$ and the number of modes to be found. Notice that the parameter N_α is limited from below by the convergence and the number of desired modes, but also from above since the spherical Bessel function in $\mathbf{u}_\alpha^{(1)}(k\boldsymbol{r})$ decays rapidly with l as

$$\mathrm{j}_l\,(ka) \approx \frac{2^l l!}{(2l+1)!}\,(ka)^l\,, \quad ka \to 0. \tag{4.1}$$

4.3 Potential Improvements

Even though the numerical dynamics are remarkably improved, they are strictly limited and they present an inevitable, thus fundamental, bottleneck of all modal methods involving radiation properties. The true technical limitation is the SVD of the matrix $\mathbf{S}$. A possible remedy is the use of high-precision packages that come at an expense of markedly longer computation times and the necessity of performing all subsequent operations in the same package to preserve high numerical precision.

The second potential improvement relies on higher-order basis functions, which can compensate a poor-meshing scheme (that is sometimes unavoidable for complex or electrically large models). It can also reduce the number of basis function N_ψ so that the evaluation of (2.11), (2.10), and (3.2) are further accelerated.

5 Conclusion

Evaluation of the discretized form of the EFIE impedance operator, the impedance matrix, has been reformulated using projection of spherical harmonics onto a set of basis functions representing the radiator. The key feature of the proposed method is the fact that the real part of the impedance matrix can be written as a multiplication of the spherical modes projection matrix with itself. This feature opens new possibilities in a wide area of modal decomposition techniques given that the achievable numerical dynamics are doubled. Consequently, the proposed method resolves a class of fundamental problems of CM decomposition.

The approach presented here opens new ways to deal with complicated examples, *i.e.*, geometrically complex shapes, electrically large structures, or symmetrical bodies. Moreover, the approach may also improve performance of tracking algorithms and feeding synthesis, essential tools for modal decomposition techniques.

For radiators located in free-space, the proposed method leads to faster evaluation and higher number of modes properly found as compared with the conventional procedure. The method is of particular interest for all cases in which the number of desired modes is high including small antenna analysis, design of antenna arrays, and antenna synthesis in general. The results obtained by the method can also be used as reference for validation and benchmarking. These facts have been confirmed via comparison with analytically known results. Additionally, the doubled numerical dynamics lead to roughly four times more modes.

It has been shown that the method has notable advantages, namely the number of available modes can be estimated prior to the decomposition and the convergence can be controlled via the number of basis functions and the number of projections. The normalization of generalized eigenvalue problems with respect to the product of the spherical modes projection matrix on the right hand side are implicitly done. The presented procedure finds its use in various optimization techniques as well. It allows for example to prescribe the radiation pattern of optimized current by restricting the set of the spherical harmonics used for construction of the matrix.

The method can be straightforwardly implemented into both in-house and commercial solvers, improving thus their performance and providing antenna designers with more accurate and larger sets of modes.

Appendix A Used Computational Electromagnetics Packages

A.1 FEKO

FEKO (ver. 14.0-273612, [4]) has been used with a mesh structure that was imported in NASTRAN file format [2]: CMs and far fields were chosen from the model tree under *requests* for the FEKO solver. Data from FEKO were acquired using *.out, *.os, *.mat and *.ffe files. The impedance matrices were imported using an in-house wrapper [40]. Double precision was enabled for data storage in solver settings.

A.2 AToM

AToM (pre-product ver., CTU in Prague, [1]) has been used with a mesh grid that was imported in NASTRAN file format [2], and simulation parameters were set to comply with the data in Table 2. AToM uses RWG basis functions with the Galerkin procedure [37]. The Gaussian quadrature is implemented according to [14] and singularity treatment is implemented from [15]. Built-in Matlab functions are utilized for matrix inversion and decomposition. Multiprecision package Advanpix [3] is used for comparison purposes.

A.3 IDA

IDA (in-house, Lund University, [40]) has been used with the NASTRAN mesh and processed with the IDA geometry interpreter. IDA solver is a Galerkin type MoM implementation. RWG basis functions are used for the current densities. Numerical integrals are performed using Gaussian quadrature [14] for non-singular terms and the DEMCEM library [33–36] for singular terms. Intel MKL library [26] is used for linear algebra routines. The matrix computation routines are parallelized using OpenMP 2.0 [13]. Multiprecision computations were done with the mpmath Python library [29].

Appendix B Spherical Vector Waves

General expression of the (scalar) spherical modes is [30]

$$\mathrm{u}_{\sigma ml}^{(p)}(k\boldsymbol{r}) = \mathrm{z}_l^{(p)}(kr)\mathrm{Y}_{\sigma ml}\left(\hat{\boldsymbol{r}}\right), \tag{B.1}$$

with $\hat{\boldsymbol{r}} = \boldsymbol{r}/|\boldsymbol{r}|$ and k being the wavenumber. The indices are $m \in \{0,\dots,l\}$, $\sigma \in \{\mathrm{e},\mathrm{o}\}$ and $l \in \{1,\dots,L\}$ [20, 21]. For regular waves $\mathrm{z}_l^{(1)} = \mathrm{j}_l$ is a spherical Bessel function of order l, irregular waves $\mathrm{z}_l^{(2)} = \mathrm{n}_l$ is a spherical Neumann function, and $\mathrm{z}_l^{(3,4)} = \mathrm{h}_l^{(1,2)}$ are spherical Hankel functions for the ingoing and outgoing waves, respectively. Spherical harmonics are defined as [30]

$$\mathrm{Y}_{\sigma ml}\left(\hat{\boldsymbol{r}}\right) = \sqrt{\frac{\varepsilon_m}{2\pi}}\widetilde{P}_l^m\left(\cos\vartheta\right)\begin{Bmatrix}\cos m\varphi\\ \sin m\varphi\end{Bmatrix}, \quad \sigma = \begin{Bmatrix}\mathrm{e}\\ \mathrm{o}\end{Bmatrix} \tag{B.2}$$

with $\varepsilon_m = 2 - \delta_{m0}$ the Neumann factor, δ_{ij} the Kronecker delta function and $\tilde{\mathrm{P}}_l^m\left(\cos\vartheta\right)$ the normalized associated Legendre functions [32].

The real-valued spherical vector waves are [21, 30]

$$\mathbf{u}_{1\sigma ml}^{(p)}\left(k\boldsymbol{r}\right) = \mathrm{R}_{1l}^{(p)}\left(kr\right)\mathbf{Y}_{1\sigma ml}\left(\hat{\boldsymbol{r}}\right), \tag{B.3a}$$

$$\mathbf{u}_{2\sigma ml}^{(p)}\left(k\boldsymbol{r}\right) = \mathrm{R}_{2l}^{(p)}\left(kr\right)\mathbf{Y}_{2\sigma ml}\left(\hat{\boldsymbol{r}}\right) + \mathrm{R}_{3l}^{(p)}\left(kr\right)\mathrm{Y}_{\sigma ml}\left(\hat{\boldsymbol{r}}\right)\hat{\boldsymbol{r}}, \tag{B.3b}$$

where $\mathrm{R}_{\tau l}^{(p)}\left(kr\right)$ are the radial function of order l defined as

$$\mathrm{R}_{\tau l}^{(p)}\left(\kappa\right) = \begin{cases} \mathrm{z}_l^{(p)}(\kappa), & \tau = 1, \quad \text{(B.4a)}\\ \dfrac{1}{\kappa}\dfrac{\partial}{\partial\kappa}\left(\kappa\mathrm{z}_l^{(p)}\left(\kappa\right)\right), & \tau = 2, \quad \text{(B.4b)}\\ \dfrac{b_l}{\kappa}\mathrm{z}_l^{(p)}(\kappa), & \tau = 3, \quad \text{(B.4c)}\end{cases}$$

with

$$b_l = \sqrt{l\left(l+1\right)} \tag{B.5}$$

and $\mathbf{Y}_{\tau\sigma ml}\left(\hat{\boldsymbol{r}}\right)$ denotes the real-valued vector spherical harmonics defined as

$$\mathbf{Y}_{1\sigma ml}\left(\hat{\boldsymbol{r}}\right) = \frac{1}{b_l}\nabla \times \left(\boldsymbol{r}\mathrm{Y}_{\sigma ml}\left(\hat{\boldsymbol{r}}\right)\right), \tag{B.6a}$$

$$\mathbf{Y}_{2\sigma ml}\left(\hat{\boldsymbol{r}}\right) = \hat{\boldsymbol{r}} \times \mathbf{Y}_{1\sigma ml}\left(\hat{\boldsymbol{r}}\right), \tag{B.6b}$$

where $\mathrm{Y}_{\sigma ml}$ denotes the ordinary spherical harmonics [30].

Appendix C Associated Legendre Polynomials

The associated Legendre functions are defined [27] as

$$P_l^m\left(x\right) = \left(1-x^2\right)^{m/2}\frac{\mathrm{d}^m}{\mathrm{d}x^m}P_l(x), \quad l \geqslant m \geqslant 0, \tag{C.1}$$

with

$$P_l\left(x\right) = \frac{1}{2^l l!}\frac{\mathrm{d}^l}{\mathrm{d}x^l}\left(x^2-1\right)^l \tag{C.2}$$

being the associated Legendre polynomials of degree l and $x \in [-1,1]$. One useful limit when computing the vector spherical harmonics is [30]

$$\lim_{x\to 1}\frac{P_l^m\left(x\right)}{\sqrt{1-x^2}} = \delta_{m1}\frac{l\left(l+1\right)}{2}. \tag{C.3}$$

The normalized associated Legendre function $\tilde{P}_l^m$, is defined as follows

$$\widetilde{P}_l^m\left(x\right) = \sqrt{\frac{2l+1}{2}\frac{(l-m)!}{(l+m)!}}P_l^m\left(x\right). \tag{C.4}$$

The derivative of the normalized associated Legendre function is required when computing the spherical harmonics, and is given by the following recursion relation

$$\begin{aligned}\frac{\partial}{\partial\vartheta}\widetilde{P}_l^m\left(\cos\vartheta\right) = \frac{1}{2}&\sqrt{(l+m)(l-m+1)}\widetilde{P}_l^{m-1}\left(\cos\vartheta\right)\\ &-\frac{1}{2}\sqrt{(l-m)(l+m+1)}\widetilde{P}_l^{m+1}\left(\cos\vartheta\right)\end{aligned} \tag{C.5}$$

where $x \equiv \cos\vartheta$, $\vartheta \in [0,\pi]$.

References

[1] Antenna Toolbox for MATLAB (AToM), 2017.

[2] MSC NASTRAN, 2017.

[3] Advanpix. Multiprecision Computing Toolbox for MATLAB, 2016.

[4] Altair. FEKO, 2016.

[5] G. Angiulli and F. Venneri. Use of the simultaneous diagonalization technique in the $Ax = \lambda Bx$ eigenproblem applied to the computation of the characteristic modes. *ACES Journal*, **17**(3), 232–238, Nov. 2002.

[6] R. Burden, J. Faires, and A. Burden. *Numerical Analysis.* Cengage Learning, 2015.

[7] M. Capek, P. Hazdra, and J. Eichler. A method for the evaluation of radiation Q based on modal approach. *IEEE Trans. Antennas Propag.*, **60**(10), 4556–4567, Oct. 2012.

[8] M. Capek and L. Jelinek. Optimal composition of modal currents for minimal quality factor Q. *IEEE Trans. Antennas Propag.*, **64**(12), 5230–5242, 2016.

[9] M. Capek, V. Losenicky, L. Jelinek, and M. Gustafsson. Validating the characteristic modes solvers. *IEEE Trans. Antennas Propag.*, **65**(8), 4134–4145, Aug. 2017.

[10] M. Capek, M. Gustafsson, and K. Schab. Minimization of antenna quality factor. *IEEE Trans. Antennas Propag.*, **65**(8), 4115–4123, 2017.

[11] Y. Chen and C.-F. Wang. Electrically small UAV antenna design using characteristic modes. *IEEE Trans. Antennas Propag.*, **62**(2), 535–545, Feb. 2014.

[12] W. C. Chew, M. S. Tong, and B. Hu. *Integral Equation Methods for Electromagnetic and Elastic Waves.* Morgan & Claypool, 2009.

[13] L. Dagum and R. Menon. OpenMP: an industry standard api for shared-memory programming. *Computational Science & Engineering, IEEE*, **5**(1), 46–55, 1998.

[14] D. A. Dunavant. High degree efficient symmetrical gaussian quadrature rules for the triangle. *International Journal for Numerical Methods in Engineering*, **21**, 1129–1148, 1985.

[15] T. F. Eibert and V. Hansen. On the calculation of potential integrals for linear source distributions on triangular domains. *IEEE Trans. Antennas Propag.*, **43**(12), 1499–1502, Dec. 1995.

[16] R. J. Garbacz and R. H. Turpin. A generalized expansion for radiated and scattered fields. *IEEE Trans. Antennas Propag.*, **19**(3), 348–358, May 1971.

[17] W. C. Gibson. *The Method of Moments in Electromagnetics.* CRC press, 2014.

[18] G. H. Golub and C. F. Van Loan. *Matrix Computations.* Johns Hopkins University Press, 2012.

[19] M. Gustafsson, D. Tayli, C. Ehrenborg, M. Cismasu, and S. Norbedo. Antenna current optimization using MATLAB and CVX. *FERMAT*, **15**(5), 1–29, May–June 2016.

[20] M. Gustafsson and S. Nordebo. Characterization of MIMO antennas using spherical vector waves. *IEEE Trans. Antennas Propag.*, **54**(9), 2679–2682, 2006.

[21] J. E. Hansen, editor. *Spherical Near-Field Antenna Measurements.* Number 26 in IEE electromagnetic waves series. Peter Peregrinus Ltd., Stevenage, UK, 1988.

[22] R. F. Harrington. *Field Computation by Moment Methods.* Wiley – IEEE Press, 1993.

[23] R. F. Harrington. *Time-Harmonic Electromagnetic Fields.* Wiley – IEEE Press, 2 edition, 2001.

[24] R. F. Harrington and J. R. Mautz. Computation of characteristic modes for conducting bodies. *IEEE Trans. Antennas Propag.*, **19**(5), 629–639, Sept. 1971.

[25] R. F. Harrington and J. R. Mautz. Theory of characteristic modes for conducting bodies. *IEEE Trans. Antennas Propag.*, **19**(5), 622–628, 1971.

[26] Intel. Intel Math Kernel Library 2017 update 3. `https://software.intel.com/en-us/mkl`, 2017. Accessed: 2017-12-20.

[27] A. Jeffrey and H.-H. Dai. *Handbook of Mathematical Formulas and Integrals.* Academic Press, 4 edition, 2008.

[28] L. Jelinek and M. Capek. Optimal currents on arbitrarily shaped surfaces. *IEEE Trans. Antennas Propag.*, **65**(1), 329–341, Jan. 2017.

[29] F. Johansson et al. mpmath: a Python library for arbitrary-precision floating-point arithmetic (version 0.18). `http://mpmath.org/`, December 2013. Accessed: 2017-12-20.

[30] G. Kristensson. *Scattering of Electromagnetic Waves by Obstacles.* SciTech Publishing, an imprint of the IET, Edison, NJ, 2016.

[31] P. M. Morse and H. Feshbach. *Methods of Theoretical Physics*, volume 2. McGraw-Hill, New York, NY, 1953.

[32] F. W. J. Olver, D. W. Lozier, R. F. Boisvert, and C. W. Clark. *NIST Handbook of mathematical functions.* Cambridge University Press, New York, 2010.

[33] A. G. Polimeridis and T. V. Yioultsis. On the direct evaluation of weakly singular integrals in Galerkin mixed potential integral equation formulations. *IEEE Trans. Antennas Propag.*, **56**(9), 3011–3019, September 2008.

[34] A. G. Polimeridis. Direct evaluation method in computational electromagnetics (DEMCEM). `https://github.com/thanospol/DEMCEM`, 2010. Accessed: 2017-12-20.

[35] A. G. Polimeridis and J. R. Mosig. Complete semi-analytical treatment of weakly singular integrals on planar triangles via the direct evaluation method. *International journal for numerical methods in engineering*, **83**(12), 1625–1650, 2010.

[36] A. G. Polimeridis and J. R. Mosig. On the direct evaluation of surface integral equation impedance matrix elements involving point singularities. *IEEE Trans. Antennas Propag.*, **10**, 599–602, 2011.

[37] S. M. Rao, D. R. Wilton, and A. W. Glisson. Electromagnetic scattering by surfaces of arbitrary shape. *IEEE Trans. Antennas Propag.*, **30**(3), 409–418, May 1982.

[38] M. N. O. Sadiku. *Numerical Techniques in Electromagnetics with Matlab.* CRC Press, 3 edition, 2009.

[39] K. R. Schab and J. T. Bernhard. Radiation and energy storage current modes on conducting structures. *IEEE Trans. Antennas Propag.*, **63**(12), 5601–5611, Dec. 2015.

[40] D. Tayli. IDA (Integrated Development toolset for Antennas), 2017.

[41] M. Vogel, G. Gampala, D. Ludick, U. Jakobus, and C. Reddy. Characteristic mode analysis: Putting physics back into simulation. *IEEE Antennas Propag. Mag.*, **57**(2), 307–317, April 2015.

[42] P. C. Waterman. Symmetry, unitarity, and geometry in electromagnetic scattering. *Phys. Rev. D*, **3**(4), 825–839, 1971.

[43] P. Waterman. Matrix formulation of electromagnetic scattering. *Proc. IEEE*, **53**(8), 805–812, August 1965.

[44] J. H. Wilkinson. *The Algebraic Eigenvalue Problem.* Oxford University Press, 1988.

[45] B. Yang and J. J. Adams. Systematic shape optimization of symmetric MIMO antennas using characteristic modes. *IEEE Trans. Antennas Propag.*, **64**(7), 2668–2678, July 2016.

[46] D. Zuras, M. Cowlishaw, A. Aiken, M. Applegate, D. Bailey, S. Bass, D. Bhandarkar, M. Bhat, D. Bindel, S. Boldo, et al. IEEE standard for floating-point arithmetic. *IEEE Std 754-2008*, pages 1–70, 2008.

Synthesis of Large Endfire Antenna Arrays using Convex Optimization

Jakob Helander, Doruk Tayli, and Daniel Sjöberg

Paper IV

Published as: J. Helander, D. Tayli, and D. Sjöberg, “Synthesis of Large Endfire Antenna Arrays using Convex Optimization”, *IEEE Transactions on Antennas and Propagation*, 2017.

Abstract

An innovative approach utilizing convex optimization to simultaneously conduct pattern synthesis and improve the matching of large scale endfire antenna arrays is proposed in this paper. A fast full-wave analysis tool facilitates the computation of the necessary data for running the optimization routine, and enables analysis on arrays with dimensions $\mathbf{100}\lambda \times \mathbf{6}\lambda$ for the highest simulated frequency. Simulated results are provided for various array configurations of bowties, and the results show that improved matching can be obtained while maintaining a clear endfire far field pattern analogous to the pattern obtained with the classical Hansen-Woodyard excitation. The spatial dependence on the amplitude of the optimized input waves in the antenna ports indicate that a considerable fraction of the input power is fed to the antennas at the array's front, in the direction of where the main lobe is launched.

1 Introduction

Phased arrays are extensively utilized in a variety of wireless applications, e.g., satellite communications, radio-frequency identification (RFID), mobile systems and radar systems, in order to realize power gain and beamsteering [1]. In radar applications, electrically large arrays consisting of a vast number of antenna elements are commonly adopted in order to realize the high directivity, and the main lobe direction can easily be controlled by applying the appropriate progressive phase shift thus increasing the area of coverage as the beam is made steerable. Requirements are often set on the achievable pattern, with low side lobe levels and directivity as the main concerns for proper functionality of the array [5].

However, with a classical feeding approach [18] for endfire mode operation of an electrically large array, the problem of very strong coupling between the antenna elements arises. Since the array is a multiport system, this impacts the overall matching of the array. Even if high directivity is achieved, the realized gain in the endfire direction might still be considerably compromised by the overall mismatch of the array. For instance, the uniform feeding by Hansen-Woodyard [13] is commonly known to be poorly matched. From a design-synthesis perspective, this indicates that the radiation characteristics of the endfire array is not the sole concern. Rather, the overall matching of the array is essential.

The uneven loading occurring under the endfire excitation puts restrictions on the numerical methods that can be adopted for simulating electrically large arrays with arbitrary complexity of the antenna geometry. Periodic boundary conditions, a useful tool for large arrays of uniform spacing, can not be employed due to this loading. Therefore, full-wave simulations are required for the problem at hand.

A widely used full-wave analysis tool is the MoM [8] which scales as $\mathcal{O}(N^3)$ in computational complexity for N degrees of freedom in its standard form when solving the system of equations. It is thus dependent on hybrid techniques in order to run time-efficient simulations on electrically large geometries. To date, there are numerous approaches for hybridizing the conventional MoM, two of which are the MBF method [4,14,21,22,28] and the ACA algorithm [2,33]. Both methods have the advantage of being relatively simple to implement as add-ons to an existing MoM code, and, if used jointly, they offer a significant reduction of both run time and memory usage [14,22]. Due to this joint utilization, it is feasible to conduct full-wave analysis of large-scale arrays, and output the data necessary for running post process synthesis routines in a time efficient manner. For instance, the MBF method facilitates the calculation of the EEP which is essential for invoking the effect of mutual coupling in the pattern synthesis problem.

A powerful synthesis tool used extensively in the field of electromagnetics is convex optimization [11,12,24,26]. If the problem under consideration can be expressed in convex form, the optimum solution can be found rapidly using convex programming toolboxes [3]. Pattern synthesis using optimization techniques is not a novel concept [6,20]. In fact, convex optimization in particular was used for this purpose around twenty years ago [19] albeit limited to less extensive problems due to the computational limitations of the time. However, as the power and speed of computers have increased over the past decade, new momentum has been added to this research front, and recent publications have shown the applicability of convex optimization in synthesis problems for arrays of increasing sizes and more complex antenna geometries [7,25,31,32]. For example, in [31] convex optimization is used together with a fast full-wave scheme in order to optimize antenna positioning in large aperiodic arrays. Pattern synthesis using constraints on the magnitude response of the main lobe is presented in [32] for moderate-sized arrays.

In this paper, we present synthesis results for electrically large arrays of printed bowtie antennas operating in endfire mode. The convex optimization formulation presented optimizes the performance of a particular array design with respect to the overall matching with constraints set on the far field pattern. The full-wave analysis tool developed in-house utilizes the MBF method and the ACA algorithm, and produces the essential input data for running the optimization problem. To the authors' knowledge, these are the first results provided for endfire arrays of such sizes that treat the problems of pattern synthesis and array matching simultaneously.

The results indicate that bandwidth enhancement and improved matching can be realized while simultaneously achieving a clear endfire far field pattern. Moreover, once the full-wave simulation of the array has been run for the desired frequency range, the convex optimization can be executed as an independent post-processing routine. The complete scheme can easily be invoked in the already existing design process of endfire antenna arrays.

2 Full-Wave Analysis

The original equation system for the finite antenna array in the RWG basis is described by the full MoM representation,

$$\mathbf{Z}\boldsymbol{I} = \boldsymbol{V}, \tag{2.1}$$

which can be divided into sub-blocks $\mathbf{Z}_{n,m}$ and $\boldsymbol{V}_n$ that contains the coupling terms between subdomain n and m, and the excitation of subdomain n, respectively. The array under consideration consists of non-contacting antenna elements, and every antenna therefore constitutes a corresponding subdomain. The hybridized MoM used in this work utilizes two approaches for acceleration: the MBF method and the ACA algorithm [33].

2.1 Compression

The MBF method utilizes an aggregated basis to reduce the size of each sub-block $\mathbf{Z}_{n,m}$ and $\boldsymbol{V}_n$, and the overall equation system is thereby retained in a compressed version. The procedure of generating the MBFs, i.e., the aggregated basis functions, consists of a series of steps presented in [14] for the choice of implementation, but alternative versions are available in [4,21,22,28]. In essence, the compression is realized by employing a set of orthonormal MBFs for each antenna:

$$\begin{aligned} \mathbf{Z}_{n,m}^{\mathrm{mbf}} &= \mathbf{U}_n^{\mathrm{T}}\mathbf{Z}_{n,m}\mathbf{U}_m \\ \boldsymbol{V}_n^{\mathrm{mbf}} &= \mathbf{U}_n^{\mathrm{T}}\boldsymbol{V}_i \\ n = 1,2,\ldots,N;& \quad m = 1,2,\ldots,N. \end{aligned} \tag{2.2}$$

Here, n and m are antenna indices, $\cdot^{\mathrm{T}}$ denotes the transpose and a total of N antennas is assumed in the array. The columns in $\mathbf{U}_n$ each represents a MBF on antenna n. The overall reduction of unknowns is hence determined by the number of MBFs, which in turn depends on a user-defined accuracy of the resolved induced currents [15].

2.2 Accelerated Computation of Sub-blocks

The ACA algorithm produces a low-rank approximation $\widetilde{\mathbf{Z}}$ to a matrix $\mathbf{Z}$, and is here employed to accelerate the calculation of the sub-blocks $\mathbf{Z}_{n,m}$. The method, introduced in [2] and described thoroughly in [33], is entirely algebraic and therefore also independent of the kernel of the integral equation. Moreover, the algebraic nature makes it easy to implement on top of an existing MoM-code. In short, the sub-block matrix $\mathbf{Z}_{n,m}$ in the RWG basis is approximated by a sum of r dyadic products of rows $\mathbf{R}$ and columns $\mathbf{C}$,

$$\mathbf{Z}_{n,m}^{k\times l} \approx \widetilde{\mathbf{Z}}_{n,m}^{k\times l} = \mathbf{R}^{k\times r}\mathbf{C}^{r\times l}, \tag{2.3}$$

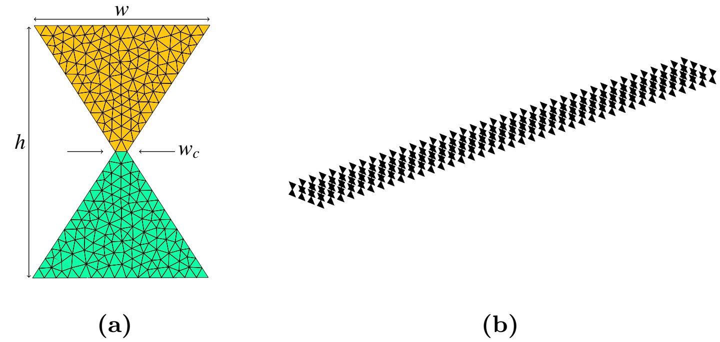

Figure 1: (a) Meshview of the bowtie antenna element with height $h = 1\,\text{m}$, width $w = 0.75\,\text{m}$ and center width $w_\text{c} = 0.05\,\text{m}$. (b) Antenna alignment in the considered bowtie arrays. The antenna spacing is $d_x = d_y = 1\,\text{m}$.

where the upper index denotes the matrix dimension and $r < \min(k, l)$ is the effective rank of $\mathbf{Z}_{n,m}^{k\times l}$. The computation of $\mathbf{R}$ and $\mathbf{C}$ is described in [33]. Again, a user-defined threshold is employed in order to determine when the algorithm has reached convergence.

2.3 Implementation

The block toeplitz symmetry existing for finite arrays with uniform spacing can be exploited to reduce the number of sub-blocks that needs to be computed. Additionally, reciprocity allows us to discard the calculation of the lower triangular area of the total MoM matrix. In a nutshell, for a $N_x \times N_y$ uniform array it is only necessary to compute $N_xN_y + (N_x - 1)(N_y - 1)$ number of sub-blocks. For example, for a 100×10 array we compute 1891, less than 0.2 %, of the actual existing 10^6 sub-blocks.

The code is implemented in the C programming language and uses the Intel MKL library [17]. Conceptual simulations were run on an Intel(R) Core(TM) i7-4770 CPU @ 3.4 GHz with 32 GB RAM, and the overall gain in computation time of the in-house hybridized MoM can be seen in Table 1. All simulations were run for uniform bowtie arrays configured as in Fig. 1, with 643 RWGs/element and 23 MBFs/element. The bowtie element has a height of $h = 1\,\text{m}$, a width of $w = 0.75\,\text{m}$ and a center width of $w_\text{c} = 0.05\,\text{m}$. The antenna spacing is $d_x = d_y = 1\,\text{m}$. The obtained scattering matrix from the in-house hybridized MoM is compared to that from FEKO in Fig. 2 for a 2×1 bowtie array.

2.4 Calculation of Embedded Element Pattern

In the case of non-contacting antenna elements, the currents on each element are expressed using the same set of MBFs. To benefit from this, the total far field for the array can be retrieved in an efficient manner by pre-computing the

Table 1: Time to generate and solve the system of equations using the in-house full wave solver for various array configurations of bowties as in Fig. 1b.

Config.	RWGs	Full	MBF+ACA	w.Toeplitz
8×3	15 432	242.0 s	6.6 s	1.6 s
100×10	643 000	N/A	5798.0 s	98 s

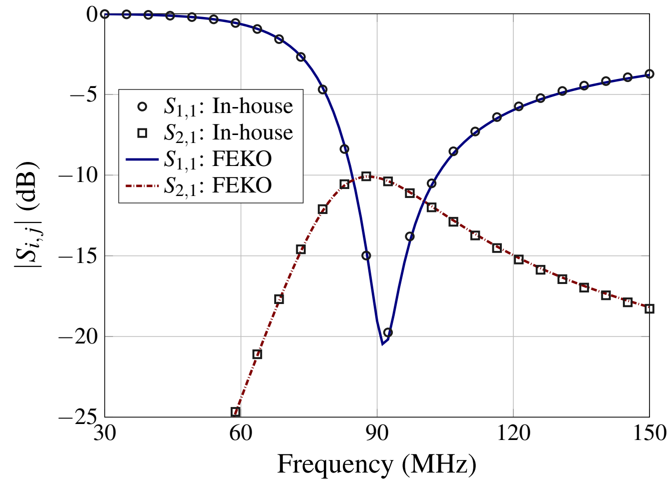

Figure 2: Scattering matrix simulation comparison of the in-house code with FEKO for a 2×1 array of the bowtie geometry in Fig. 1a with $d = 1\,\mathrm{m}$.

far field $\boldsymbol{F}^{\mathrm{mbf}}(\theta_{\mathrm{e}},\phi)$ from the expansion coefficients that constitutes the MBFs. Here, θ_{e} and ϕ denote the elevation and azimuth angle, respectively. For a given excitation, $\boldsymbol{F}^{\mathrm{mbf}}(\theta_{\mathrm{e}},\phi)$ is spatially translated for every antenna and weighted accordingly with the corresponding currents on that element. For M number of MBFs and N_{rwg} number of RWGs on one antenna, the far field from the MBFs is

$$\begin{aligned}&\boldsymbol{F}_m^{\mathrm{mbf}}(\theta_{\mathrm{e}},\phi)=\sum_{n=1}^{N_{\mathrm{rwg}}}u_{n,m}\boldsymbol{F}_n^{\mathrm{rwg}}(\theta_{\mathrm{e}},\phi),\\&m=1,\ldots,M.\end{aligned}\tag{2.4}$$

Here, $u_{n,m}$ is the corresponding matrix element of $\mathbf{U}$ in (2.2) and $\boldsymbol{F}_n^{\mathrm{rwg}}(\theta_{\mathrm{e}},\phi)$ is the far field from the n:th RWG. The total far field is then

$$\boldsymbol{F}(\theta_{\mathrm{e}},\phi)=\sum_{n=1}^{N}\sum_{m=1}^{M}I_{n,m}\boldsymbol{F}_m^{\mathrm{mbf}}(\theta_{\mathrm{e}},\phi)\mathrm{e}^{\mathrm{j}k(ux_n+vy_n)}\tag{2.5}$$

where $(u,v)=(\cos\theta_{\mathrm{e}}\cos\phi,\cos\theta_{\mathrm{e}}\sin\phi)$, $k=2\pi f/c$ is the wavenumber, and (x_n,y_n) is the position and $I_{n,m}$ is the m:th MBF current of the n:th antenna. The speed of light in air is c. The embedded element pattern (EEP) refers here to the far field pattern obtained when element n is excited and all other elements are terminated by a reference impedance [30]. Since the EEP needs to be computed for every existing antenna in the array, this processing becomes very time demanding when N grows large. The MBF approach facilitates this calculation and speeds up the entire process.

3 Metrics

An appropriate measure of the frequency bandwidth and radiation performance of a multiport system is the TARC [23]:

$$\mathit{\Gamma}_{\mathrm{tot}}^{\mathrm{a}}=\sqrt{\frac{\sum_{n=1}^{N}|b_n|^2}{\sum_{n=1}^{N}|a_n|^2}}.\tag{3.1}$$

Here, $N=N_xN_y$ is the total number of ports, and b_n and a_n represent the backward- and forward-propagating wave in port n, respectively. The waves $\boldsymbol{a}=[a_1,\ldots,a_N]^{\mathrm{T}}$ and $\boldsymbol{b}=[b_1,\ldots,b_N]^{\mathrm{T}}$ are related through the scattering matrix as

$$\boldsymbol{b}=\mathbf{S}\boldsymbol{a},\tag{3.2}$$

and we can hence express the backward-propagating wave in port m as

$$b_m=\sum_{n=1}^{N}S_{m,n}a_n.\tag{3.3}$$

The active reflection coefficient (ARC) [16, 23] can be used to consider only a single port n:

$$\mathit{\Gamma}_n^{\mathrm{a}} = \frac{b_n}{a_n}. \tag{3.4}$$

Evidently, the TARC represents the overall matching under a single frequency excitation, while the ARC allows us to study the matching at each antenna.

The scattering matrix $\mathbf{S}_0$ for a default characteristic impedance, e.g., $Z_0 = 50\,\Omega$, can be transformed to any characteristic impedance Z_{c}. For an arbitrary Z_{c} the voltages and currents in the ports are [27]:

$$\begin{aligned} \boldsymbol{V} &= \boldsymbol{a} + \boldsymbol{b} \\ \boldsymbol{I} &= (\boldsymbol{a} - \boldsymbol{b})/Z_{\mathrm{c}}. \end{aligned} \tag{3.5}$$

Using (3.2) and (3.5) then gives that

$$\mathbf{S} = (\mathbf{I} + Z_{\mathrm{c}}\mathbf{Y})^{-1}(\mathbf{I} - Z_{\mathrm{c}}\mathbf{Y}), \tag{3.6}$$

where $\mathbf{Y}$ denotes the admittance matrix, defined by $\boldsymbol{I} = \mathbf{Y}\boldsymbol{V}$. Note the difference between the port current vector $\boldsymbol{I}$ and the identity matrix $\mathbf{I}$. Solving (3.6) for a given default characteristic impedance, $Z_{\mathrm{c}} = Z_0$, and the corresponding scattering matrix $\mathbf{S}_0$ gives:

$$\mathbf{Y} = \frac{1}{Z_0}(\mathbf{I} + \mathbf{S}_0)^{-1}(\mathbf{I} - \mathbf{S}_0). \tag{3.7}$$

The scattering matrix can then be scaled from Z_0 in all ports to Z_{c} in all ports by insertion of $\mathbf{Y}$ into (3.6):

$$\mathbf{S} = (\mathbf{I} + \mathit{\Gamma}\mathbf{S}_0)^{-1}(\mathit{\Gamma}\mathbf{I} + \mathbf{S}_0). \tag{3.8}$$

Here, the reflection coefficient $\mathit{\Gamma} = (1 - Z_{\mathrm{c}}/Z_0)/(1 + Z_{\mathrm{c}}/Z_0)$ has been introduced. Consequently, only one full-wave simulation is necessary for a given geometry using the default characteristic impedance, and any impedance scaling can then be performed in post process by manipulating $\mathbf{S}$ using (3.8).

The radiated power per transverse row of the array is

$$P_{\mathrm{rad}}(n_x) = \frac{1}{2Z_{\mathrm{c}}} \sum_{n_y=1}^{N_y} |a_{n_x,n_y}|^2 - |b_{n_x,n_y}|^2, \tag{3.9}$$

where n_x and n_y are the longitudinal index in direction $\hat{x}$ and transverse index in direction $\hat{y}$ of antenna n, respectively. The cumulative distribution of radiated power can then be defined as

$$\Phi(n_x) = \frac{1}{P_{\mathrm{rad}}^{\mathrm{tot}}} \sum_{i=n_x}^{N_x} P_{\mathrm{rad}}(i). \tag{3.10}$$

Here, $P_{\mathrm{rad}}^{\mathrm{tot}}$ is the total radiated power of the array. Evidently, we get $\Phi(1) = 1$ when all transverse rows are included.

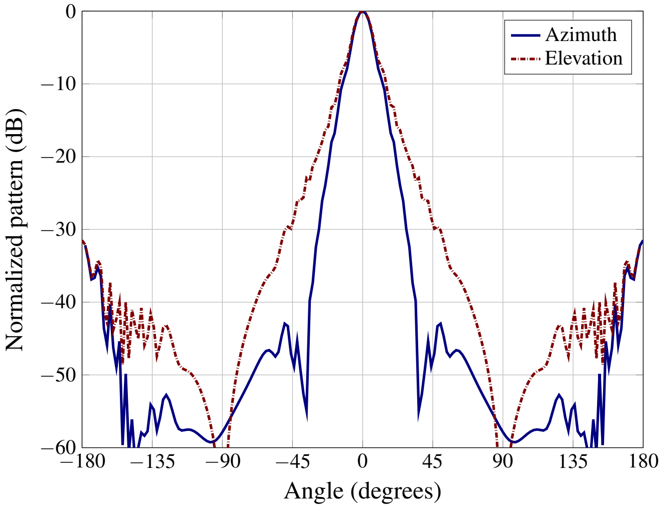

Figure 3: Normalized far field pattern for the 200×12 bowtie array at the array resonance ($f/f_0 = 0.26$) using the H-W excitation with $Z_\mathrm{c} = 50\,\Omega$.

4 Numerical Results

The in-house developed MoM solver was installed on an Intel(R) Xeon(R) CPU E5-2650 v3 @ 2.3 GHz with 128 GB RAM, and a 200×12 bowtie array with the previously introduced geometry and antenna spacing $d_x = d_y = 1\,\mathrm{m}$ was simulated. This spacing corresponds to a $\lambda/2$ displacement at $f_0 = 150\,\mathrm{MHz}$ where λ denotes the wavelength. Since the progressive phase shift feeding creates grating lobes at higher frequencies, the free space resonance of the element was chosen at the lower frequency 90 MHz, as shown in Fig. 2. Simulations were run for a set of linearly spaced discrete frequencies points ranging between 30 MHz and 150 MHz, or equivalently in the band $0.2 \le f/f_0 \le 1$, with the free space element resonance at $f = 90\,\mathrm{MHz}$ ($f/f_0 = 0.6$). The obtained input impedance is shown in Fig. 4 for a single bowtie element.

The bowtie geometry was chosen due to its bandwidth and its similarity with the versatile dipole geometry. With 643 RWGs/element the element itself is non-trivial and the total number of degrees of freedom exceeds $1.5 \cdot 10^6$. The total CPU time for a single frequency simulation, including calculation of the scattering matrix and $N = 2400$ number of EEPs, varied between 8 min 30 s and 27 min 20 s. This variation is due to the fact that the number of MBFs depends on frequency.

Fig. 5 shows two EEPs for the elements with indices (n_x, n_y) equal to $(100, 6)$ and $(200, 6)$. As seen, the pattern changes significantly depending on the element's position. The slight asymmetry in azimuth is explained by the even number of longitudinal rows.

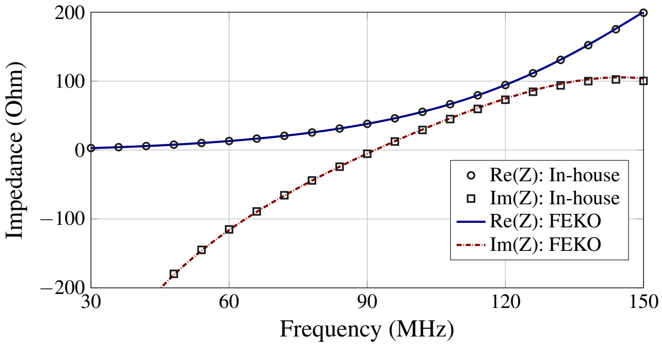

Figure 4: Input impedance for the bowtie geometry in Fig. 1a.

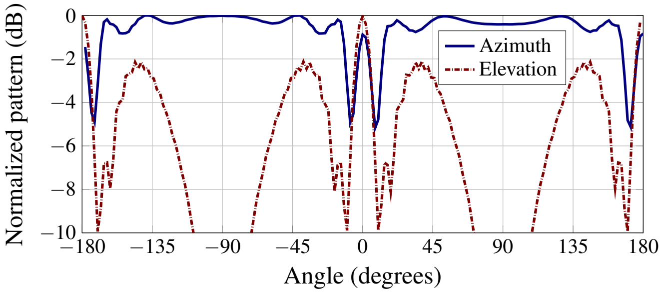

(a) $(n_x, n_y) = (100, 6)$.

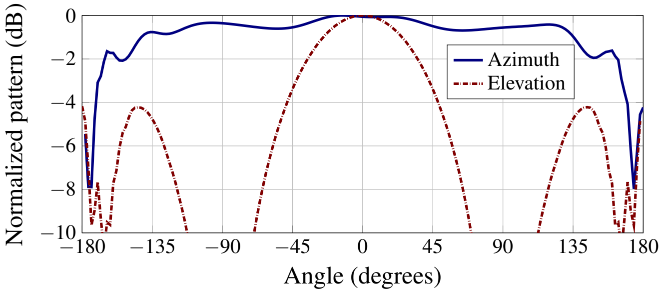

(b) $(n_x, n_y) = (200, 6)$.

Figure 5: Embedded element pattern (EEP) for bowtie elements with different positions in the 200×12 array.

4.1 Uniform Feeding

The classic H-W feeding approach [13] for endfire radiation corresponds to choosing a uniform amplitude and an incremental phase shift along the endfire direction $\hat{x}$ as

$$\varphi_x = -(kd_x + 2.94/N_x) \tag{4.1}$$

where d_x is the antenna spacing and N_x is the number of antennas in the longitudinal direction. The input waves are thus chosen as:

$$a_n = a_{n_x,n_y} = \mathrm{e}^{\mathrm{j}n_x\varphi_x}. \tag{4.2}$$

The H-W excitation provides a rough estimate to the beam widths and side lobe levels that can then be used as constraints to the convex optimization routine when applied to an array of a certain size. Fig. 3 shows the far field pattern for the 200×12 bowtie array at $f/f_0 = 0.26$ with $Z_\mathrm{c} = 50\,\Omega$. As seen, this excitation results in a clear main lobe in endfire. However, the overall matching is far from optimum. This problem is addressed in Section 4.2.

4.2 Matching Enhancement Using Pattern Synthesis

We address the problem of achieving a desired far field pattern with an endfire launched mode, while simultaneously minimizing the total reflected power in all ports in the array. The latter can be quantified by the TARC in (3.1). As in prior convex problem formulations for pattern synthesis [25,31], constraints can be put on the side lobe level and the solid angle of the main lobe. CVX, a matlab toolbox package for specifying and solving convex formulated problems [9,10] was used for all the results provided in this paper. The forward-propagating waves $\{a_n\}_{n=1}^{N}$ are used as degrees of freedom, and the problem is formulated to minimize the power reflected in the ports according to

$$\begin{array}{ll} \text{min.} & \sum_{n=1}^{N} |b_n|^2 = ||\mathbf{S}\boldsymbol{a}||_2^2 \\ \text{s. t.} & F(\theta_0,\phi_0) = 1, \quad \max\limits_{(\theta_\mathrm{e},\phi)\notin\Omega_0} |F(\theta_\mathrm{e},\phi)| \leq F_0. \end{array} \tag{4.3}$$

Here, $F(\theta_0, \phi_0)$ is the far field amplitude in elevation angle θ_0 and azimuth angle ϕ_0, F_0 is a specified side lobe level, and Ω_0 is the main lobe solid angle. The symmetry of the array allows us to enforce symmetric feeding of the different ports, e.g., for a $N_x \times N_y$ array the set of input waves at the longitudinal array with $n_y = 1$ is enforced to the longitudinal array with $n_y = N_y$ and so on. The number of degrees of freedom are thereby reduced by a factor of 2.

The optimization routine in (4.3) was first run independently for each discrete frequency point in the band. The main lobe solid angle Ω_0 is $(\theta_0 \pm 70^\circ, \phi_0 \pm 30^\circ)$ and the side lobe level $F_0 = -35\,\mathrm{dB}$ in order to accommodate the performance of the array under the H-W excitation (see Fig. 3). Note that Ω_0 does not correspond to the half-power beamwidth, but is chosen to comply with the width

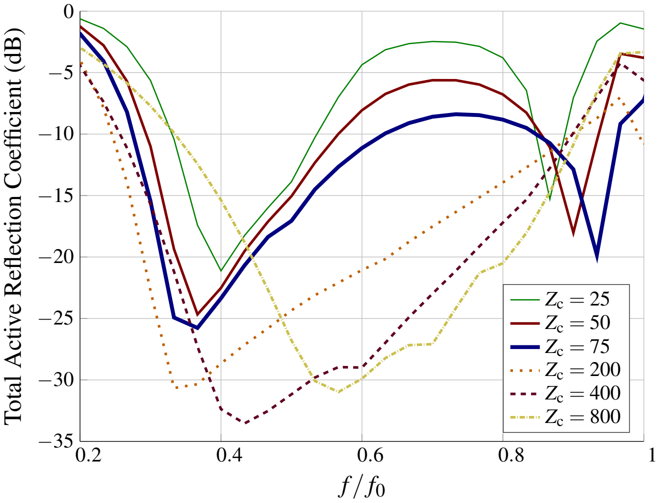

Figure 6: TARC over frequency for the 200 × 12 bowtie array using different characteristic impedances Z_c.

of the beam at the side lobe level defined by F_0. The obtained TARC for different characteristic impedances Z_c is shown in Fig. 6. A shift of the resonance of the array can be observed as Z_c increases, but most notable is the increase of the array's bandwidth and the improved matching. For $Z_\mathrm{c} = 400\,\Omega$, the $-10\,\mathrm{dB}$ bandwidth is $96\,\mathrm{MHz}$ in the range $0.26 \leq f/f_0 \leq 0.9$, and $\mathit{\Gamma}^\mathrm{a}_\mathrm{tot} = -33\,\mathrm{dB}$ at $f/f_0 = 0.43$. Referring to Fig. 4, it can be observed that in this region the bowtie element is capacitive with $\mathrm{Im}(Z) \simeq -100\,\Omega$ (in relation to the improved matching for higher Z_c). It is evident that a high capacitive load is beneficial, but no direct relation between the antenna impedance and the optimum Z_c can be distinguished. By inspection of the optimization data output, the smaller resonance close to $f/f_0 = 1$ was regarded to be less useful. Fig. 7 shows the far field pattern at $f/f_0 = 0.43$ with $Z_\mathrm{c} = 400\,\Omega$, and it shows close resemblance to the pattern obtained with the H-W excitation that is shown in Fig. 3.

Fig. 8 shows the ARC for different longitudinal rows, i.e., different transversal indices n_y, obtained using the convex optimization routine and the H-W excitation. The ARC obtained using the convex optimization routine decreases exponentially as the longitudinal index increases, and it stagnates at $-35\,\mathrm{dB}$ in the center of the array. There is no distinguishable difference of the ARC between different transversal indices. The ARC obtained using the H-W excitation is distinctly higher and shows a strong variation with respect to both the longitudinal index and transversal index.

Fig. 9 shows the normalized power of the input waves obtained using the convex optimization routine. The normalized power of the input waves increases exponentially towards the end of the array, and there is a 40 dB difference bet-

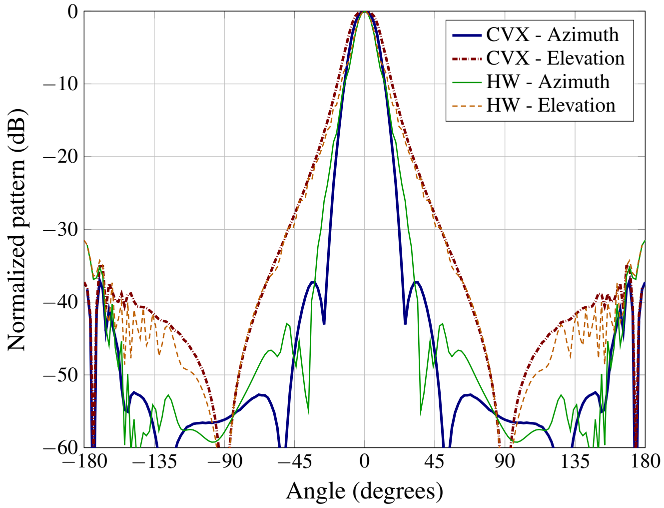

Figure 7: Normalized far field pattern for the 200 × 12 bowtie array at $f/f_0 = 0.43$ using the convex optimization routine. The characteristic impedance is $Z_c = 400\,\Omega$. The thinner graphs depict the far field pattern using the H-W excitation as shown in Fig. 3.

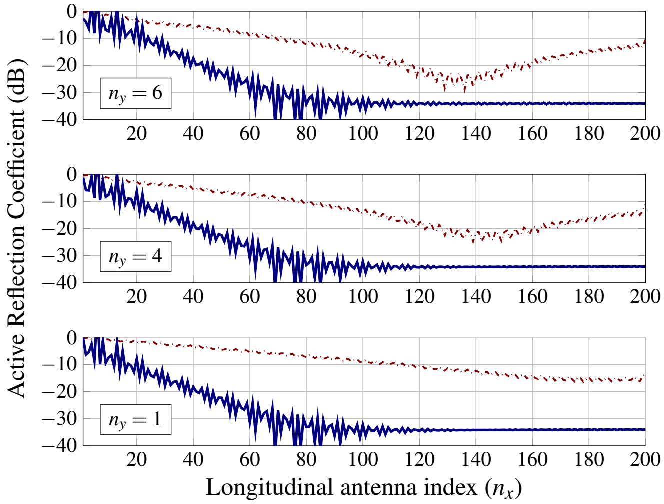

Figure 8: ARC as a function of the longitudinal index n_x for different transversal indices n_y. The solid line depicts the ARC at $f/f_0 = 0.43$ using the convex optimization scheme with $Z_c = 400\,\Omega$, and the dashed line depicts the ARC at $f/f_0 = 0.26$ using the H-W excitation with $Z_c = 50\,\Omega$.

ween the power fed at $n_x = 1$ and at $n_x = 200$. Most power is fed in the central longitudinal rows of the array, and there is $\approx 5\,\mathrm{dB}$ less power in the outer lon-

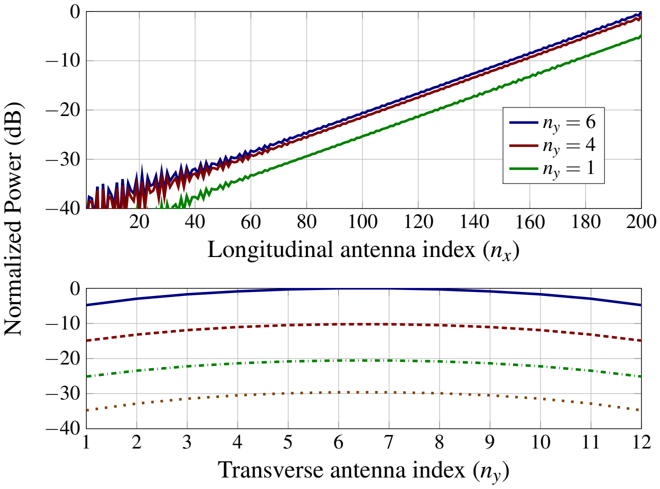

Figure 9: Normalized power of input waves as a function of the longitudinal index n_x (top), and as a function of the transverse index n_y for n_x = 50, 100, 150, and 200 in ascending order (bottom). The characteristic impedance is $Z_\mathrm{c} = 400\,\Omega$.

gitudinal rows. The phase of the input waves is depicted in Fig. 10, normalized with the phase obtained using the H-W excitation. Ignoring the difference at the first transversal rows where the input power is very small, a linear behaviour is observed. The phase difference is less than 180 ° over the entire array, which implies a small difference in the progressive phase shift. Further, an offset between the longitudinal rows is apparent and corresponds to approximately a 10 ° shift between the center- and the outer row.

Fig. 6 shows the TARCs obtained when the optimization routine was employed at each discrete frequency, independent of the excitation at adjacent frequencies. As a consequence, the optimum $\boldsymbol{a}$ is allowed to have rapidly fluctuating phase across the frequency band at every port. In fact, a closer inspection of the obtained solutions at frequencies in the outer edges of the band reveals that those far field patterns are distorted and not similar to the pattern obtained at the center frequency. Despite the good match for $0.26 \leq f/f_0 \leq 0.9$, the solutions are somewhat impractical.

A more functional formulation is introduced by restricting the phase variation over frequency with respect to the resonance frequency of the array f_c at each port n,

$$a_n(f) = a_n(f_\mathrm{c})\mathrm{e}^{-\mathrm{j}(k-k_\mathrm{c})n_x d_x}, \tag{4.4}$$

which eliminates this randomness. Here, k_c denotes the free space wavenumber at frequency f_c.

A second set of solutions was obtained using (4.4) with $f_\mathrm{c}/f_0 = 0.43$ and $Z_\mathrm{c} = 400\,\Omega$. Fig. 11 shows the achieved TARC for the 200 × 12 bowtie array using the two convex optimization routines and the H-W excitation. The −10 dB

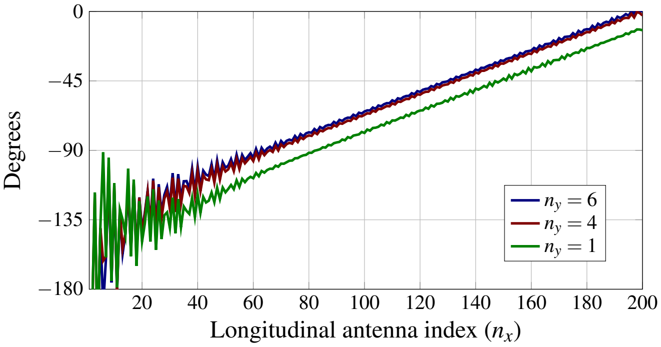

Figure 10: Input wave phase as a function of the longitudinal antenna index n_x when normalized with the phase obtained using the H-W excitation. The characteristic impedance is $Z_\mathrm{c} = 400\,\Omega$.

bandwidth is 35 MHz for the dependent frequency scheme, which corresponds to a fractional bandwidth of 54 %. Due to the enforced linear frequency-dependency under this excitation, a stable far field is obtained across the band resembling the pattern at $f = f_\mathrm{c}$.

The fractional bandwidth is smaller than for the independent frequency scheme, yet significantly improved with respect to the narrow bandwidth obtained using the H-W excitation. The H-W excitation results in a narrow bandwidth and a TARC that never sinks below −10 dB regardless of the choice of Z_c.

4.3 Performance of Different Array Configurations

The method used to obtain the results presented above can be described as a step-by-step procedure:

1. Choose constraints on side lobe level F_0 and main lobe solid angle Ω_0 in accordance to the performance of the array under the H-W excitation.
2. For all values of characteristic impedance Z_c, execute the convex optimization routine across the frequency band of interest.
3. Find the resonance frequency f_c of the array for the appropriate choice of Z_c.
4. Employ the dependent frequency excitation based on f_c using (4.4).
5. Generate the desired results, e.g., TARC, input waves, far field patterns and cumulative distribution of radiated power Φ.

The method was employed to three array configurations of the bowtie, a 50 × 12 array, a 100 × 12 array and a 200 × 12 array, and the optimization settings and performance output are displayed in Table 2. The bandwidth is not sensitive to

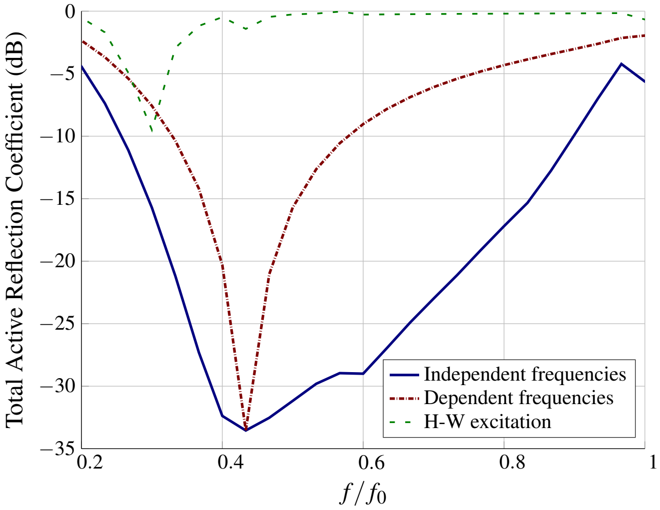

Figure 11: TARC for the convex optimization routines using dependent- and independent frequencies with $Z_\mathrm{c} = 400\,\Omega$, and the H-W excitation with $Z_\mathrm{c} = 50\,\Omega$.

the array size, but a moderate shift of the resonance of the array can be observed. The exponential increase in input wave power is apparent for all configurations under the optimized excitation.

Fig. 12 shows the cumulative distribution of radiated power. The uniform distribution of transmit power across any array under the H-W excitation results in a linear relation, as depicted in the figure. As the array size decreases, a larger fraction of the array is responsible for the same fraction of radiated power. Interestingly, the results suggest that despite the difference in array size, the radiated power originates mainly from the final fraction of transverse rows of the array. In particular, for the 200×12 array $6\,\%$ of the radiated power originates from the last transverse row ($n_x/N_x = 1$), and approximately $90\,\%$ of the radiated power originates from the last 50 transverse rows ($n_x/N_x = 0.75$). However, the first 100 transverse rows contributes to less than $1\,\%$ of the radiated power.

4.4 Truncated Optimized Excitation

The retrieved cumulative distribution curves was an incentive to truncate the retrieved input waves from the optimization of the 200×12 array such that $a_{n_x,n_y} = 0$ for all $n_x < 150$ and check the impact of the modified excitation. The far field pattern is shown in Fig. 13, and the TARC is shown in Fig. 14. The truncation corresponds to an overall reduction of the radiated power by $10\,\%$ ($1\,\mathrm{dB}$). The power in the main lobe direction is $2.5\,\mathrm{dB}$ lower than if the full excitation is used (all ports active), which means that an additional $1.5\,\mathrm{dB}$ power is lost in the endfire direction. Some ripples are introduced, but the far

Table 2: Performance for different bowtie array configurations. F_0 denotes the side lobe level, Ω_0 the main lobe solid angle, Z_c the characteristic impedance, and BW the $-10\,\mathrm{dB}$ fractional bandwidth. HPBW denotes the half-power beamwidth in elevation. The $\lambda/2$-displacement frequency is $f_0 = 150\,\mathrm{MHz}$.

Config.	F_0	Ω_0	Z_c	f/f_0	BW	HPBW
50×12	$-25\,\mathrm{dB}$	$(\theta_0 \pm 60°, \phi_0 \pm 25°)$	$200\,\Omega$	0.47	53 %	30°
100×12	$-30\,\mathrm{dB}$	$(\theta_0 \pm 65°, \phi_0 \pm 25°)$	$400\,\Omega$	0.53	55 %	22°
200×12	$-35\,\mathrm{dB}$	$(\theta_0 \pm 70°, \phi_0 \pm 30°)$	$400\,\Omega$	0.43	53 %	18°

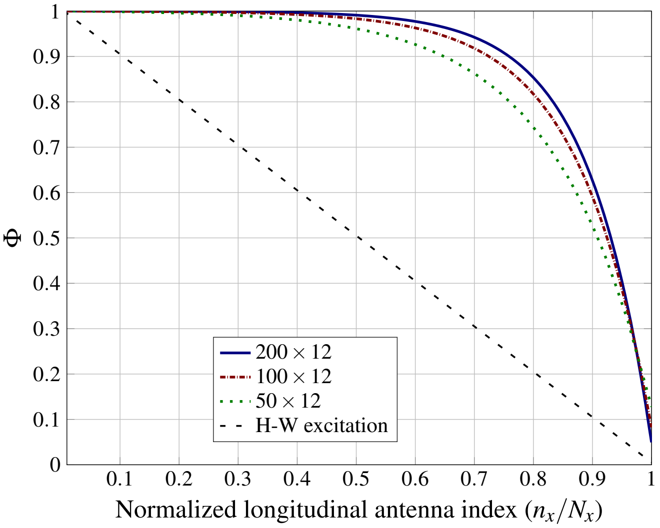

Figure 12: The cumulative distribution of radiated power for different array configurations using the optimized excitation and the H-W excitation.

field pattern is relatively well-preserved. A shift of the center frequency can be observed in Fig. 14; however, the $-10\,\mathrm{dB}$ bandwidth is not compromised and the performance is still improved with respect to the array's performance under the H-W excitation.

5 Discussion

The results suggest that the optimum excitation is found by exponentially increasing the power to the antennas as the longitudinal index increases. In fact, for the 200×12 array approximately 90 % of the radiated power originated from the last 50 transverse rows of the array, and the first 100 transverse rows contributed to less than 1 % of the radiated power. The exponential increase in feed power occurred for various array sizes, which implies that, for large enough arrays, me-

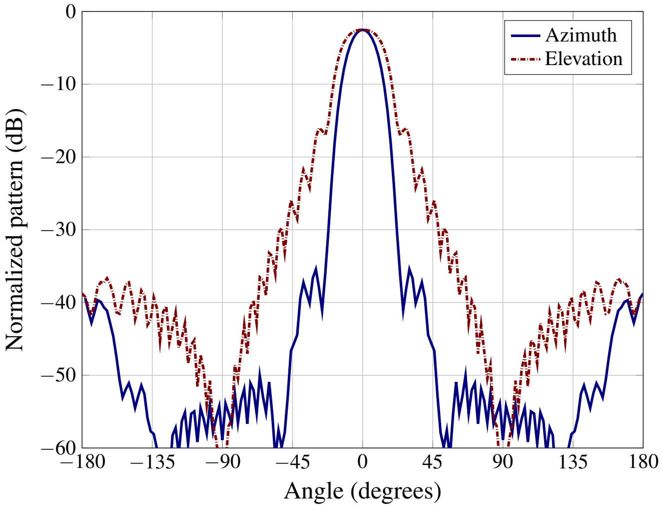

Figure 13: Normalized far field pattern for the 200 × 12 bowtie array when the optimized excitation is truncated such that $a_{n_x,n_y} = 0$ for all $n_x < 150$. The far field is normalized with respect to the maximum value using the optimized excitation of all ports.

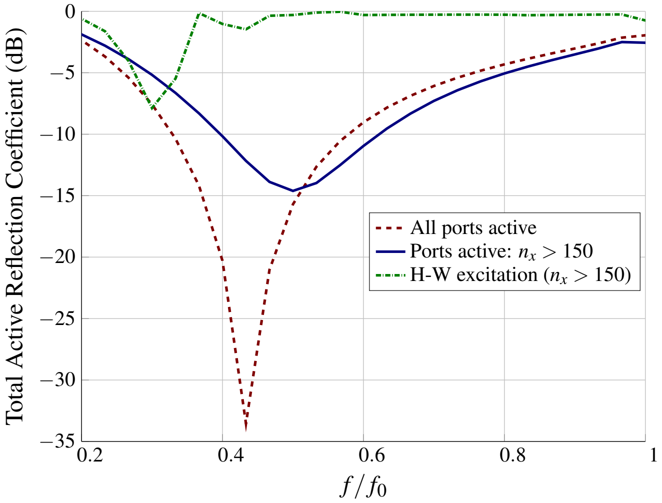

Figure 14: TARC for the 200 × 12 bowtie array using different excitation configurations. The optimized excitation is truncated such that $a_{n_x,n_y} = 0$ for all $n_x < 150$. The H-W excitation is applied to ports with $n_x > 150$.

rely a fraction of the antennas in the array needs to be excited in order to obtain good endfire performance. Interestingly, these results are in relationship with classical findings; tapering of the excitation amplitude can be used as a means to control the trade off between optimized side lobe level and beamwidth [5, 29].

The truncated excitation of the 200×12 array resulted in a well-preserved far field pattern and maintained bandwidth, yet some degraded performance with respect to the achieved gain in the endfire direction could be observed. From an engineering perspective, it can be argued that only operating a fraction of the array is beneficial on a system level if the loss in gain is acceptable. If the complete array were to be used in endfire mode, it would require transmit/receive (T/R) modules (assumed identical for all ports) with a dynamic range of 40 dB as seen in Fig. 9. Since, however, the majority of the radiated power originates from the last quarter of the array, the dynamic range of the T/R modules can be limited to 15 dB if only these rows are utilized. The nice linear behaviour of the input phase, as seen in Fig. 10, can also be deemed practical.

6 Conclusions

This paper presents an approach that utilizes convex optimization to optimize the matching of endfire antenna arrays. As in former adaptations of convex optimization to pattern synthesis problems, constraints can be put on the side lobe levels and the main lobe beamwidth. Simulations were efficiently run using an in-house full wave solver developed for the purpose of treating electrically large arrays, and numerical results were provided for a 200×12 bowtie array. The optimization routine was first employed independently at each discrete frequency point, and it was found that a significantly improved matching could be obtained in comparison to the matching obtained with the H-W excitation. Furthermore, the impact of the characteristic impedance on the TARC could be studied through the use of efficient post processing routines.

The optimization scheme was modified by restricting the phase variation over frequency at each antenna port. This resulted in a smaller bandwidth, yet significantly improved compared to the H-W excitation, and it provided stable results with respect to the obtained far field patterns across the whole band.

The presented results illustrate the versatile applicability of the utilized convex optimization formulation.

Future work includes a more extensive theoretical analysis of the results. In particular, the relation between excitation frequency, various parameters of the array configuration and the exponential increase in feed power along the longitudinal direction will be studied. Also, the optimum choice of characteristic impedance will be further examined.

Acknowledgment

The authors would like to thank Anders Höök, Glenn Sjöberg and Kent Falk at Saab Electronic Defence Systems, and Erik Abenius and Bo Strand at ESI group for helpful discussions.

References

[1] C. A. Balanis. *Antenna Theory.* John Wiley & Sons, New York, NY, second edition, 1997.

[2] M. Bebendorf. Approximation of boundary element matrices. *Numerische Mathematik*, **86**(4), 565–589, 2000.

[3] S. P. Boyd and L. Vandenberghe. *Convex Optimization.* Cambridge Univ. Pr., 2004.

[4] C. Craeye, J. Laviada, R. Maaskant, and R. Mittra. Macro basis function framework for solving maxwells equations in surface integral equation form. *The FERMAT Journal*, **3**, 1–16, 2014.

[5] C. L. Dolph. A current distribution for broadside arrays which optimizes the relationship between beam width and side-lobe level. *Proc. IRE*, **34**(6), 335–348, June 1946.

[6] E. C. Dufort. Pattern synthesis based on adaptive array theory. *IEEE Trans. Antennas Propag.*, **37**(8), 1011–1018, 1989.

[7] A. B. Gershman, N. D. Sidiropoulos, S. Shahbazpanahi, M. Bengtsson, and B. Ottersten. Convex optimization-based beamforming. *IEEE Signal Process. Mag.*, **27**(3), 62–75, 2010.

[8] W. C. Gibson. *The Method of Moments in Electromagnetics*, volume 1. Chapman & Hall/CRC London, UK, 2008.

[9] M. Grant and S. Boyd. Graph implementations for nonsmooth convex programs. In V. Blondel, S. Boyd, and H. Kimura, editors, *Recent Advances in Learning and Control*, Lecture Notes in Control and Information Sciences, pages 95–110. Springer-Verlag Limited, 2008.

[10] M. Grant and S. Boyd. CVX: Matlab software for disciplined convex programming, version 1.21. `http://cvxr.com/cvx`, April 2011.

[11] M. Gustafsson and S. Nordebo. Optimal antenna currents for Q, superdirectivity, and radiation patterns using convex optimization. *IEEE Trans. Antennas Propag.*, **61**(3), 1109–1118, 2013.

[12] M. Gustafsson, M. Cismasu, and S. Nordebo. Physical bounds on small antennas as convex optimization problems. In *IEEE Antennas and Propagation Society International Symposium*, pages 1–2. IEEE, 2012.

[13] W. W. Hansen and J. R. Woodyard. A new principle in directional antenna design. *Proc. IRE*, **26**(3), 333–345, 1938.

[14] J. Helander, D. Sjöberg, and D. Tayli. On the issue of simulating very large endfire arrays with complex antenna geometries. In *Proc. URSI Int Electromagnetic Theory (EMTS) Symp*, pages 737–740, 2016.

[15] J. Helander, D. Tayli, and D. Sjöberg. A comparison of macro basis function methods for interconnected endfire antenna arrays. *IEEE Antennas Wireless Propag. Lett.*, 2017.

[16] IEEE145-1993. *IEEE Standard Definition of Terms for Antennas.* Antenna Standards Committee of the IEEE Antennas and Propagation Society, March 1993.

[17] Intel. Intel Math Kernel Library 2017 update 3. `https://software.intel.com/en-us/mkl`, 2017. Accessed: 2017-12-20.

[18] R. W. P. King and S. S. Sandler. The theory of endfire arrays. *IEEE Trans. Antennas Propag.*, **12**(3), 276–280, 1964.

[19] H. Lebret and S. Boyd. Antenna array pattern synthesis via convex optimization. *IEEE Trans. Signal Process.*, **45**(3), 526–532, 1997.

[20] Y. Lo, S. Lee, and Q. Lee. Optimization of directivity and signal-to-noise ratio of an arbitrary antenna array. *IEE Proceedings*, **54**(8), 1033–1045, 1966.

[21] E. Lucente, A. Monorchio, and R. Mittra. An iteration-free MoM approach based on excitation independent characteristic basis functions for solving large multiscale electromagnetic scattering problems. *IEEE Trans. Antennas Propag.*, **56**(4), 999–1007, 2008.

[22] R. Maaskant, R. Mittra, and A. Tijhuis. Fast analysis of large antenna arrays using the characteristic basis function method and the adaptive cross approximation algorithm. *IEEE Trans. Antennas Propag.*, **56**(11), 3440–3451, 2008.

[23] M. Manteghi and Y. Rahmat-Samii. Multiport characteristics of a wideband cavity backed annular patch antenna for multipolarization operations. *IEEE Trans. Antennas Propag.*, **53**(1), 466–474, jan 2005.

[24] A. Massa, P. Rocca, and G. Oliveri. Compressive sensing in electromagnetics-a review. *IEEE Antennas Propag. Mag.*, **57**(1), 224–238, 2015.

[25] S. E. Nai, W. Ser, Z. L. Yu, and H. Chen. Beampattern synthesis for linear and planar arrays with antenna selection by convex optimization. *IEEE Trans. Antennas Propag.*, **58**(12), 3923–3930, 2010.

[26] S. Nordebo, M. Gustafsson, B. Nilsson, and D. Sjöberg. Optimal realizations of passive structures. *IEEE Trans. Antennas Propag.*, **62**(9), 4686–4694, 2014.

[27] D. M. Pozar. *Microwave Engineering.* John Wiley & Sons, New York, NY, third edition, 2005.

[28] V. V. S. Prakash and R. Mittra. Characteristic basis function method: A new technique for efficient solution of method of moments matrix equations. *Microwave and Optical Technology Letters*, **36**(2), 95–100, 2003.

[29] S. A. Schelkunoff. A mathematical theory of linear arrays. *Bell Labs Technical Journal*, **22**(1), 80–107, 1943.

[30] W. L. Stutzman and G. A. Thiele. *Antenna Theory and Design.* John Wiley & Sons, New York, NY, second edition, 1998.

[31] H. Van Bui, S. N. Jha, and C. Craeye. Fast full-wave synthesis of printed antenna arrays including mutual coupling. *IEEE Trans. Antennas Propag.*, **64**(12), 5163–5171, 2016.

[32] T. Zhang and W. Ser. Robust beampattern synthesis for antenna arrays with mutual coupling effect. *IEEE Trans. Antennas Propag.*, **59**(8), 2889–2895, 2011.

[33] K. Zhao, M. N. Vouvakis, and J.-F. Lee. The adaptive cross approximation algorithm for accelerated method of moments computations of EMC problems. *IEEE Trans. Electromagn. Compat.*, **47**(4), 763–773, 2005.

A Comparison of Macro Basis Function Methods for Interconnected Endfire Antenna Arrays

Jakob Helander, Doruk Tayli, and Daniel Sjöberg

Paper V

Published as: J. Helander, D. Tayli, and D. Sjöberg, "A Comparison of Macro Basis Function Methods for Interconnected Endfire Antenna Arrays", *IEEE Antennas Wireless Propagation Letters*, Vol. 16, pp. 2159–2162, 2017.

Abstract

Two approaches to the macro basis function (MBF) method that target interconnected subdomains have been adapted to finite linear arrays, and benchmarked against each other in order to estimate their performance with respect to the strong near field coupling that occurs under the endfire mode operation. The methods, here referred to as method A and B, are based on the synthetic function- and characteristic basis function method respectively, presented in previous literature. The occurrence of very strong near field coupling can be seen to affect the number of MBFs required for a certain level of accuracy, although both approaches perform well under the test scenario. However, method B provides a considerable more efficient compression with respect to a maximum acceptable error level.

1 Introduction

The conventional method of moments (MoM) is a widely used full-wave analysis tool for electrically large or complex structures, which uses an integral equation to formulate the problem at hand. The memory allocation of standard MoM scales as $\mathcal{O}(N^2)$ for N degrees-of-freedom, and typically the Rao-Wilton-Glisson (RWG) [11] function is chosen as the local basis function. However, for large-scale problems N becomes exceedingly large, and it becomes necessary to adapt hybrid techniques in order to solve the problem in a time efficient manner using minimal memory usage [3].

A method that deals with this particular problem, although various other approaches also exist, is the MBF method. Using a subdomain-division of the complete geometry, the induced surface current on each subdomain is expressed through aggregated basis functions. A compressed version of the equation system is obtained, and the computation time and memory storage is consequently reduced. Numerous variations of the approach have been proposed; e.g., the characteristic basis function (CBF) method [2, 5, 7, 10], the synthetic function (SF) method [9] and the eigencurrent method [1]. The common concept of these is the same, whereas the differences lie in how to generate the MBFs.

For geometries where the partitioning results in contacting subdomains, the MBF method must allow a continuous current to flow between neighbouring regions. This needs to be modelled, and two alternative ways to do this are presented in [7] and [9] respectively. As the strength of the mutual coupling between contacting subdomains can vary, it is a legitimate question to ask whether a particular approach can maintain a certain accuracy in the approximate solution and simultaneously maintain a considerable reduction of the number of unknowns.

This work targets the adaptation of the MBF method to finite arrays with interconnected antenna elements, and studies the effect of exciting the endfire mode on the accuracy of the solution. The endfire excitation results in the main lobe being launched in the longitudinal direction of the array, and consequently very strong coupling between antenna elements will occur. Previous presented methods have not been studied under this extreme condition, and we aim here to provide a comparison of different approaches in this respect. Two methods to treat the interconnection problem, compression method A and B based on the methods in [9] and [7] respectively, are analyzed. While this study only considers finite arrays, both methods can be applied to more general geometries of arbitrary complexity [2, 9]. The performances are evaluated using two measures: (1) Relative error of the retrieved current, and (2) the compression ratio for a given maximum value of the relative error. Results are provided for arrays consisting of two different antenna geometries. Notably, the only difference between method A and B will be the procedure of treating the interconnection between subdomains.

2 Macro Basis Functions

The original equation system in the RWG basis is described by the full MoM representation,

$$\mathbf{Z}\boldsymbol{I} = \boldsymbol{V}, \tag{2.1}$$

which can be divided into sub-blocks $\mathbf{Z}_{i,j}$ and $\boldsymbol{V}_i$, containing the coupling terms between subdomain i and j, and the excitation of subdomain i, respectively. The aim of the MBFs method is then to efficiently compress each block by utilizing an aggregated basis form instead of the local basis.

For clarity, we emphasize here the difference between the following terms: The domain considered when computing a set of MBFs is denoted the Domain under Excitation (DE); any domain on which a set of MBFs is employed is denoted a subdomain. Only linear finite arrays are considered here, but the procedure can easily be extended to the planar case, with the only effect being an increase in the number of DEs.

2.1 Generation of Excitation Space

Both investigated methods rely on computing the induced surface currents on the DE from a set of excitations. The resulting current vectors are computed as

$$\boldsymbol{r}_i = \mathbf{Z}_{\mathrm{DE}}^{-1}\boldsymbol{V}_{r,i}, \tag{2.2}$$

where $\boldsymbol{V}_{r,i}$ is the corresponding excitation for response i and $\mathbf{Z}_{\mathrm{DE}}$ is the moment matrix of the DE. For consistency, the same excitation approach will be employed in both methods.

First, each port in the DE is excited sequentially, as to generate the natural responses. Point dipoles located at a subset of the node coordinates of all subdomains adjacent to the DE are used as excitations to invoke a representation of induced currents due to near field coupling. This is illustrated in Fig. 1. Lastly, a set of plane wave excitations is used as far-distanced external sources. A total

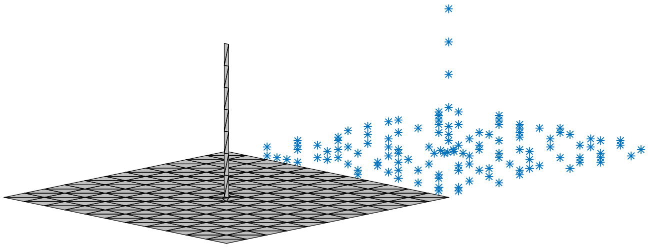

Figure 1: Illustration of near field coupling excitations for the edge element of a linear monopole array; the nodes of the adjacent subdomain are used as point dipole centers.

number of N_e responses are computed, and the response matrix

$$\mathbf{R} = \left[\begin{array}{cccc} \boldsymbol{r}_1, & \boldsymbol{r}_2, & \ldots, & \boldsymbol{r}_{N_e} \end{array} \right],$$

constituting of all N_e response vectors, is the foundation on which the set of MBFs will be based on.

2.2 General Macro Basis Function Approach

The MBFs are represented as column vectors of expansion coefficients, aggregating the RWGs on the DE. The coefficients are retrieved from $\mathbf{R}$ through a singular value decomposition (SVD),

$$\mathbf{R} = \mathbf{U}\boldsymbol{\Sigma}\mathbf{V}^{\mathrm{H}}, \tag{2.3}$$

where $\mathbf{U}$ and $\mathbf{V}$ are unitary matrices containing singular vectors, Σ is a diagonal matrix with the singular values σ in descending order as its diagonal entries, and superscript H denotes the Hermitian transpose. By discarding the singular vectors of $\mathbf{U}$ whose normalized singular values are below a certain prescribed threshold τ, we obtain the number of representative MBFs:

$$\sigma_m/\sigma_1 \geq \tau, \quad m = 1, 2, \ldots, M. \tag{2.4}$$

The initial orthonormal set of MBFs, acting on the *complete* DE, is then represented by the matrix $\widehat{\mathbf{U}}$, containing the M first columns of $\mathbf{U}$:

$$\widehat{\mathbf{U}} = \left[\begin{array}{cccc} \boldsymbol{u}_1, & \boldsymbol{u}_2, & \ldots, & \boldsymbol{u}_M \end{array} \right].$$

The size of $\widehat{\mathbf{U}}$ is $N_{\mathrm{rwg}}^{\mathrm{DE}} \times M$, for $N_{\mathrm{rwg}}^{\mathrm{DE}}$ number of RWGs on the DE. The final set of MBFs, acting only on a single subdomain, is represented by the matrix $\mathbf{A}$ which is selected as a segment of $\widehat{\mathbf{U}}$ according to the descriptions in Section 2.3 and 2.4 for the two methods respectively. With a set of MBFs expressed through a corresponding matrix $\mathbf{A}$ for each subdomain, the total system of equations can

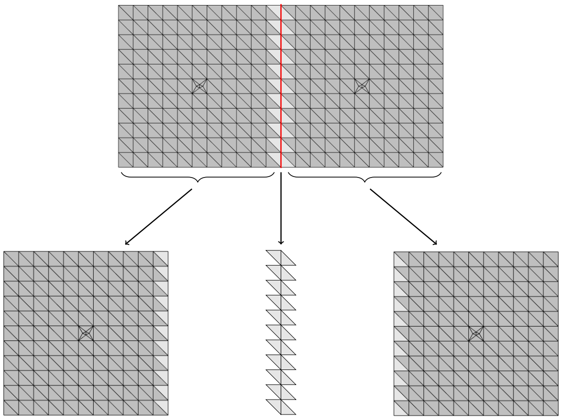

Figure 2: Geometrical sectioning for extracting DEs for MBF generation according to method A. The subdomain is extracted together with the corresponding HRWGs on its border (bottom left and right). The RWGs along the subdomain borders represent a separate subdomain (bottom center).

be reduced by block-wise compression of the subdomain coupling matrices and excitation vectors:

$$\begin{aligned}\mathbf{Z}_{i,j}^{\mathrm{MBF}} &= \mathbf{A}_i^{\mathrm{T}}\mathbf{Z}_{i,j}\mathbf{A}_j \\ \boldsymbol{V}_i^{\mathrm{MBF}} &= \mathbf{A}_i^{\mathrm{T}}\boldsymbol{V}_i \\ i = 1,2,\ldots,N_{\mathrm{sd}};& \quad j = 1,2,\ldots,N_{\mathrm{sd}}.\end{aligned} \tag{2.5}$$

Here, i and j are subdomain indices, superscript T denotes the transpose and a total of N_{sd} subdomains are assumed.

2.3 Compression Method A

The DE considered for generation of a subdomain's final set of MBFs is chosen as the subdomain itself. To avoid edge conformity and invoke current continuity, the enclosing RWGs are added on the border to the subdomain's neighbours. Recalling that an RWG is obtained by pairing up mesh-triangles, only the triangle maintained within the subdomain is included. This is referred to as an half-RWG (HRWG) in [9]. The response matrix $\mathbf{R}$ is then expanded to include excitation of the HRWGs. Moreover, $\mathbf{A}$ is extracted from $\widehat{\mathbf{U}}$ by removing the expansion coefficents for the HRWGs, and treating *all* RWGs along the subdomain borders as a *separate* subdomain. For N_{a} number of antennas in the array, the number of subdomains will then be $N_{\mathrm{sd}} = N_{\mathrm{a}} + 1$. Since no reduction of unknowns occurs on this final subdomain, for N_l number of RWGs on all borders, $\mathbf{A}$ is an identity matrix of size $N_l \times N_l$. The scheme is visualized in Fig. 2.

For a linear array, there are three DEs to consider; one for each edge element (one border present) and one for the centred elements (two borders present).

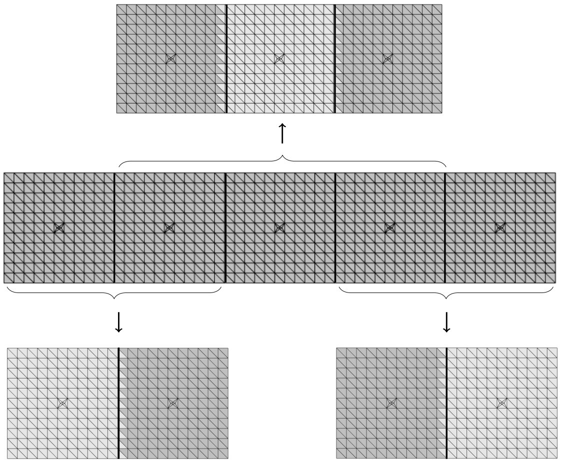

Figure 3: Geometrical sectioning for extracting DEs for MBF generation according to method B. For centered elements two neighbouring subdomains are included (top), for edge elements one neighbouring subdomain is included (below). The highlighted region denotes the region where the corresponding MBFs are employed.

2.4 Compression Method B

The DE considered for generation of a subdomain's final set of MBFs is chosen as the subdomain itself together with its closest neighbours. Again, there are three DEs to consider as illustrated in Fig. 3. A trapezoidal windowing function is employed on $\mathbf{R}$ prior to applying the SVD [6]:

$$\widehat{\mathbf{R}} = \mathbf{\Lambda}\mathbf{R}, \tag{2.6}$$

$$\widehat{\mathbf{R}} = \mathbf{U}\mathbf{\Sigma}\mathbf{V}^{\mathrm{H}}. \tag{2.7}$$

Here, $\mathbf{\Lambda}$ is a diagonal matrix with its entries being either 0, 1 or 0.5 depending on if the corresponding RWG lies outside or inside the subdomain, or on the border between two subdomains respectively. The weighting of 0.5 ensures a proper weight when the geometry is considered globally. The matrix $\mathbf{A}$, representing the final set of MBFs, is then selected as the truncated singular vectors in $\widehat{\mathbf{U}}$.

3 Numerical Results

Two 10×1 finite antenna arrays, a monopole array and a bowtie array, are considered in this section. The geometries are shown in Fig. 4, and the total number of RWGs are 7 938 and 3 769 respectively. The spacing is $d = 2\,\mathrm{m}$ for the monopole array and 2.4 m for the bowtie array. The monopole has a length of 1 m and a width of 0.04 m, and the bowtie has length $l = 2\,\mathrm{m}$, width $w = 2\,\mathrm{m}$, centerwidth $w_{\mathrm{c}} = 0.12\,\mathrm{m}$ and is placed 1 m above ground. The arrays

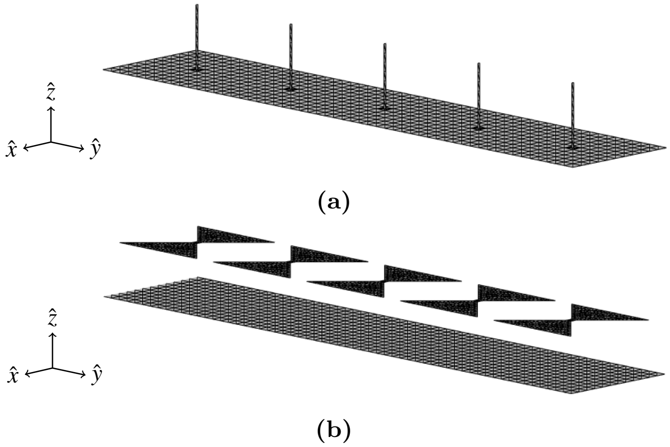

Figure 4: Five elements in the two 10×1 arrays under consideration: (a) monopole array, (b) bowtie array.

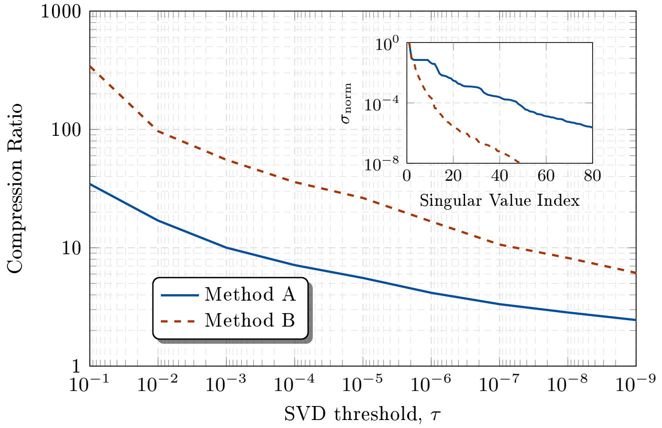

Figure 5: Compression ratio of the monopole array as a function of the SVD threshold. The subfigure shows the normalized singular values σ_{norm} for the singular value sequence.

are excited at frequency $f = 67.5\,\mathrm{MHz}$ using two progressive phaseshifts φ: $\varphi = 0$ for broadside mode operation, and $\varphi = -(kd + 2.94/N)$, the Hansen-Woodyard phaseshift [4], for endfire mode operation. The wavenumber $k = 2\pi f/\mathrm{c}$, $N = 10$ is the number of antennas and c is the speed of light in air. The algorithms are implemented in Matlab as add-ons to the source code provided in [8].

The accuracy is measured using the relative error of the current vectors in the L_2-norm, defined as:

$$\eta = \frac{||\boldsymbol{I}^{\mathrm{MBF}} - \boldsymbol{I}^{\mathrm{RWG}}||_2}{||\boldsymbol{I}^{\mathrm{RWG}}||_2}. \tag{3.1}$$

With an acceptable error level of 1 % ($\eta = 10^{-2}$), the maximum SVD thresholds for the two methods are determined: $\tau_{\mathrm{max,A}}$ and $\tau_{\mathrm{max,B}}$ respectively. The compression ratio (CR) is a measure of a method's compression efficiency,

$$\mathrm{CR} = \frac{N_{\mathrm{rwg}}^{\mathrm{tot}}}{\sum_{i=1}^{N_{\mathrm{sd}}} M_i}, \tag{3.2}$$

with M_i MBFs in subdomain i, and a total of $N_{\mathrm{rwg}}^{\mathrm{tot}}$ RWGs in the complete geometry.

The singular value sequence and the CR for the monopole array is shown in Fig. 5; the trend is similar for the bowtie array. Interestingly, the slope of the singular value sequence is substantially different for the two methods, and this characteristic directly reflects the obtained CR; method B corresponds to a larger reduction of unknowns with respect to a fixed threshold. Notably, the difference is not only a consequence of treating the border-RWGs as a separate subdomain in method A, which would generate a fixed gap between the curves. Thus, if $\tau_{\mathrm{max,A}} \approx \tau_{\mathrm{max,B}}$, the achieved compression using method B would be significantly greater which would result in a smaller final system of equations.

The computational complexity for generating the MBFs is greater for method B since the DEs, on which the SVD is performed, will incorporate neighbouring subdomains. Method B therefore requires the solution of a larger system of equations in (2.2). As the total size of the array grows however, the generation of the set of MBFs will constitute a smaller proportion of the total computation time.

As seen in Fig. 6 and Fig. 7 the endfire mode results in a larger error than the broadside mode for a given τ. This is to be expected, as the mutual coupling is more critical under this scenario. Both methods show little sensitivity with respect to the antenna geometry; however, a slight left-shift of the curves in Fig. 7 can be observed with respect to Fig. 6. Interestingly, a monotonic decrease is only observed for method A. It is seen that the required accuracy is achieved at a lower threshold with method B than for method A, with $\tau_{\mathrm{max,B}} \simeq 10^{-5}$ and $\tau_{\mathrm{max,A}} \simeq 10^{-6}$ in both examples. For the monopole, this corresponds to $\mathrm{CR_B} \approx 25$ and $\mathrm{CR_A} \approx 4$. These results indicate that it is not straightforward to a priori select the SVD threshold for a desired error level. The farfield pattern of the 10×1 monopole array under the endfire excitation is shown in Fig. 8 for the full MoM, method A ($\tau = \tau_{\mathrm{max,A}}$) and method B ($\tau = \tau_{\mathrm{max,B}}$) , and good agreement is observed.

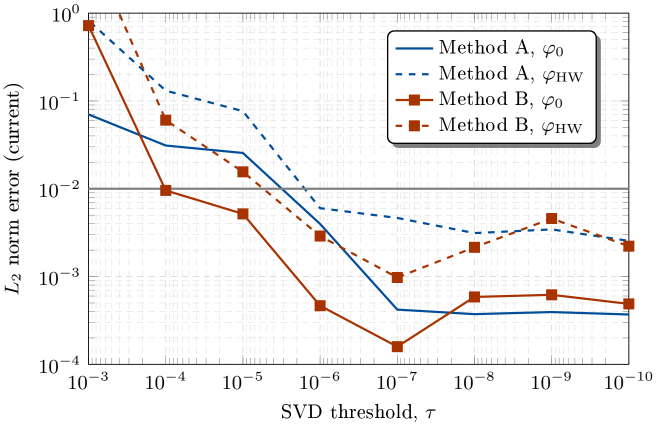

Figure 6: Relative error of the retrieved current vector for the monopole array. The phaseshifts are $\varphi_0 = 0$ and $\varphi_{\mathrm{HW}} = -(kd + 2.94/N)$.

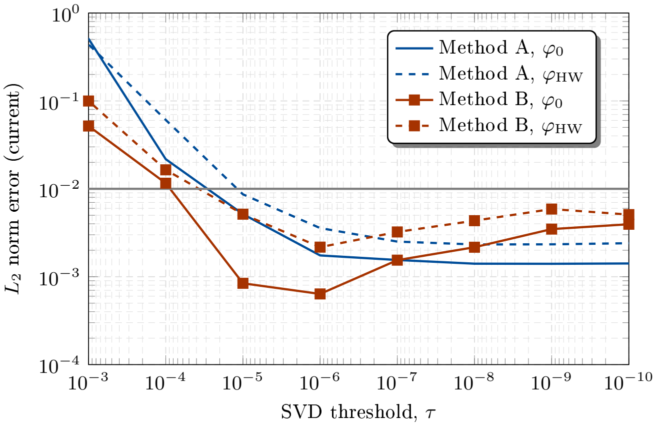

Figure 7: Relative error of the retrieved current vector for the bowtie array. The phaseshifts are $\varphi_0 = 0$ and $\varphi_{\mathrm{HW}} = -(kd + 2.94/N)$.

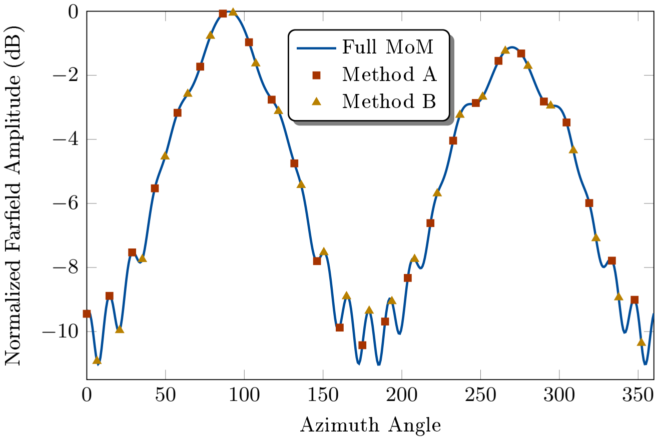

Figure 8: Normalized farfield pattern for the 10×1 monopole array with $\varphi = -(kd + 2.94/N)$. The SVD threshold for the methods are $\tau_{\max,\mathrm{A}} \simeq 10^{-6}$ and $\tau_{\max,\mathrm{B}} \simeq 10^{-5}$ respectively.

4 Conclusions

Two different MBF methods, capable of treating subdomains in contact, have been investigated and benchmarked against each other, and their performance assessed with respect to broadside and endfire excitation. The study has shown that both methods can provide accurate solutions and a significant compression of the total equation system. However, method B presented in [7] has some advantages compared to method A presented in [9], particularly since the reduction of unknowns is considerably greater for a certain level of accuracy. As the size of the problem grows larger, the gain of achieving as great compression as possible would become more critical. Notably, the overall compression (i.e., the singular value sequence) is dependent on how the response matrix is generated, and due to the many different variations of the MBF method that have been proposed in previous literature, this study has provided a consistent approach with the treatment of interconnections as the only difference between the methods.

The complexity of implementation is not regarded here, as we argue that individual preferences and source code will greatly affect that choice.

References

[1] D. J. Bekers, S. J. van Eijndhoven, A. A. van de Ven, P.-P. Borsboom, and A. G. Tijhuis. Eigencurrent analysis of resonant behavior in finite antenna arrays. *IEEE Trans. Microwave Theory Tech.*, **54**(6), 2821–2829, 2006.

[2] C. Craeye, J. Laviada, R. Maaskant, and R. Mittra. Macro basis function

framework for solving maxwells equations in surface integral equation form. *The FERMAT Journal*, **3**, 1–16, 2014.

[3] W. C. Gibson. *The Method of Moments in Electromagnetics.* CRC press, 2014.

[4] W. W. Hansen and J. R. Woodyard. A new principle in directional antenna design. *Proc. IRE*, **26**(3), 333–345, 1938.

[5] E. Lucente, A. Monorchio, and R. Mittra. An iteration-free MoM approach based on excitation independent characteristic basis functions for solving large multiscale electromagnetic scattering problems. *IEEE Trans. Antennas Propag.*, **56**(4), 999–1007, 2008.

[6] R. Maaskant, R. Mittra, and A. Tijhuis. Application of trapezoidal-shaped characteristic basis functions to arrays of electrically interconnected antenna elements. In *Electromagnetics in Advanced Applications, 2007. ICEAA 2007. International Conference on*, pages 567–571. IEEE, 2007.

[7] R. Maaskant, R. Mittra, and A. Tijhuis. Fast analysis of large antenna arrays using the characteristic basis function method and the adaptive cross approximation algorithm. *IEEE Trans. Antennas Propag.*, **56**(11), 3440–3451, 2008.

[8] S. N. Makarov. *Antenna and EM Modeling with MATLAB.* John Wiley & Sons, New York, NY, 2002.

[9] L. Matekovits, V. A. Laza, and G. Vecchi. Analysis of large complex structures with the synthetic-functions approach. *IEEE Trans. Antennas Propag.*, **55**(9), 2509–2521, 2007.

[10] V. V. S. Prakash and R. Mittra. Characteristic basis function method: A new technique for efficient solution of method of moments matrix equations. *Microwave and Optical Technology Letters*, **36**(2), 95–100, 2003.

[11] S. M. Rao, D. R. Wilton, and A. W. Glisson. Electromagnetic scattering by surfaces of arbitrary shape. *IEEE Trans. Antennas Propag.*, **30**(3), 409–418, 1982.